

The reformation of catalyst: From a trial-and-error synthesis to rational design

Ligang Wang[§], Jiabin Wu[§], Shunwu Wang, Huan Liu, Yao Wang, and Dingsheng Wang (✉)

Department of Chemistry, Tsinghua University, Beijing 100084, China

[§] Ligang Wang and Jiabin Wu contributed equally to this work.

© Tsinghua University Press 2023

Received: 24 June 2023 / Revised: 18 July 2023 / Accepted: 23 July 2023

ABSTRACT

The appropriate catalysts can accelerate the reaction rate and effectively boost the efficient conversion of various molecules, which is of great importance in the study of chemistry, chemical industry, energy, materials and environmental science. Therefore, efficient, environmentally friendly, and easy to operate synthesis methods have been used to prepare various types of catalysts. Although previous studies have reported the synthesis and characterization of the aforementioned catalysts, more still remain in trial and error methods, without in-depth consideration and improvement of traditional synthesis methods. Here, we comprehensively summarize and compare the preparation methods of the trial-and-error synthesis strategy, structure–activity relationships and density functional theory (DFT) guided catalysts rational design for nanomaterials and atomically dispersed catalysts. We also discuss in detail the utilization of the nanomaterials and single atom catalysts for converting small molecules (H_2O , O_2 , CO_2 , N_2 , etc.) into value-added products driven by electrocatalysis, photocatalysis, and thermocatalysis. Finally, the challenges and outlooks of mass preparation and production of efficient and green catalysts through conventional trial and error synthesis and DFT theory are featured in accordance with its current development.

KEYWORDS

trial-and-error synthesis, structure–activity relationships, density functional theory (DFT) guidance, nanomaterials, atomically dispersed catalysts

1 Introduction

Human production and life are inseparable from chemical reactions, which are related to various fields such as health, environment, and energy. The control of chemical reactions is the core and key of chemical science. How to make chemical reactions more precise and controllable? This requires the help of catalytic technology. Catalytic reactions, through the interaction between catalysts and reactants, change the reaction energy barrier of chemical reactions to achieve the goal of regulating chemical reactions. The essence of this interaction is the electronic interaction between reactant molecules and catalyst particles. Scientists have found that when particles reach the nanoscale, the originally continuous electronic energy bands will be dispersed into independent electronic energy levels. By precisely regulating the electronic states, reactant molecules and catalysts can be “matched”, achieving more precise catalytic reactions. In the chemical industry, over 85% of processes rely on catalysts to accelerate reaction rates. Therefore, achieving more precise and efficient catalyst synthesis is an important challenge for basic and applied research in catalysis, and it is also the direction and driving force that researchers have been striving for.

The application history of catalysts in industry can be traced back to the late 19th century, from the industrial production of sulfuric acid to the chlor-alkali industry, from industrial nitrogen fixation to ammonia synthesis via Haber–Bosch process, later to the petroleum refining industry, and later to the catalytic polymer

synthesis industry [1–4]. Catalysts play an important role, and every update of catalysts will trigger a huge transformation in the chemical industry. At the same time, the significant progress brought by them is also evident to all. The synthetic ammonia industry has improved the fertility of the land and alleviated our food problems; the production of low-level hydrocarbons through petroleum refining has alleviated our energy problems; the synthesis of polymers enriches our daily necessities.

In 1959, Richard Phillips Feynman, a famous American physicist, once said, “there is plenty of room at the bottom”, and proposed the idea of gradually shrinking the device, so that at last, humans could directly arrange atoms and molecules as needed to manufacture products, pointing out a new idea for the development of nanotechnology in the future [5, 6]. He won the Nobel Prize in Physics in 1965. Since the 1990s, a technological revolution represented by information technology, biotechnology, energy technology, and nanotechnology has been emerging globally. Among them, nanoscience and technology, which gradually formed worldwide in the 1980s and 1990s, are the most representative hot areas of widespread concern. Nanoscience and technology is a multi-disciplinary technology based on modern advanced science and technology. Its in-depth development has led to a series of new science and technology, such as nano physics, nanochemistry, nano biology, nano electronics, nano materials science, nano technology, nano process, etc. Nanochemistry is one of the most important ones, which can be

Address correspondence to wangdingsheng@mail.tsinghua.edu.cn

said to be the basis of nano science and technology, which has greatly promoted the emergence of nano catalysts. The size of nano particles is generally between 1–100 nm, larger than atomic clusters and smaller than micro powders. It is neither a typical micro system nor a typical macro system. The mesoscopic system in the transitional region between micro and macro is a new level of matter. As a new phase in the transformation of matter from atoms and molecules to bulk matter, it has many characteristics that are different from both microscopic particles and macroscopic objects. After nearly a decade of development, the preparation methods of nanocatalysts have become relatively mature, and multifunctional and efficient catalysts can be prepared and produced on a large scale [7–14].

Adding nanocatalysts to chemical reactions can greatly improve catalytic efficiency and selectivity, as well as control reaction speed, and even reactions that were previously impossible can be carried out. At present, nanosized powder such as platinum black, silver, aluminum oxide, iron oxide, zinc oxide, etc. have been directly used as catalysts for oxidation, reduction and synthesis of polymer, with obvious catalytic effect. For example, nanometer zinc oxide particles are used as photocatalyst, the decomposition of organic matter can be greatly accelerated, and the reaction speed is 100–1000 times that of ordinary zinc oxide. In addition, the nickel or copper-zinc compounds nanoparticles are used to replace expensive platinum and palladium catalysts for the oxidation of organic compounds. The research findings demonstrated that platinum black nanocatalysts can reduce the reaction temperature of ethylene from 600 °C to room temperature. Likewise, the aluminum nanoparticles are added to solid rocket fuel, the combustion efficiency can be improved by many times. Using nano-nickel as a combustion catalyst for solid rocket fuel can increase the combustion efficiency by 100 times. Although nanocatalysts greatly improve catalytic efficiency, the atomic utilization of nanocatalysts still needs to be improved.

In order to improve further the atomic utilization efficiency of catalysts, researchers have been working hard. Impressively, the concept of “single atom catalysis” was jointly proposed for the first time by academician Zhang Tao and collaborators in 2011 [15]. As a special type of supported metal catalyst, single atom catalysts (SACs) specifically refers to the presence of all metal components on the support in the form of single atom dispersion. In just 10 years, single atom catalysis has rapidly become the forefront of research in the field of catalysis [5, 16–20]. More and more research results show that monatomic catalysts exhibit significantly different activity, selectivity and stability from conventional nanocatalysts due to their special structure. With the development of advanced characterization technology, monatomic catalysts provide an opportunity to clarify the structure–activity relationship of catalysts at the atomic and molecular levels, and also provide a possibility to connect heterogeneous catalysis with homogeneous catalysis. Recently, a large amount of research work has been systematically summarized on the synthesis of single atom site catalysts using chemical methods in recent years [5, 21–28], focusing on discussing how to achieve atomic level dispersion of metal precursors in synthesis strategies, how to prevent migration and aggregation during the preparation process, and how to ultimately achieve single atom stability on the supports. At the same time, the advantages and disadvantages of various synthesis strategies were also compared. Finally, the author pointed out the difficulties and challenges that chemical synthesis of SACs still faces, and pointed out that SACs needs more in-depth exploration and research investment in industrial development, including exploring the possibility of replacing traditional homogeneous catalysts with heterogeneous SACs, exploring high load and high stability SACs

to meet industrial needs, solving problems such as catalyst carbon deposition and metal active center poisoning, further screening out systems that can be suitable for large-scale production of single atom catalysts.

With the global energy shortage and increasingly severe environmental issues, the development of clean energy is urgent. With chemical energy conversion, small molecules (H_2O , CO_2 , N_2 , etc.) in the air can be converted into value-added products (H_2 , $\text{C}_x\text{H}_y\text{O}_z$, NH_3 , etc.) driven by electrocatalysis [17, 29–33], photocatalysis [34–39], and thermocatalysis [17, 23, 26, 40–45], so as to achieve green and sustainable production of energy and important chemical raw materials. Therefore, this is seen as one of the potential solutions to current energy shortages and environmental issues, and is also the fundamental goal of breaking through the dual carbon target. In the past few decades, significant progress has been made in the research and development of catalysts, but they are still limited to the traditional mass trial and error stage. Fortunately, the rapid development of computing technology has brought dawn to the efficient preparation of catalysts through the combination of density functional theory (DFT) and machine learning [46–50]. Firstly, in terms of understanding experiments, using DFT calculations can help determine the atomic structure of active centers, describe reaction mechanisms, and construct activity descriptors to understand the origin of activity. Furthermore, a good “structure–activity” relationship is established to guide the rational design of catalysts, as well as the design principles for efficient catalysts that break through the inherent linear relationship limitations. Secondly, utilizing high-throughput and machine learning techniques can screen efficient catalysts from a large number of candidate materials and further guide experimental synthesis. The most important problem lies in the development and establishment of methods and models to achieve a catalytic reaction model in a real chemical environment, so as to quantitatively describe and evaluate the activity, selectivity, stability, etc. of the catalyst, and then design a more efficient and real catalyst.

Considering the aforementioned discussions, this review aims to systematically summarize the trial and error synthesis and rational design of catalysts, as shown in Fig. 1. In this review, we summarized the preparation strategies for nanomaterials with different dimensions and single atom catalysts in view of trial-and-error method. Furthermore, guided by structure–activity relationship and DFT, the advanced nano and atomic level dispersed catalysts have been successfully prepared. In addition, we elaborate the catalytic applications for various types of catalysts in different fields, such as hydrogen evolution reaction (HER), oxygen evolution reaction (OER), oxygen reduction reaction (ORR), nitrogen reduction reaction (NRR), CO_2 reduction reaction (CO_2RR), carbon dioxide thermal catalytic hydrogenation to hydrocarbon fuel and propane dehydrogenation (PDH). Finally, we also propose future directions yet to be explored for the accurate characterization of catalyst structure, reasonable identification of active site and improvement of synthesis efficiency utilizing advanced characterization techniques and theories.

2 Trial and error method for synthesizing catalysts

2.1 Synthesis method of nanomaterials

Up to now, there are many methods to prepare nanomaterials (NMs), such as mechanical grinding, physical grinding, chemical vapor deposition (CVD), sol gel method and vacuum condensation. The preparation methods for nanomaterials are also different according to their principles: in view of the different



清华大学出版社



Springer | www.editorialmanager.com/nare/default.asp

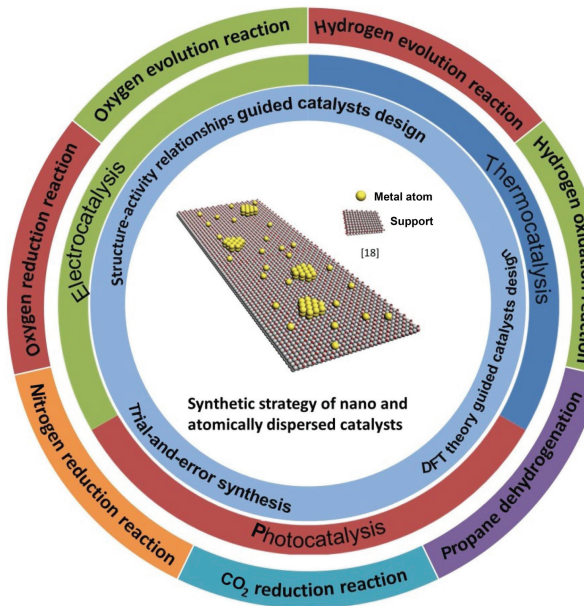


Figure 1 Overview of the topics covered in this review. Reproduced with permission from Ref. [18], © American Chemical Society 2022.

states in the reaction process, the method can be mainly divided into dry method and wet method; according to the different states in which the raw materials exist, the method can also be divided into solid-phase method, gas-phase method, and liquid-phase method; based on preparation method, the method can also be divided into chemical methods (precipitation method, phase transformation method, aerosol reaction method, and CVD, etc.), physical methods (vapor condensing method, electric spark method, ion sputtering method, etc.). Notably, nanomaterials are prepared by a variety of synthesis strategies, including “bottom-up” and “top-down” approaches [7, 51, 52]. Among, the bottom-up method usually involves the chemical reaction process. This method controls the growth process of materials from the perspective of atoms or molecules, and has become a commonly used method for the synthesis of metal nanomaterials. Since the regulation of physical parameters such as size, morphology, structure and composition of materials is more accurate and efficient. The synthesized method of bottom-up usually includes: CVD, hydrothermal, co-precipitation, and sol-gel [8, 53–55]. Top-down method typically involves pulverizing solid metal particles physically or chemically, and reducing their size to the nanoscale, especially for two-dimensional nanomaterials. “Top-down” fabrication can be further divided into two major categories: mechanical cleavage and liquid exfoliation [56–59]. Compared with the bottom-up process, top-down method is simple to operate, low cost, and few by-products generated. However, the operation process is easy to introduce impurities and oxidize metals, leading to the poor uniformity. The synthesized method of top-down usually includes: ball milling, thermal evaporation, laser ablation, and sputtering [53, 54, 60, 61].

2.1.1 Zero-dimensional (0D) NMs

The 0D-NMs mainly refer to nanoparticles with dimensions ranging from 1 to 100 nm for each dimension (x, y, z) and usually include quantum dots (QDs) and nanoclusters. Among them, QDs, also known as semiconductor fluorescent nanocrystals, are mainly nanoparticles composed of II-VI group elements (such as CdS, CdSe, CdTe, ZnSe, etc.) and III-V group elements (such as InP, InAs, etc.), with a particle size generally less than 20 nm [62, 63]. Due to its multiple effects such as size confinement, quantum confinement, macroscopic quantum tunneling, and surface effect, it exhibits many optical and physical properties that are different

from macroscopic substances. Therefore, it has extremely broad application prospects in fields such as optics, electronics, magnetic media, catalysis, medicine, life sciences, and functional materials.

Trap states in colloidal QD solids limit the open circuit voltage and short circuit current, which significantly affects the performance of QD solar cells. Zhang group minimized the (100) facets of ~ 3 nm PbS QDs to suppress trap states, by controlling the balance between kinetic and thermodynamics-dominated growth conditions (Fig. 2(a)) [64]. PbS QD synthesized by a hot-injection method at relatively low temperatures and high supersaturation follows kinetic-dominated growth, producing near-octahedral nanoparticles terminated primarily by (111) crystal planes. Compared to PbS QD from thermodynamically dominated growth, the PbS QDs synthesized by this method with less (100) facets show fewer trap states in the QD solids, resulting in better photovoltaic device performance with a power conversion efficiency of 11.5%. The same group developed the synthesis of the low-bandgap PbS QDs (0.65–1 eV) by cation exchange from ZnS nanorods (NRs), which has the advantages of high monodispersity, ease-of-size control, *in situ* passivation of chloride, high stability, “clean” surface, and easy scalability [65]. When ZnS NRs dissolved during cation exchange process, the sulfur precursors released to promote size focusing of small band gapped PbS QDs. Compared with the devices with similar bandgaps, infrared solar cells based on the above PbS QDs with different bandgaps show better performance. Based on ~ 0.95 eV PbS QD, under air mass (AM) 1.5 solar illumination, 4.2% under perovskite filtration illumination, and 1.1% under silicon filtration illumination, the high efficiency is 10% (Figs. 2(b)–2(d)).

Sargent et al. introduced a mixed lead-halide (MPbX) ligand-exchange strategy to achieve the thorough surface passivation without compromising transport [66]. The MPbX-PbS prepared by this method improved both passivation and transport by exchanging each lead halide onto their favored infrared (IR)-PbS facet. The performance of MPbX-PbS carbon quantum dots (CQDs) showed improved passivation, higher charge transport than single lead halide. The devices have high IR open-circuit voltages and maintain high short-circuit current densities, which could benefit to the development of IR photodetectors or IR light-emitting diodes. Ning used NiO as the p-type layer and PbS QDs with iodide ligands as the n-type active layer to construct an effective inverted-structure QD solar cell (Fig. 2(e)) [67]. Since the high photocurrent caused by big depletion region in the QD layer, a layer of slightly doped p-type QDs with 1,2-ethanedithiol as ligands was inserted to prevent interfacial recombination and increase the voltage of the device. A statistical study of the efficiency of 30 devices showed that the average efficiency of the grading device structure was 8.40% higher than that of the non-grading device 6.81% (Figs. 2(f) and 2(g)). The highest efficiency was as high as 9.7%, which was double the best performance of similar equipment of 4.2%. The Ning’s work effectively solved the bottleneck problem of PbS colloidal QD solar cells based on the inverted structure. Different from the traditional “bottom-up” approach in colloidal chemical, Du used a facile “top-down” strategy to controllably prepare crystalline monodisperse colloidal PbS quantum dots with size and narrow dispersion of 5.5%–9.1% by laser irradiation of larger-sized polydisperse PbS nanocrystal suspensions [68].

Moreover, 1-dodecanethiol as surfactant and sulfur source, with a small degree of polydispersity and surface coverage, enabled colloidal quantum dots to exhibit size-tunable near-infrared photoluminescence properties and self-assemble into ordered two-dimensional or three-dimensional super-lattices. The quantum-confinement effect of quantum dots and the size-selective-vaporization effect of monochromatic, low-intensity millisecond

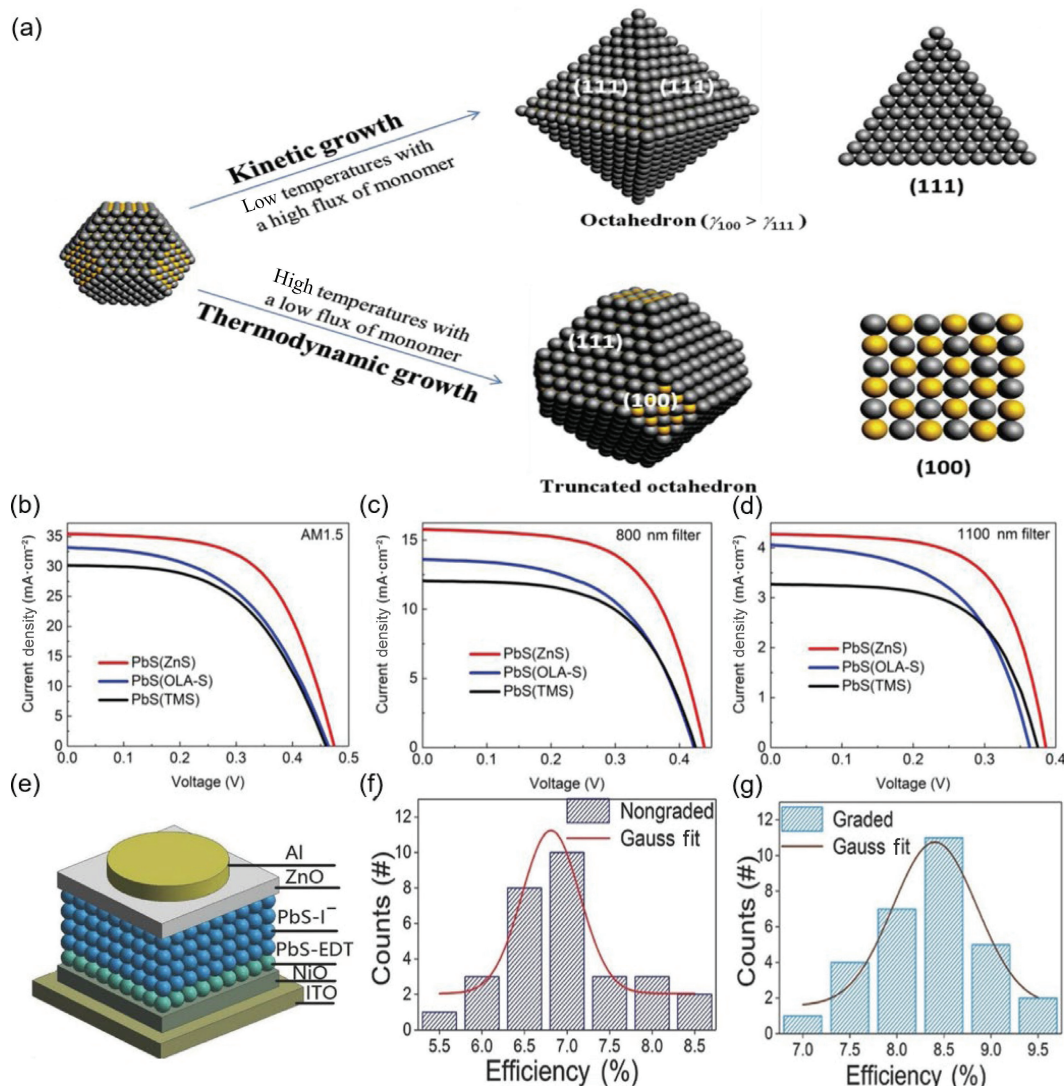


Figure 2 (a) Controlling the terminating facets of PbS QDs via a balance of the growth regimes between kinetic (top) and thermodynamic (bottom) growth conditions. The black and yellow spheres represent Pb and S atoms, respectively. Reproduced with permission from Ref. [64], © Wiley-VCH GmbH 2020. (b)–(d) J – V curves of the device under AM 1.5, 800 nm filtered and 1100 nm filtered illumination, respectively. For comparison, the J – V curves of devices based on PbS(TMS) and PbS(OLA-S) are also plotted. Reproduced with permission from Ref. [65], © Wiley-VCH GmbH 2020. (e) Graded inverted QD solar cell. (f) and (g) Histogram of PEC with statistics based on 30 devices for the same batch. Average efficiencies are 7% and 8.5% for nongraded structure and graded structure, respectively. Reproduced with permission from Ref. [67], © Wiley-VCH GmbH 2018.

pulsed laser light enable the successful preparation of the monodisperse alternating PbS quantum dots. Based on perovskite solar cell (PSC) and PbS QDs device, Tavakoli reported the efficient and stable monolithic tandem solar cells (perovskite/PbS QDs) with 2T and 4T configurations [69]. When SnO₂-passivated ZnO nanowires (NWs) were used as the electron transport layer of the PSC front cell, the power conversion efficiency (PCE) of 2T and 4T tandem devices could achieve 17.1% and 21.1% respectively. Within 500 h of continuous illumination, the 2T tandem cell showed excellent working stability, and the PCE loss was only 6%. Meanwhile, PbS QDs possessed the superior air stability, and the devices demonstrated impressive environmental stability in an environment of 65% relative humidity for 70 days. Wu altered the transport properties of MAPbBr₃ perovskite single crystals devices by intercalating PbS QDs [72]. The incorporated QDs significantly enhanced the charge transport and reduce current-voltage hysteresis. Moreover, the pristine single-crystal device exhibits negative differential resistance, while the quantum dot-embedded crystal exhibits filament-type switching behavior with greatly improved device stability. This study highlights the potential of quantum dot-embedded hybrid perovskites as a new medium for advanced electronic devices. The original single

crystal device with poor stability exhibited negative differential resistance. With the embedding of QDs, the crystal exhibited filament-type switching behavior, and the stability is greatly improved. This work embedded QDs into hybrid perovskites, providing a strategy for improving the stability of hybrid organic-inorganic halide perovskites applied for advanced electronic devices.

In addition, the fluorescence properties of quantum dots have also been widely studied and applied. Xu et al. found fluorescent spherical nanoparticles in the experimental process of preparing single-walled carbon nanotubes, but the fluorescence performance was very poor [73]. In 2006, Sun et al. improved the fluorescence emission properties of this new type of nanoparticles by surface passivation, and named them "CQDs" for the first time [74]. Since then, carbon quantum dots have attracted much attention as a new member of the carbon family. CQDs have certain advantages over well-known and commercialized metal quantum dots, such as ease of synthesis and negligible cytotoxicity, they have become the most promising emerging fluorescent labeling materials for cell imaging and bio-imaging, and have also found potential applications in photocatalysis, energy conversion/storage, optoelectronics, drug delivery, and fluorescent probes [75]. Costa-

Fernandez investigated a one-pot microwave-assisted hydrothermal method for the preparation of CQDs doped with nitrogen and lanthanides [76]. The doped CQDs exhibited intense fluorescence and high magnetic resonance (MR) and computed tomography (CT) contrast when used as imaging contrast agents. No significant cytotoxicity was shown after 24 and 72 h exposure to the three different cell lines. Moreover, significant enhancement of MR and CT of bladder and kidney can be observed in mice after intravenous injection. This suggested that the synthesized nanoparticles have great potential as contrast agents for multimodal imaging *in vivo*.

The CQD-implanted g-C₃N₄ nanotubes (CCTs) were prepared by a thermal polymerization approach (Fig. 3(a)) [70]. The injection of CQD promotes photoelectron transport and inhibits charge recombination through coupled heterogeneous interface. The electronic structure and morphology of CCTs were optimized to improve visible light absorption and weaken photo-generated carriers transfer barriers. The photocatalytic stability test showed that the CCTs had high photocorrosion stability. Under the illumination at 420 nm, CCTs exhibited efficient photocatalytic performance, the H₂ production rate was 3538.3 μmol·g⁻¹·h⁻¹, and the quantum yield was 10.94% (Figs. 3(b) and 3(c)). The implanted CQDs can effectively improve the photo-generated carriers transfer rate and absorbability of g-C₃N₄, thus improving their activity in photocatalytic hydrogen production. In order to separate clean hydrogen energy from water using solar energy, a facile “spot heating” synthesis of CQDs/C₃N₄ was designed by Liu group [77]. The effects of introduced CQDs were verified by DFT calculations and electrochemical experiments. CQDs could expand the optical absorption spectrum of C₃N₄ and were benefit to the transport of photocarriers from the excited site. Moreover, CQDs with superior peroxidase mimetic showed higher activity (H₂ production rate, 152 μmol·g⁻¹·h⁻¹) than C₃N₄. This study provides feasibility for efficient solar hydrogen production synchronously with contaminant decomposition. Yin et al.

presented a template-assisted, spin-coating method to prepare CQD-sensitized inorganic CsPbBr₃ inverse opal (IO) perovskite films [78]. Compared to planar CsPbBr₃, CsPbBr₃ IO greatly improves the utilization of light in the perovskite solar cells, due to the slow photon effect. The injection of CQD in IO frameworks effectively promoted the electron-hole extraction and injection process, and extended the carrier lifetime. Together, they contributed to double the power conversion efficiency (8.29%) and an incident photon-to-electron conversion efficiency of 76.9%. The strategy of constructing CQD-sensitized CsPbBr₃ IO perovskite to enhance PCE can be extended to the design of novel optoelectronic devices, enabling all-inorganic cesium lead halide perovskites to be applied in perovskite solar cells. Using the sequential dehydrative condensation and dehydrogenative planarization (DCDP) approach, Fan group prepared red emissive carbon quantum dots (R-CQDs), and the quantum yield was 53% [79]. The ultraviolet-pumped CQD phosphors-based warm white light-emitting diode (WLED) was fabricated based CQDs, achieved good color stability, high device stability, and a color rendering index of 97. Dai et al. developed metal-free CQD/holey graphene composite catalysts for Li-CO₂ batteries [71]. The prepared Li-CO₂ batteries exhibited excellent performance because of the synergistic effect of the CQD/holey graphene (hG) composite structure. Defect-rich CQDs provided high catalytic activity, and the conductive porous graphene sheets transport electron/electrolyte fast. When the current density was 0.5 A·g⁻¹, the reversible capacity of the Li-CO₂ batteries can reach 12,300 mAh·g⁻¹ (Fig. 3(d)). The overpotential was as low as 1.02 V (vs. Li/Li⁺) at current density of 0.1 A·g⁻¹. Moreover, the cycle stability was 235 times at the current density of 1 A·g⁻¹, which is better than all lithium batteries (Figs. 3(e)–3(g)). A novel carbon-quantum-dots-loaded ruthenium nanoparticles (Ru@CQDs) was developed by Yang group, and was used for the HER [80]. The results showed that Ru@CQDs exhibited excellent catalytic performance and good stability under extremely alkaline (1 M KOH)

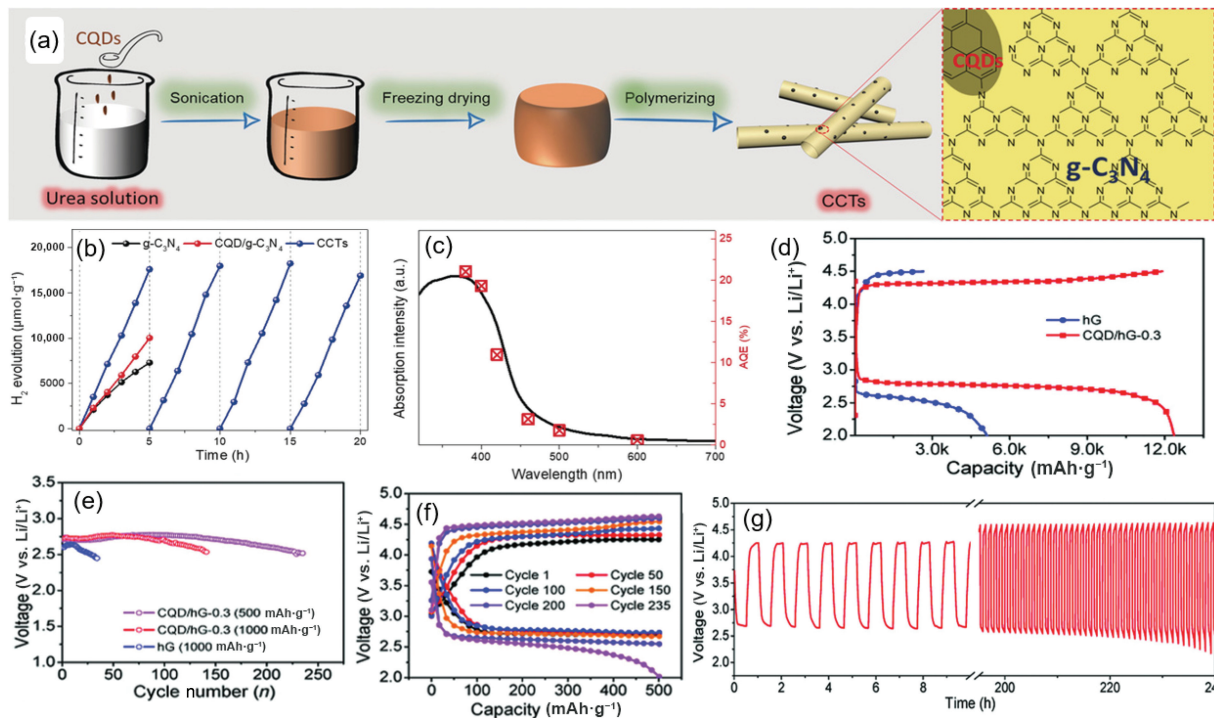


Figure 3 (a) Preparation procedure of CCTs. (b) Time course of H₂ evolution experiments for g-C₃N₄ and CCTs under visible light irradiation ($\lambda > 420$ nm), and (c) wavelength dependent AQE of H₂ evolution over CCTs (right axis), and UV-Vis absorption spectra of CCTs (left axis). Reproduced with permission from Ref. [70], © Wiley-VCH GmbH 2018. (d) Full discharge-charge curves of Li-CO₂ battery performance. (e) Long-term stability. (f) Selected discharge-charge curves. (g) Time–voltage curves for the Li-CO₂ battery based on the CQD/hG-0.3 catalyst with 500 mA·h·g⁻¹ capacity limitation at the current density of 1 A·g⁻¹. Reproduced with permission from Ref. [71], © Wiley-VCH GmbH 2018.

conditions. Most importantly, a current density of $10 \text{ mA}\cdot\text{cm}^{-2}$ can be achieved at an overpotential of 10 mV, indicating superior HER activity.

2.1.2 One-dimensional (1D) NMs

1D NMs usually refer to nanomaterials that are in the nanoscale of 1–100 nm for two dimensional directions and have a length at the macroscopic scale. The types of one-dimensional nanomaterials typically include nanotubes (NTs), nanorods, nanowires, and nanoribbons or nanobelts [81–89]. To obtain the desired properties, the size, morphology, composition and structure of the material should be controlled carefully. However, due to the small size of 1D NMs, there are some problems in the preparation process, such as poor catalytic performance and homogeneity of materials prepared in large quantities, and poor repeatability of preparation methods. Based on the above problems, researchers have developed different preparation methods for different compound materials.

Iijima et al. successfully prepared carbon nanotubes in 1991, and the preparation process was done by arc evaporation [90]. Nanotube is a seamless steel tube-like structure that is also wound according to certain rules. One of the typical representatives of nanotubes is carbon nanotubes. Carbon nanotubes are one-dimensional nanostructures whose structure is to seamlessly curl the graphite layer at a certain helical angle. Carbon nanotubes have good electrical properties due to their special structure. Carbon nanotubes can often be prepared by chemical vapor

deposition and arc discharge methods, and the growth conditions are adjusted during the preparation process to obtain carbon nanotubes with different wall layers. The properties of carbon nanotubes allow them to be used in field emission sources, scanning probes, and nanodevices [91, 92]. For example, Jones group varied covalent attachment of green fluorescent protein (GFP) on the sidewalls of single carbon nanotubes via a simple photochemical attachment process to prepare single-walled carbon nanotube (SWCNT) bio-optoelectronic transistors [93]. The protein residue coupling site determined the electrical behavior of semiconducting SWCNTs. When a chromophore was attached proximal to the residue of GFP, the phototransistors with specific wavelengths had a high responsivity of $7 \times 10^3 \text{ A}\cdot\text{W}^{-1}$ at 470 nm and turned off in less than 38 s. Attaching a second residue to the distal end of the chromophore, the optoelectronic memory showed rapid and reproducible conductivity switching with up to 15-fold modulation, recoverable on application of gate voltage. This work combined the photoactive GFP with the nanomaterial (carbon nanotubes), providing a particular route for the fabrication of photonic devices. Using CO as the carbon source, Kauppinen directly synthesized SWCNTs films with tunable chirality distribution and tunable color by modulating the amount of CO_2 in floating catalyst chemical vapor deposition (FC-CVD) [94]. The diameter and chirality distribution of SWCNTs changed when modulating the volume percent of carbon dioxide, resulting in the color of the films tuning from gray, green, brown to gray (Figs. 4(a) and 4(b)). Moreover, the narrow chirality

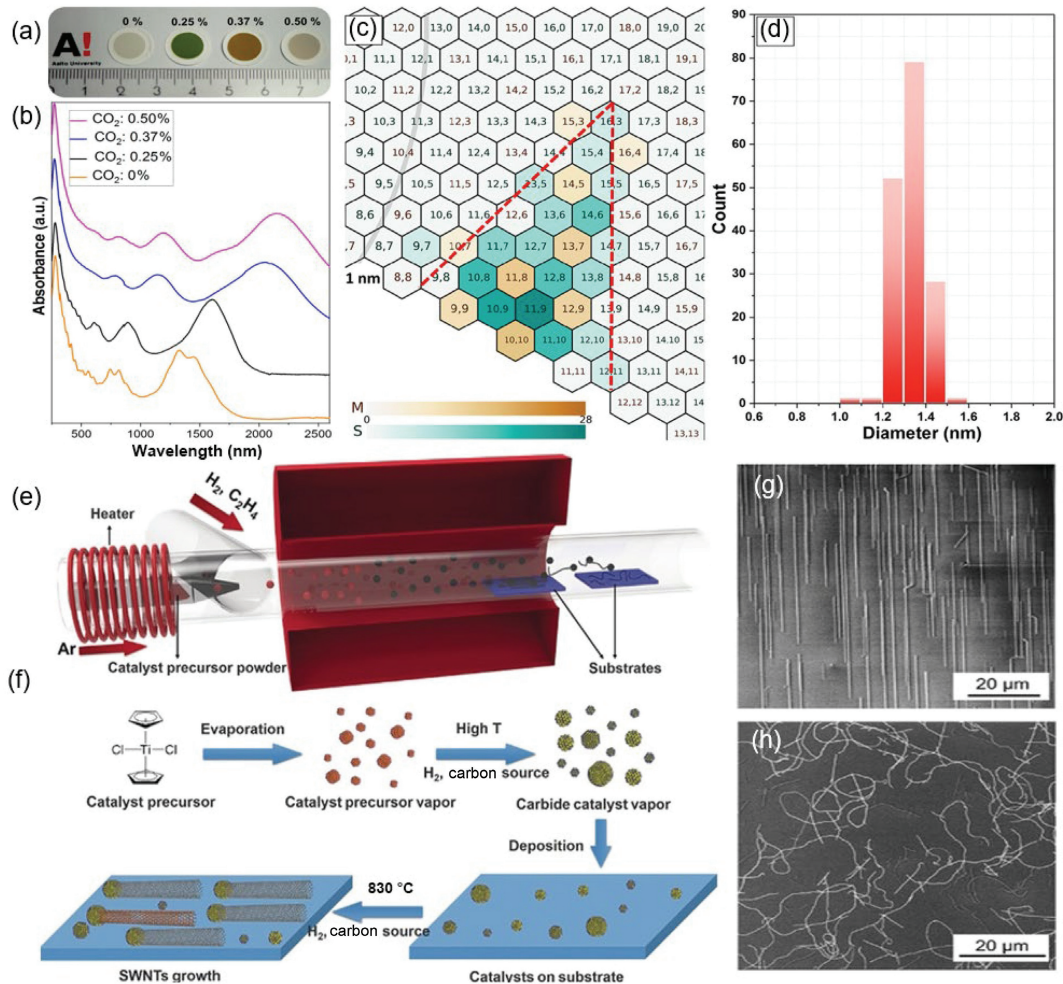


Figure 4 (a) Optical image of SWCNT thin films on filters obtained from different CO_2 concentration at $850 \text{ }^\circ\text{C}$ and (b) corresponding absorption spectra. (c) Chirality and (d) diameter distribution of SWCNTs with 0.25 vol.% CO_2 at $880 \text{ }^\circ\text{C}$. Reproduced with permission from Ref. [94], © American Chemical Society 2018. (e) Schematic illustration of the designed FSCCVD system. (f) Schematic showing the formation process of carbide catalyst and the growth of SWNTs on substrates. SEM images of SWNTs grown on (g) quartz and (h) Si/SiO₂ substrates at $830 \text{ }^\circ\text{C}$. Reproduced with permission from Ref. [96], © Wiley-VCH GmbH 2020.

distribution clustered around (11,9) with extremely narrow diameter range (> 98% between 1.2 and 1.5 nm) could be achieved under suitable temperature (Figs. 4(c) and 4(d)). Kong et al. developed a non-destructive soft-lock mapping method to highly align nano-sized carbon nanotube bundles in CNT (angular standard deviation $\sim 0.03^\circ$) [95]. The assembled CNT bundles exhibited high packing density ($\sim 400 \mu\text{m}^{-1}$) and high current-carrying capacity ($\sim 1.8 \times 10^8 \text{ A}\cdot\text{cm}^{-2}$), high current density ($\sim 38 \mu\text{A}\cdot\mu\text{m}^{-1}$) and low contact resistance ($\sim 1.6 \text{ k}\Omega\cdot\mu\text{m}$) for nano-electrical contacts in high-density monolayer molybdenum dioxide transistors. The development of super-aligned CNT bundles through non-destructive soft-lock mapping method, improved device-to-device uniformity and highly reduced device area. This work provided a new direction for future electronic devices and advanced integration technologies. Zhang et al. presented the floating carbide solid catalyst chemical vapor deposition (FSCCVD) method to prepare FSC for the controlled growth of SWNTs (Figs. 4(e)–4(h)) [96]. Titanium carbide catalyst was prepared with titanocene dichloride precursor system. Since (16,8) tubes belong to $(2m,m)$ tube family, the residence time in the floating system is short, four-fold symmetric carbon nanotubes can be rapidly grown on the titanium dioxide (200) plane, and the purity can reach 74%. Horizontal nanotube arrays are particularly attractive in technical applications because of their superior current output capability. The direct growth of horizontal SWNT arrays with controllable chirality was reported by Zhang group [97]. By controlling the symmetry of the active catalyst surface, horizontal SWNT arrays with the desired chirality can be grown from solid carbide catalyst surfaces. Based on principle, the researchers grew (12,6) and (8,4) nanotube arrays with chiral purity of greater than 90% and 80%, with surface densities of more than 20 and 10 tubes per micron, respectively. By optimizing the catalyst size and reduction temperature, the purity of high symmetry $(2m,m)$ nanotubes can be increased, which has high probability for future electronic device applications. Liu et al. prepared a flexible thermoelectric material by anchoring highly ordered Bi_2Te_3 nanocrystals on a SWCNT network [98]. The method was suitable for a series of thermoelectric materials with layered structures such as Bi_2Te_3 , Bi_2Se_3 and Sb_2Te_3 , and both n- and p-type thermoelectric materials. The experimental and computational results showed that the Bi_2Te_3 SWCNTs material had excellent flexibility and thermoelectric properties, with a power factor of $\sim 1600 \mu\text{W}\cdot\text{m}^{-1}\cdot\text{K}^{-2}$ and a maximum thermoelectric effect value (ZT) of 0.89 at room temperature.

Besides nanotubes, other one-dimensional nanostructures, such as nanowires and nanorods, have also been studied. The structure of nanowires is different from that of nanotubes, the difference lies in the cross section. The nanowire cross-section is cylindrical and solid, while the nanotube cross-section is tubular and hollow. Semiconductor nanotubes have mechanical, electrical and optical properties, and their good properties make them have broad application prospects in materials science, condensed matter physics and chemistry. Basak et al. synthesized the Co-doped (the Co content from 0% to 10%) ZnO nanorods (Co:ZnO NRs) on glass substrates by the hydrothermal method. Their gas-sensing responses to different concentrations of H_2 were investigated at 300 °C, and it was found that 8% Co-doped ZnO nanorods exhibited the highest and faster gas-sensing response [99]. Tian et al. prepared zeolitic imidazolate framework (ZIF)-coated ZnO core-shell nanorods (ZnO@ZIF-8) as molecular sieves by the hydrothermal method [100]. Nitrogen (N_2) adsorption isotherms indicated that ZnO@ZIF-8 nanorods are a typical microporous material. The relationship between the pore size of ZIF-8 and the kinetic diameter of different test gas molecules was investigated. It is found that ZIF-8 with a pore size of 3.4 Å enables formaldehyde

to pass through ZIF-8 quickly and then be detected, which improves the selectivity of ZnO@ZIF-8 core-shell nanorods for formaldehyde. It was indicated that the fabrication of semiconductor@MOF core-shell heterostructures can be a novel approach to improve the selectivity of gas-sensing materials.

Self-assembled nanorods with strong quantum confinement have become an attractive topic for understanding their physical basis and promising technological applications. Yaghmour et al. reported that self-assembled $\alpha\text{-Ag}_2\text{S}$ nanorods were fabricated for the first time by squalene assisted microwave technique [101]. The morphology, crystal structure, size distribution and optical properties of $\alpha\text{-Ag}_2\text{S}$ nanorods were investigated by a series of different characterization methods, such as X-ray diffraction (XRD), transmission electron microscopy (TEM), energy dispersive spectroscopy (EDS), selected area electron diffraction (SAED), X-ray photoelectron spectroscopy (XPS), ultraviolet visible (UV-vis) absorption and luminescence spectrometers. The results showed that the grown silver sulfide had a strong confinement mechanism. Jiang et al. synthesized SnO_2/ZnS nanocomposites by a simple two-step hydrazine-assisted hydrothermal process [102]. The nanocomposite was SnO_2 QD-deposited ZnS nanorods with highly enhanced photocatalytic activity and photostability. The photocatalytic activity of SnO_2/ZnS ($R_{\text{Sn/Zn}} = 0.10$) nanocomposites is 3 times higher than that of pristine ZnS nanorods and 17 times higher than that of commercial ZnS . The addition of SnO_2 quantum dots improves the photocatalytic efficiency of ZnS nanorods. Notably, Sargent et al. successfully synthesized a new class of chiral inorganic nanorod materials by selectively composite magnetic materials in one-dimensional nanostructure units and using their local magnetic field to modulate the interaction between electric dipole moment and magnetic dipole moment [85]. They took one-dimensional $\text{Zn}_x\text{Cd}_{1-x}\text{S}$ ($0 \leq x \leq 1$) semiconductor nanorods with UV visible absorption characteristics as an example, and successfully constructed $\text{Zn}_x\text{Cd}_{1-x}\text{S}\text{-Ag}_2\text{S}$ by integrating $\text{Ag}_2\text{S}/\text{Au}$ core-shell structure components at the vertices of the nanorods to catalyze the fixed-point growth of Fe_3O_4 magnetic nanoparticles/ $\text{Au}@\text{Fe}_3\text{O}_4$ ($x = 1, 0.9, 0.5, 0.3$ and 0) quaternal heterogeneous nanorods. This method has high universality and can be widely used for coupling between various semiconductor materials and magnetic components, opening up a new path for the design and development of chiral optical active nanomaterials in the future.

As one of the representative one-dimensional nanomaterials, nanowires have great potential for various applications in the field of energy storage, as they can maintain electron transport along the long axis and have confinement effects throughout the entire diameter range. Based on the previous work, Mai et al. summarized the nanowires [86]. In this review, they systematically summarized the latest research progress of nanowires for electrochemical energy storage, from reasonable design and construction, *in situ* structure characterization to vital applications for energy storage, such as lithium ion batteries, lithium sulfur batteries, sodium-ion battery and supercapacitors. The problems and limitations in electrochemical energy storage were pointed out, as well as the advantages of using nanowires to solve problems and improve device performance.

2.1.3 Two-dimensional (2D) NMs

Ultra-thin 2D NMs are an emerging category of nanomaterials with sheet like structures, with lateral dimensions exceeding 100 nm or a few micrometers or even larger, but with a thickness of only one or a few atoms (typically less than 5 nm) [103]. Although the exploration of two-dimensional materials can be traced back to decades ago, it only marked the birth of ultra-thin

nanomaterials in 2004. That year Novoselov, Geim and their collaborators successfully stripped graphene from graphite using tape, which is now known as micromechanical stripping [104–106]. Undoubtedly, the discovery of graphene has promoted the rapid development of two-dimensional ultrathin materials. In addition, transition metal dichalcogenides (TMDs, such as MoS₂, WS₂, MoSe₂, WSe₂, TiS₂, NbSe₂, TaSe₂ and etc.), graphene analogs (such as boron nitride (BN)), black phosphorus (BP), layered double hydroxides (LDHs, such as NiFe-LDH, NiCo-LDH, FeCo-LDH, NiAl-LDH, etc.) and transition metal oxides (such as MnO₂, Co₃O₄, WO₃, ZnO and TiO₂) were also prepared and studied. Recently, novel ultrathin 2D crystals, including metal organic frameworks (MOFs), covalent organic frameworks (COFs), graphdiyne, silicene, and MXenes etc., have been extensively studied (Fig. 5), greatly enriching the family of 2D NMs [7, 52, 103, 107, 108]. The above 2D NMs can be used in catalysis, energy-storage devices, sensors, and sustainable environment.

Over the past two decades, we have witnessed tremendous progress in graphene research. It changes the landscape of many fields of science and technology, especially condensed matter physics [104, 109], electronics [110], energy storage and conversion [111], and biomedical research [112]. For example, Geim et al. prepared single-crystal graphene films by mechanical exfoliation, and the material exhibited a strong bipolar electric field effect [113]. Chen et al. reported a method to decompose silicon carbide into graphene at high temperature [114]. It was found that a gap of ~ 0.26 eV was created when graphene was epitaxial grown on SiC substrates. This gap decreases with increasing sample thickness and finally approaches zero when the number of layers exceeds four. The physicochemical and electronic properties of graphene can be dramatically changed by molecular and atomic doping. These molecules (oxygen, boron, nitrogen, phosphorus, sulfur, etc.) can donate or extract free electrons, tuning the properties of graphene through interacting molecules [119, 120]. Moreover, Sutter et al. transformed layered crystals into thin monolayer and few-layer flakes using slightly modifying micromechanical exfoliation strategy (Fig. 6(a)) [115]. In short, the substrate was first treated with oxygen plasma to remove environmental adsorbents. Then, additional heat treatment was brought in assuring well-distributed interface contact between the substrate and the bulk during the exfoliation procedure. This improved technology has enhanced the

production yield and area of nanosheets, which can be further utilized to prepare other large area and high yield 2D NMs. First-principles density functional calculations showed that the halogenated edges can provide good adsorption sites for oxygen molecules. Woo et al. synthesized B, N-doped graphene (BNGr) and P, N-doped graphene (PNGr) by additional doping B or P in N-doped graphene (NGr), respectively [121]. Compared with NGr, BNGr and PNGr not only enhanced the catalytic activity of nitrogen-doped graphene in ORR, but also improved the catalytic stability in strong acid environment. In addition, BNGr and PNGr effectively reduced the production of H₂O₂ in ORR, and the stability in acidic medium was significantly higher than that of noble metal catalyst Pt/C. It is particularly memorable that Gogotsi et al. successfully prepared a new type of MXenes material using a hydrofluoric acid etching strategy (Fig. 6(b)) [116]. This greatly enriches the family of two-dimensional nanomaterials. Compared to the hazardous and environmentally unfriendly hydrofluoric acid etching strategy, Huang and Gogotsi et al. developed a Lewis acid molten salt (LAMS) etching strategy that can etch and replace weakly bonded interlayer atoms in the M_{n+1}AX_n phase [122], synthesize a series of M_{n+1}AX_n phases containing transition metals and MXenes with pure halogen ends, and explore their applications as catalysts and ferromagnetic and electrochemical energy storage materials.

TMDs especially those with atomic thickness, have emerged as a new class of promising nanomaterials for fundamental research and applications due to their fascinating properties [123]. Electrocatalysis is one of the most promising applications of nanosheets of layered transition metal dichalcogenides nanosheets, especially in the HER [123, 124]. Compared with traditional noble metal catalysts such as Pt NPs, MoS₂ nanosheets have the advantages of low cost, high chemical stability and good catalytic performance. However, pure MoS₂ has problems such as limited active sites and inherent poor electrical transport properties. Therefore, scientists have developed different strategies to improve the catalytic performance of MoS₂ in the HER. For example, Xie et al. proposed a novel method for the controllable fabrication of defect-rich MoS₂ ultrathin nanosheets [125]. Additional active edge sites are exposed due to the large number of defects present in the ultrathin nanosheets that partially rupture the inert basal plane. In turn, the defect-rich MoS₂ ultrathin nanosheets exhibited higher HER activity than the amorphous MoS₂ nanosheets, showing a small onset overpotential of 120 mV, large current density, and low Tafel slope of 50 mV-dec⁻¹. In addition, Jaramillo et al. synthesized mesoporous MoS₂ nanosheets with a highly ordered double helix structure [126]. The high surface curvature of this mesoporous-structured catalyst exposes most of the edge sites, leading to excellent activity for electrocatalytic hydrogen evolution. Sun et al. synthesized MoS₂ nanosheets with edge-to-edge and interlayer extension properties by means of a microwave-assisted strategy [127]. The nanosheets presented high kinetic indices with an onset potential of -103 mV, and a low Tafel slope of 49 mV-dec⁻¹. In addition to electrochemical properties, some layered transition metal dichalcogenides have good photocatalytic/photoelectrocatalytic water splitting and photo-degradation properties [128–131]. For example, Ye et al. synthesized MoS₂/G-CdS ternary composites as cocatalysts for hydrogen production [132]. The hydrogen production performance of different catalysts was compared in lactic acid solution, and it was found that the MoS₂/G-CdS ternary composite catalyst had the highest photocatalytic activity for water splitting. Moreover, the catalytic rate of the ternary composite was about 1.6 mmol·h⁻¹ in the first hour and 9 mmol·h⁻¹ after 5 h of irradiation, which was better than that of the noble metal catalyst Pt/CdS (~ 0.276 mmol·h⁻¹). In addition, TMDs are also used in optoelectronic devices, which pose greater challenges for material

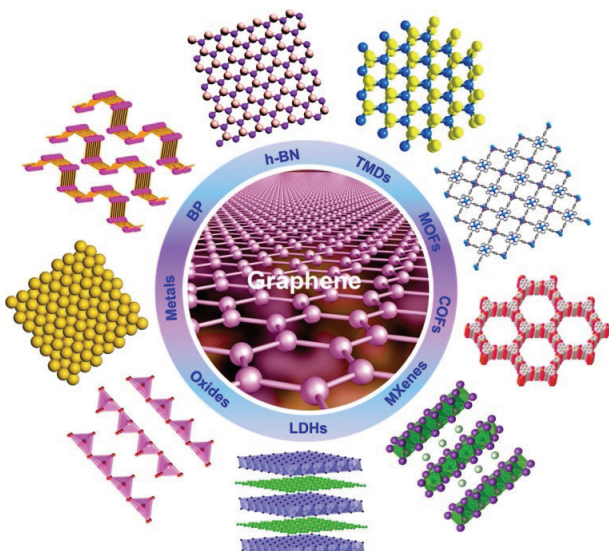


Figure 5 Schematic illustration of different kinds of typical ultrathin 2D nanomaterials, such as graphene, h-BN, TMDs, MOFs, COFs, MXenes, LDHs, oxides, metals, and BP. Reproduced with permission from Ref. [103], © American Chemical Society 2015.



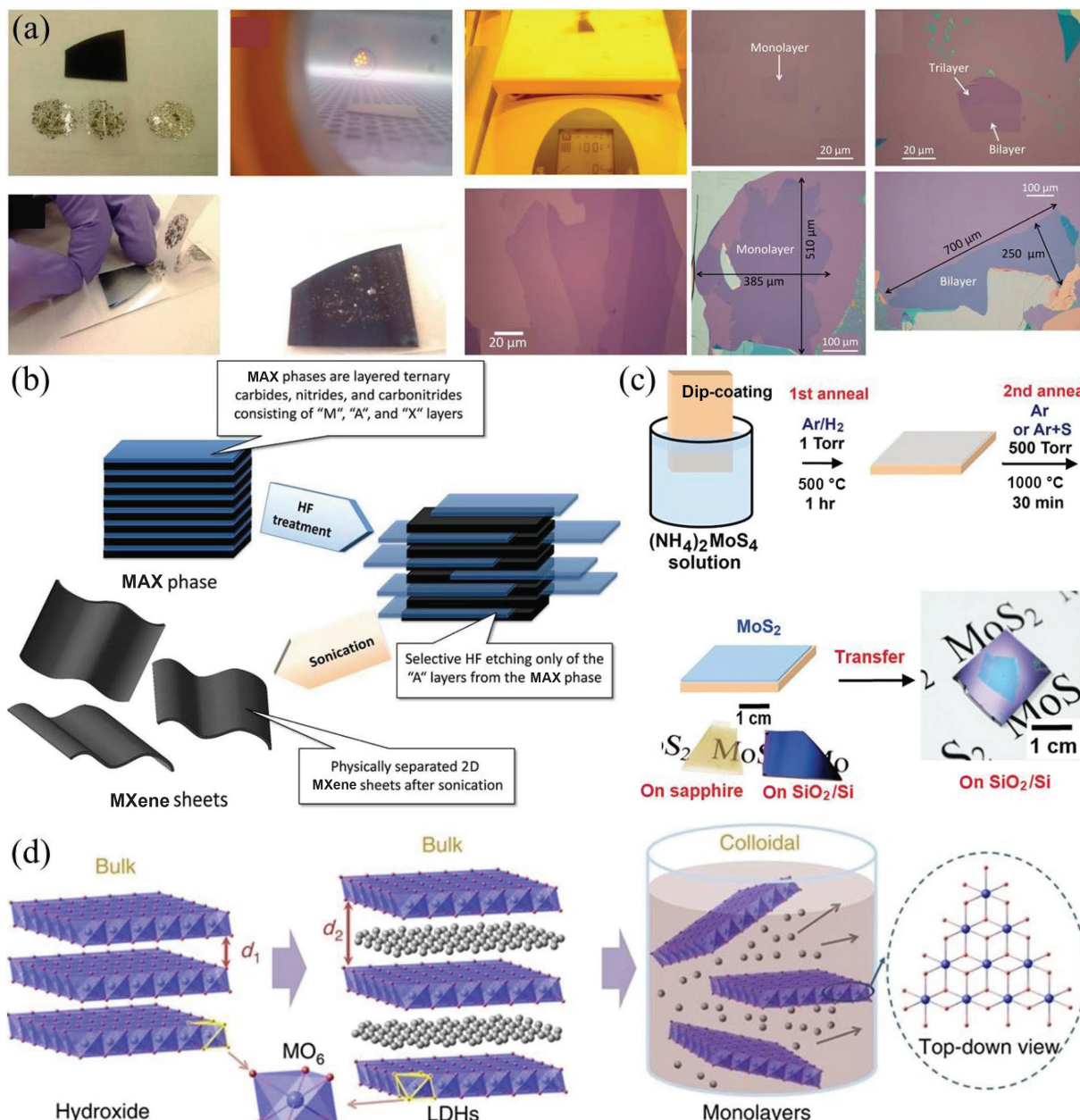


Figure 6 (a) Illustration of the modified exfoliation process for layered crystals (shown here for graphene) and optical images of graphene flakes prepared by the standard exfoliation method and our modified method. Reproduced with permission from Ref. [115], © American Chemical Society 2015. (b) Schematic for the exfoliation process of MAX phases and formation of MXenes. Reproduced with permission from Ref. [116], © American Chemical Society 2012. (c) Schematic illustration of the two-step thermolysis process for the synthesis of MoS₂ thin layers on insulating substrates. Reproduced with permission from Ref. [117], © American Chemical Society 2012. (d) Schematic representation of preparation of LDH structures. Reproduced with permission from Ref. [118], © Hu, X. et al. 2014.

design and synthesis. For example, Li and co-workers reported the large-area MoS₂ thin layers through two-step thermolysis process (Fig. 6(c)) [117]. In details, the (NH₄)₂MoS₄ precursor was firstly dip-coated on insulating substrate such as SiO₂/Si or sapphire. Then, the prepared MoS₂ film can be arbitrarily transferred to other supports. The 2D TMDs can also be used as electrode materials for lithium-ion battery due to their ultrathin thickness and lateral morphology, which endow them with high surface-to-volume ratios and short diffusion paths [133–135].

Due to the weak van der Waals interactions between adjacent layers, nanoflake layers had an opportunity to peel off the bulk material. The various transition-metal oxides nanosheets were synthesized by intercalation reaction of bulky guest species with host compounds (layered transition-metal oxides) in the solution [57, 118]. The liquid phase exfoliation method has the advantages of simple operation, no requirement of a third phase dispersant (i.e., a surfactant), and the high yield of production. This process

has been the most practical method to produce high-quality monolayer or multilayer nanoflakes. Hu et al. developed an orthogonal method to enhance the activity of LDH catalysts via liquid phase exfoliation strategy (Fig. 6(d)) [118]. In details, the CoCo and NiCo LDHs with Br⁻ anions were obtained by a topochemical method, whereas the NiFe LDH with CO₃²⁻ anions was prepared via a hydrothermal approach. To further increase the possibility for successful exfoliation, the inter-layer distance of LDHs was needed to be expanded. The inter-layer distances of CoCo and NiCo LDHs were increased from 7.8 to 8.7 Å by replacing Br⁻ with NO₃⁻; the NiFe LDH increased from 7.7 to 9.1 Å through using ClO₄⁻ to exchange with CO₃²⁻. Kim synthesized ultrathin 2D transition metal oxide (TiO₂, ZnO, Co₃O₄, and WO₃) by surfactant self-assembly or bottom-up growth strategy (Fig. 7) [57, 107, 136]. The amphiphilic block copolymers and short-chain alcohol co-surfactants were used as structure directing agents to control the stacking and growth directions of metal oxides. The

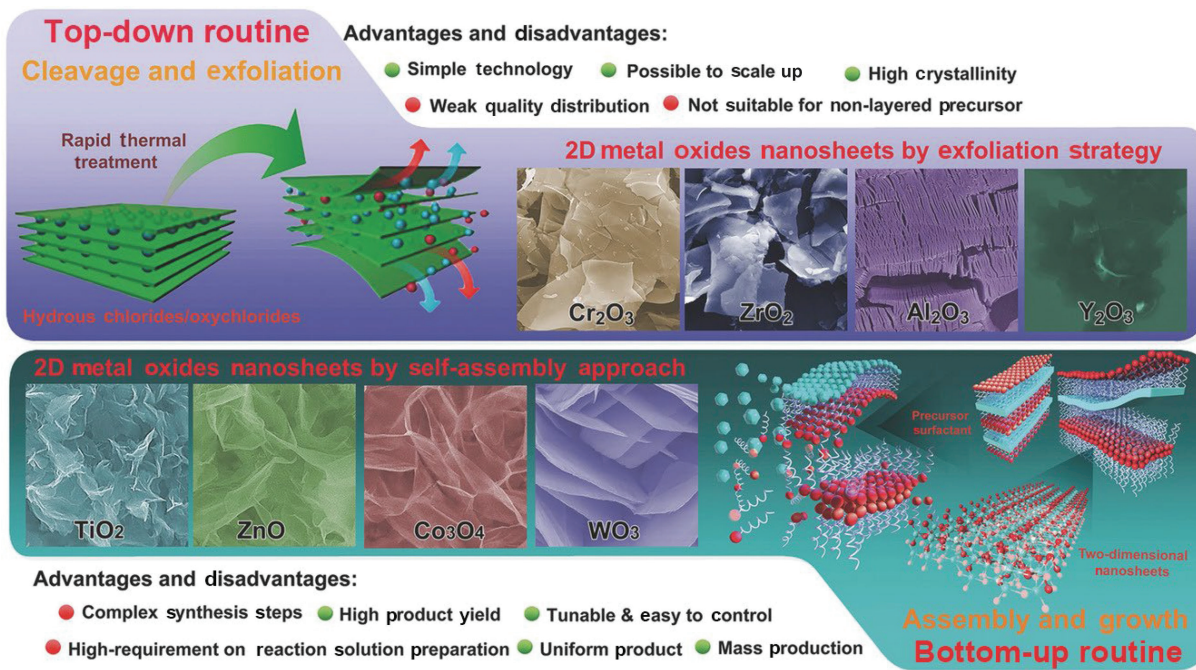


Figure 7 Strategies for the synthesis of 2D metal oxide nanosheets. For example, 2D Cr_2O_3 , ZrO_2 , Al_2O_3 , and Y_2O_3 nanosheets via top-down; 2D TiO_2 , ZnO , Co_3O_4 , and WO_3 nanosheets through bottom-up. Reproduced with permission from Ref. [57], © Wiley-VCH GmbH 2017.

fabricated nanosheets possessed the advantage of defined thickness, high surface area, high chemical activity, and quantum confinement effects, which can serve as the basis for energy generation/storage systems and emerging applications such as electronics and sensors. Different from the above method, Wu achieved the preparation of oxide nanosheets by rapid thermal annealing of corresponding [57, 107, 140]. By heating hydrous-chloride compounds, corresponding ultrathin Cr_2O_3 , ZrO_2 , Al_2O_3 and Y_2O_3 nanosheets were received (Fig. 7). Layered nanosheets stripped during the annealing process, as the rapid evaporation of water and/or other gas molecules. Such Cr_2O_3 nanosheets showed superior properties as anodes of lithium ion batteries compared to microcrystal counterparts.

2.2 Synthetic methods for SACs

SACs have emerged as a new type of material and usually refer to the isolated atoms (0.1–0.3 nm) dispersed on the support without interaction among the individual atoms. Designing and developing efficient synthetic methods for SACs has become one of the most important research priorities, which is also conducive to promoting its wide application. However, the high surface energy easily caused isolated single atoms to migrate and aggregate into particles [22, 141], which were challenging for preparing and maintaining atomically dispersed metal species under synthesis and realistic reaction conditions. Fortunately, multiple methods have been developed to successfully fabricate SACs, such as spatial confinement strategy [138, 139, 142–148], defect engineering strategy [149–158], coordination site design strategy [42, 158–168], impregnation and co-precipitation strategy [169–178], atomic layer deposition (ALD) strategy [179–182], transforming bulk metals or metal oxide powers into SACs [183–185], chemical etching strategy [186, 187], electrochemical method [188, 189], photochemical method [190, 191], freezing-assisted method [192, 193], microwave-assisted method [194], ball-milling method [195, 196] and ionic-liquid-assisted method [197]. At present, the SACs prepared by the above methods have covered all the elements, such as s-, d-, ds-, p- and f-block, of the periodic table, as shown in Fig. 8 [18, 28, 199, 200]. The following four methods were mainly introduced here.

2.2.1 Spatial confinement strategy

The spatial confinement strategy consists of two steps: 1) Using molecular channels of porous materials such as molecular sieves, MOFs, and COFs as “cages” to encapsulate and anchor mononuclear metal precursors, achieves its uniform spatial distribution and atomic-level dispersion; 2) in the process of removing the metal precursor ligands by post-treatment, the skeletons or the derivatives of the supports were used to stabilize the formed single atoms to prevent their migration and agglomeration, thereby realizing the fabricating of SACs. Using this method, the SACs of Ru, Fe and Pt were successfully prepared [137–139], as shown in Fig. 9. For example, Zhang et al. designed a click confinement strategy that can serve as a novel synthesis method to confine transition metal atoms in precursors and prepare M-N-C SACs [201]. The confinement strategy proposed in this study does not have strict requirements for molecular size or symmetry, which provides the possibility for expanding synthesis routes. In addition, this strategy will contribute to controllable and targeted catalyst synthesis based on the inherent advantages of click chemistry. The author successfully prepared Co-N-C SACs by clicking cobalt porphyrin sites onto conductive substrates through amination reaction using this confinement strategy. The prepared Co-N-C SACs exhibited excellent bifunctional ORR/OER electrocatalytic activity, which is better than most previously reported M-N-C SACs. The clicking confinement strategy designed in this study can effectively expand the method of preparing transition metal single atom sites, achieving efficient bifunctional oxygen electrocatalysis and rechargeable zinc-air batteries (ZABs) performance.

2.2.2 Defect engineering strategy

By constructing defect sites on the surface of the support, the C defects, O defects, S defects, and metal defects of the support are used as “traps” to capture single-nuclear metal precursors. Then, the charge-transfer effect between metal single atoms and defect sites is used to stabilize the formed single atoms, thereby realizing the synthesis of single-atom catalysis. Through this strategy, the Pt, Ni and Au single atoms were successfully obtained [151, 153, 157, 198], as shown in Fig. 10. Li et al. obtained efficient $\text{Pt}_1/\text{def-TiO}_2$



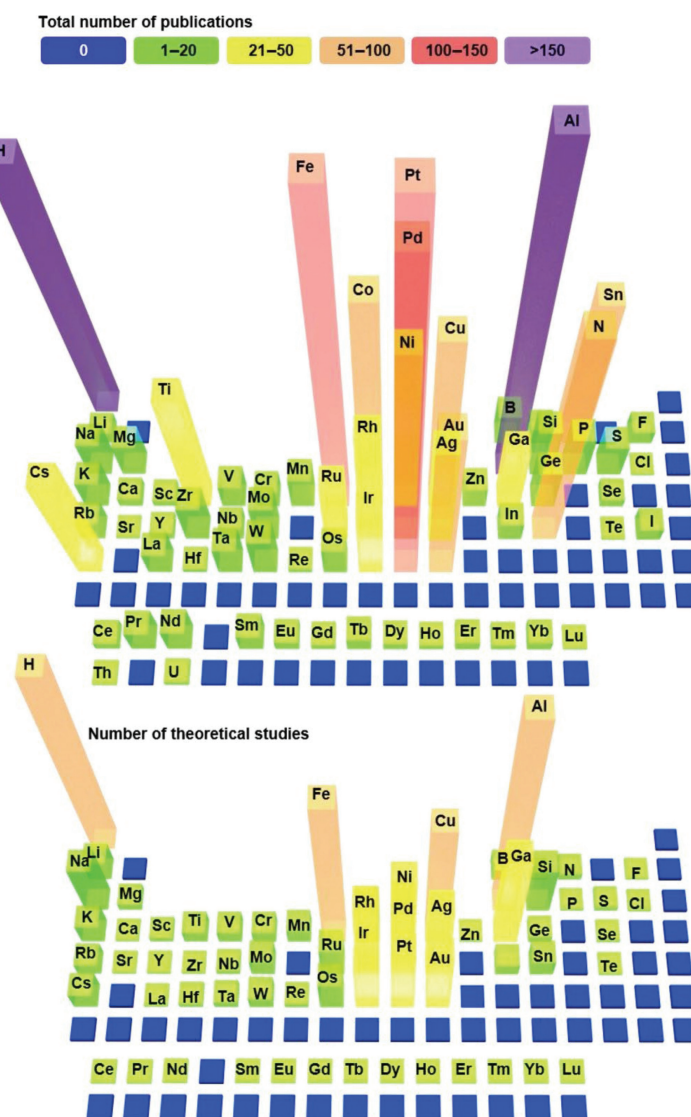


Figure 8 Publications on single-atom heterogeneous catalysts of all elements across the periodic table until May 2020. Reproduced with permission from Ref. [28], © American Chemical Society 2020.

single atom photocatalysts by anchoring individual Pt atoms using defect sites on defective TiO_2 supports [198]. Firstly, preparing sodium titanate precursor, and then the 0.1 M HCl aqueous solution containing $\text{H}_2\text{PtCl}_6 \cdot 6\text{H}_2\text{O}$ was injected into a sodium titanate nanotubes suspension under intense stirring. Subsequently, titanate was converted into anatase TiO_2 support at 400 °C calcination in air. Finally, a Pt single atom photocatalyst ($\text{Pt}_{\text{i}}/\text{def}-\text{TiO}_2$) loaded on defective TiO_2 was obtained after low-temperature reduction treatment in a 5% H_2/Ar atmosphere at 160 °C. Spherical aberration corrected TEM and X-ray absorption fine spectroscopy (XAFS) characterization fully demonstrated the existence of platinum species as isolated atoms, and the charge transfer between Pt single atoms and surrounding O atoms enhanced the metal–support interaction. The research results found that the presence of a single Pt atom promoted the construction of the Pt–O– Ti^{3+} atomic interface, which was conducive to the separation of electron hole pairs, inhibited electron hole recombination, and thus improved the photocatalytic hydrogen production efficiency.

2.2.3 Coordination site design strategy

Constructing coordination sites and coordinating groups similar to "claws" on the surface of the support were used to capture and anchor the mononuclear metal precursor. Then, the strong interaction between the metal single atom and the coordination

site was used to stabilize the formed single atom. In addition, the strong interaction also prevented the migration and aggregation of prepared single atom. Therefore, the SACs were successfully fabricated. This is one of the methods often used to construct single atoms. The rational use of this method has successfully achieved the synthesis of SACs such as Pt, Ir, Au, Pd, Ru, Co and Fe etc. [160, 162, 165, 202–206], as shown in Fig. 11. For example, Tan et al. developed a "gelation-and-pyrolysis" process to fabricate a series of single-atom metal sites (Pt, Ir, Ru, Pd and Au) on three-dimensional porous $\text{Ti}_3\text{C}_2\text{T}_x$ nanosheets with N and P co-doping (expressed As $\text{M}_1\text{SA-PNPM}$, $\text{M}_1 = \text{Pt, Ir, Ru, Pd, and Au}$) [206]. The aberration-corrected high-angle annular dark-field scanning transmission electron microscopy (AC-HAADF-STEM) measurements and XAFS confirmed that the single-atom metal sites (Pt, Ir, Ru, Pd and Au) were existed in isolation and homogeneous distribution condition, and coordinated with both N(O) and P on $\text{M}_1\text{SA-PNPM}$ nanosheets. Among, the Pt SA-PNPM presented superior electrocatalytic hydrogen evolution activity and stability over a wide pH range, comparable to commercial Pt/C electrodes. Through XAFS measurements and DFT calculation analysis, the unique electronic structure of Pt single atomic sites coordinated with nitrogen and phosphorus can dramatically optimize the adsorption energy of hydrogen intermediates and improve their inherent catalytic performance. This work provides direction for the development of MXene

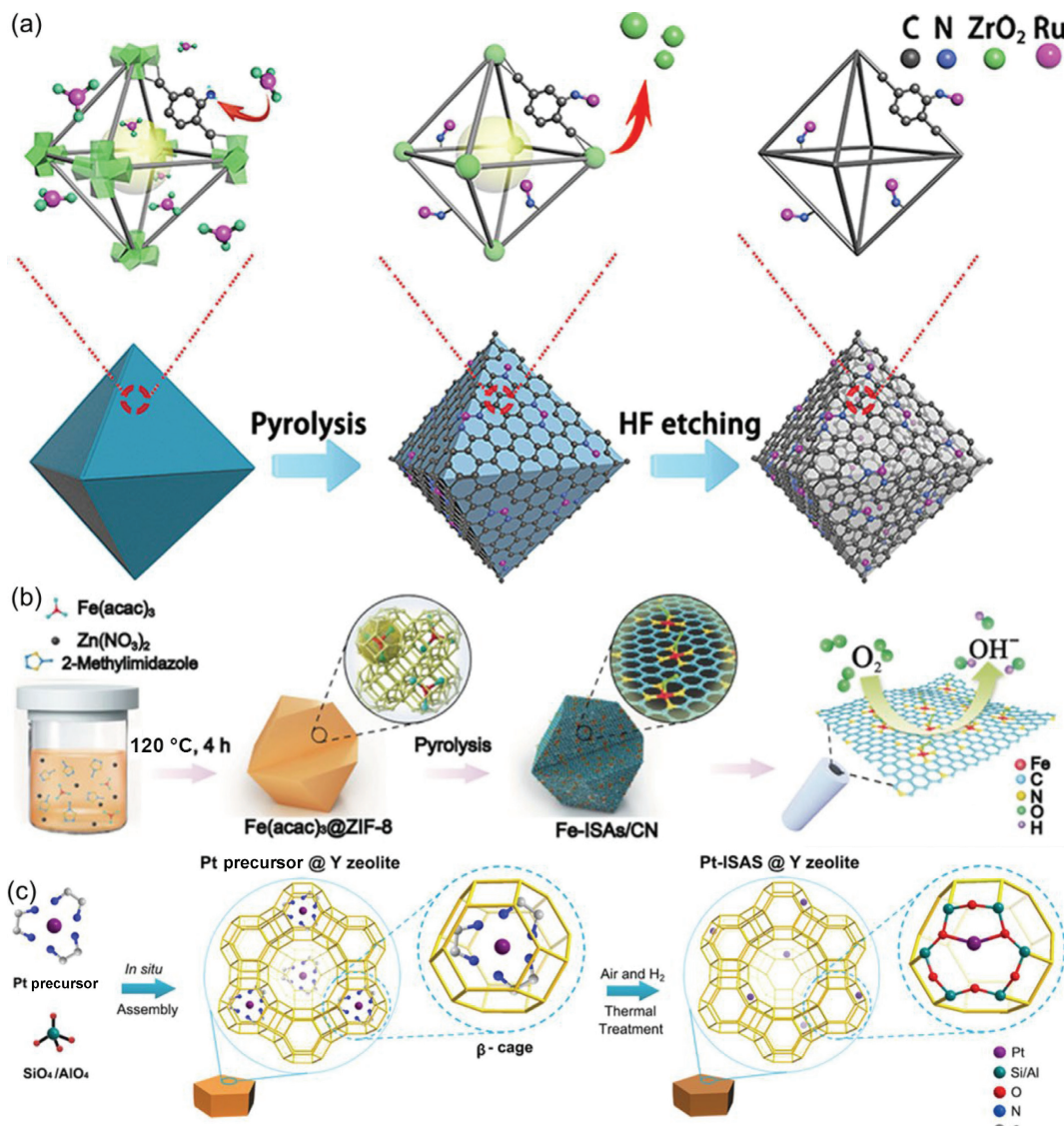


Figure 9 (a) Formation procedures of single Ru atoms immobilized on the carbonized skeleton of UiO-66-NH₂. Reproduced with permission from Ref. [137], © American Chemical Society 2017. (b) Synthetic process for Fe-ISAs/CN. Reproduced with permission from Ref. [138], © Wiley-VCH 2017. (c) Schematic illustration of the *in situ* separation and confinement of a platinum precursor in a β -cage followed by thermal treatment. Reproduced with permission from Ref. [139], © American Chemical Society 2019.

based supported single atom catalysts and highlights the combination of coordination structure modulation and geometric structure design to construct high-activity electrocatalysts.

2.2.4 Atomic layer deposition strategy

ALD was also known as single atom layer deposition or atomic layer epitaxy [207–209]. It is a method in which substances can be plated on the surface of the substrate layer by layer in the form of a single atomic film. In atomic layer deposition, the chemical reaction of a new layer of atoms was directly linked to the previous layer, in such a way that only one layer of atoms was deposited per reaction. The advantage of ALD technology laid in the successive deposition of single atomic layers, ensuring extremely uniform thickness and excellent consistency of the deposited layer. Through this strategy, the single atoms Pt, Pd, Co, Cu, Fe, Ti and Zn were successfully prepared [181, 182, 210, 211], displayed in Fig. 12. For instance, Botton et al. used ALD technology to prepare a N-doped graphene supported Pt based catalyst for HER [182]. The size range of the obtained Pt catalyst ranged from single atoms, sub nanoclusters, to nanoparticles, which can be precisely controlled by adjusting the number of ALD cycles to accurately control the size of the prepared Pt species. Compared with

commercial Pt/C catalysts, individual Pt atoms and atomic clusters exhibited superior high HER activity and long-term stability. The significance of single Pt atoms and clusters was attributed to their small size and the unique electronic structure of the adsorption of single Pt atoms on N-doped graphene, which was confirmed by X-ray absorption near edge structure (XANES) and DFT analysis. This work provided a new method for the design of next-generation catalysts with high performance and durability based on single Pt atoms and clusters, which have a great potential to decrease the high price of industrial noble-metal catalysts.

3 Structure–activity relationships guided catalysts design

The structure–property relationships of catalysts include several aspects such as composition, crystal structure, morphology, surface active sites, electronic structure and energy band structure [213]. The composition of catalyst plays a crucial role in its catalytic activity. Different combinations of elements and compounds can lead to different catalytic activities and selectivities. Common catalyst compositions include metals [214, 215], alloys [216–218], metal oxides [219–222], metal sulfides

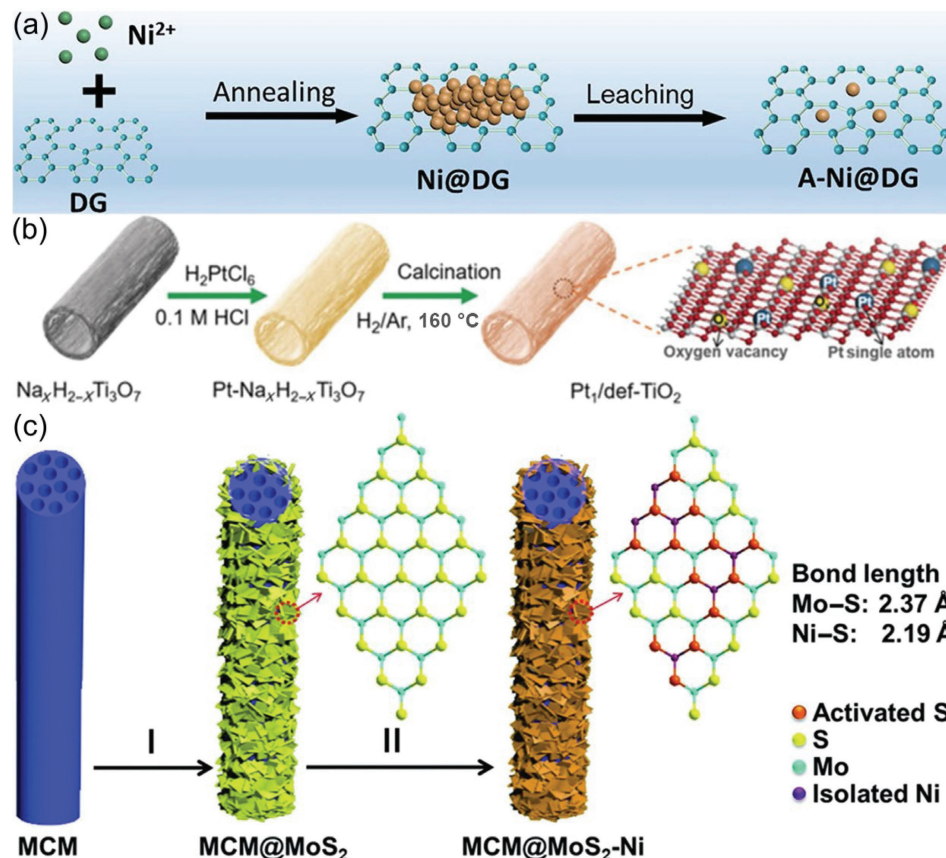


Figure 10 (a) Schematic preparation of A-Ni@DG. Reproduced with permission from Ref. [153], © Elsevier Ltd. 2018. (b) Schematic illustration of synthesis procedure for the Pt₁/def-TiO₂. Reproduced with permission from Ref. [198], © Wiley-VCH GmbH 2019. (c) Schematic illustration of the synthetic process for MCM@MoS₂-Ni. Reproduced with permission from Ref. [157], © Wiley-VCH GmbH 2018.

[223–228], etc. Metals are common catalyst types in catalysts. Different metals have different catalytic activity and stability. Commonly used metal catalysts include platinum [31], iron [229, 230], nickel [231], cobalt [230], etc. Platinum is a widely used and efficient electrocatalyst with good catalytic activity and stability, but at a higher cost. Other metals such as iron, nickel and cobalt have lower costs, but relatively poor catalytic activity and stability. Pt based catalysts with different morphologies, compositions, crystal structures and facets have different catalytic properties (Fig. 13) [212].

3.1 Alloying effects

The catalytic performance of catalysts can be modified by forming alloys of two or more metals [232, 233]. Alloying can modulate metal interactions and improve catalytic activity and stability. For example, platinum alloy catalysts offer higher catalytic activity and better durability, while reducing cost. Li group reported a Cu atom-pair stabilized by the Te surface defects on Pd₁₀Te₃ alloy nanowires (Fig. 14(a)) [234]. We demonstrate its high activity and Faradaic efficiency to selectively produce CO (FE_{CO}) in CO₂RR at low applied overpotentials. The competing HER is almost completely suppressed when an atom-pair catalyst (APC) is used; in sharp contrast, HER dominates when the pure Pd₁₀Te₃ nanowire is used as catalyst. Wang et al. reported a highly efficient and stable Pt₃Sn electrocatalyst with defect rich Pt atomic layers coating an ordered intermetallic core (Fig. 14(b)) [235]. The creation of 4.4% tensile strain in the [001] direction is made possible by Pt atomic layers. The performance of ethanol electrooxidation is significantly improved by Pt atomic-layer catalyst (Pt atomic-layer) due to the synergistic surface and strain engineering controls. In addition, compressive or tensile strain can also lead to alloy catalysts with better catalytic properties. Huang group reported a highly efficient

and stable PtPb/Pt core-shell hexagonal nanoplates with large biaxial tensile strain for boosting ORR activity (Fig. 14(c)) [236]. They found that at a very high tensile strain, the Pt (110) plane located outside the nanoplates can exhibit the superior electrocatalytic activity for ORR. The PtPb/Pt nanoplates show negligible activity decay and no obvious structure and composition changes after a 50,000-cycle electrochemical accelerated durability test (ADT). Besides the core-shell alloy catalysts, other transition metal-doped alloy catalysts also exhibit better catalytic performance. Huang group reported a Mo surface-doped octahedral Pt₃Ni nanocrystal, which shows exceptional catalytic performance (Fig. 14(d)) [237]. The Mo doping is possible to fine-tune the chemical and electronic properties of the surface layer and increase the oxygen binding energies at sites and hence modulate its catalytic activity.

In the “alloying effect”, the relationship between alloying metal and catalytic performance usually exhibited the following aspects: 1) By adjusting the surface stress and surface coordination of alloying metals, the adsorption of alloy catalysts and catalytic intermediates is optimized, that is, by adjusting the binding strength of M–O intermediates through ligand and strain effects, the catalytic activity and stability are effectively improved [238, 239]; 2) the alloying effect can regulate electronic and lattice strain, improve the catalytic performance of alloy metal catalysts, weaken the poisoning phenomenon of catalysts, and improve the activity and stability of catalysts [240, 241]; 3) Optimize the d-band center of the metal catalytic center through alloying, achieve adsorption of catalytic species intermediates, reduce energy barriers, and promote reaction progress [242].

3.2 Metal–support interactions effect

Catalysts are usually loaded on a support material to increase its

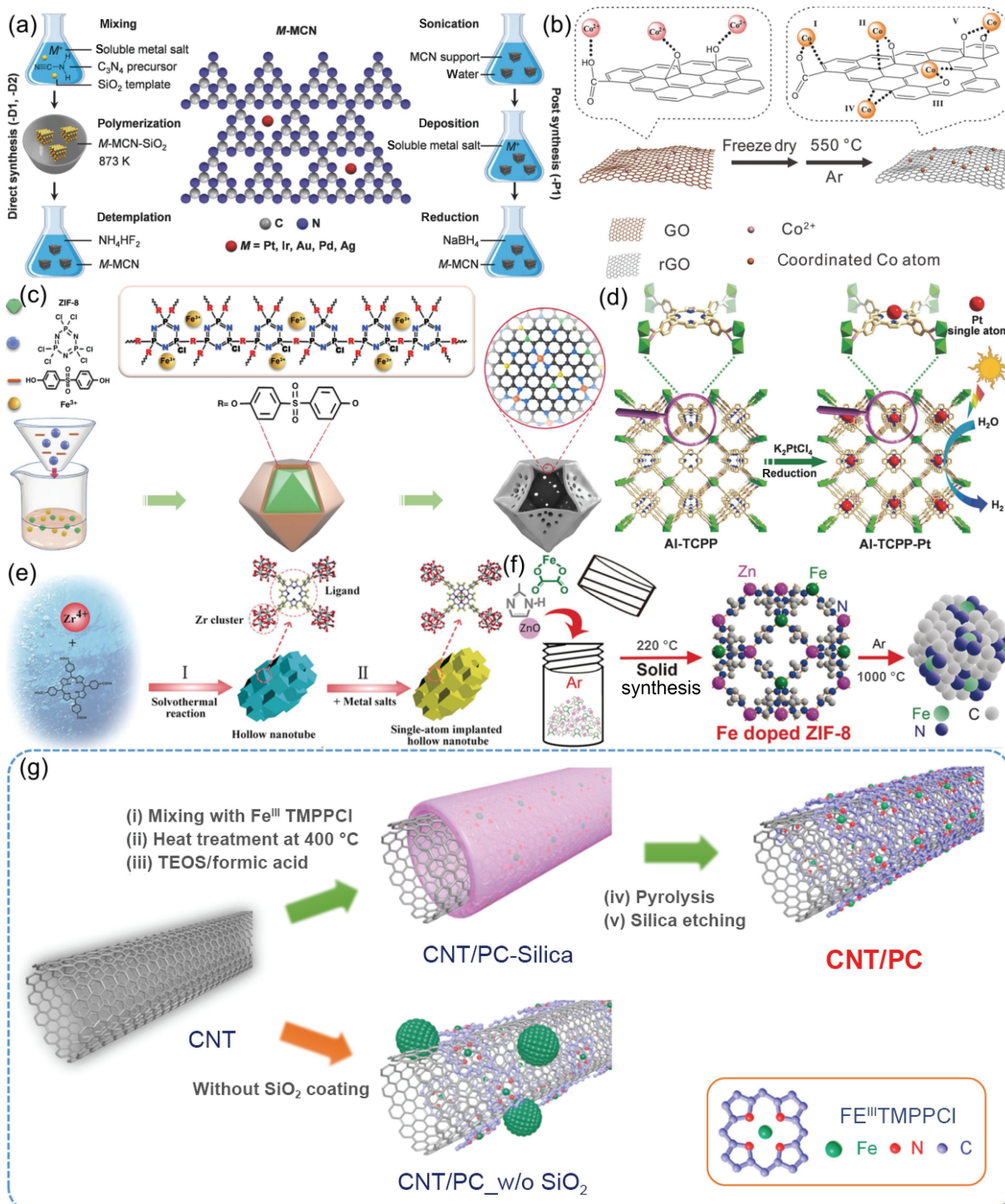


Figure 11 (a) Direct synthesis (-D1, -D2) and postsynthesis (-P1) approaches to stabilize metal atoms within $\text{g-C}_3\text{N}_4$ exemplified for the mesoporous MCN support. Reproduced with permission from Ref. [202], © Wiley-VCH GmbH 2017. (b) Schematic illustration for the SACs synthetic procedure of the $\text{Co}_1\text{-G}$ catalyst. Reproduced with permission from Ref. [160], © Wiley-VCH GmbH 2018. (c) Illustration of preparation process of single iron atomic sites supported on a nitrogen, phosphorus and sulfur co-doped hollow carbon polyhedron (Fe-SAs/NPS-HC). Reproduced with permission from Ref. [203], © Li, Y. et al., under exclusive license to Springer Nature Limited 2019. (d) Schematic illustration showing the synthesis of Al-TCPP-Pt for photocatalytic hydrogen production. Reproduced with permission from Ref. [204], © Wiley-VCH GmbH 2018. (e) Formation of the hollow nanotube MOF and the single-atom-immobilized hollow nanotube of HNTM-Ir/Pt. Reproduced with permission from Ref. [162], © Wiley-VCH GmbH 2018. (f) Formation of SACs Fe/N-C derived from Fe-doped-ZIF-8. Reproduced with permission from Ref. [205], © Wiley-VCH GmbH 2018. (g) Synthetic scheme for the preparation of CNT/PC catalysts. Reproduced with permission from Ref. [165], © American Chemical Society 2016.

surface area and stability. Commonly used support materials include carbon materials, oxides (e.g., silica, alumina, etc.) and nitrides [243–249]. In general, the supports can enhance the metal atom utilization, stabilize the metal active centers, and even participate in chemical reactions process based on metal–support interaction [250–254]. It can provide a large specific surface area, enhance the interaction between the electrocatalyst and the

electrolyte, and protect the catalyst from corrosion at the same time. Isolated single atomic site catalysts have attracted a great amount of interest in recent years owing to their excellent properties in fields of fuel cells, photocatalysis, and organic catalysis. Because of their high surface energy, single atoms are highly mobile and tend to form aggregate during synthetic and catalytic processes. Therefore, it is a significant challenge to

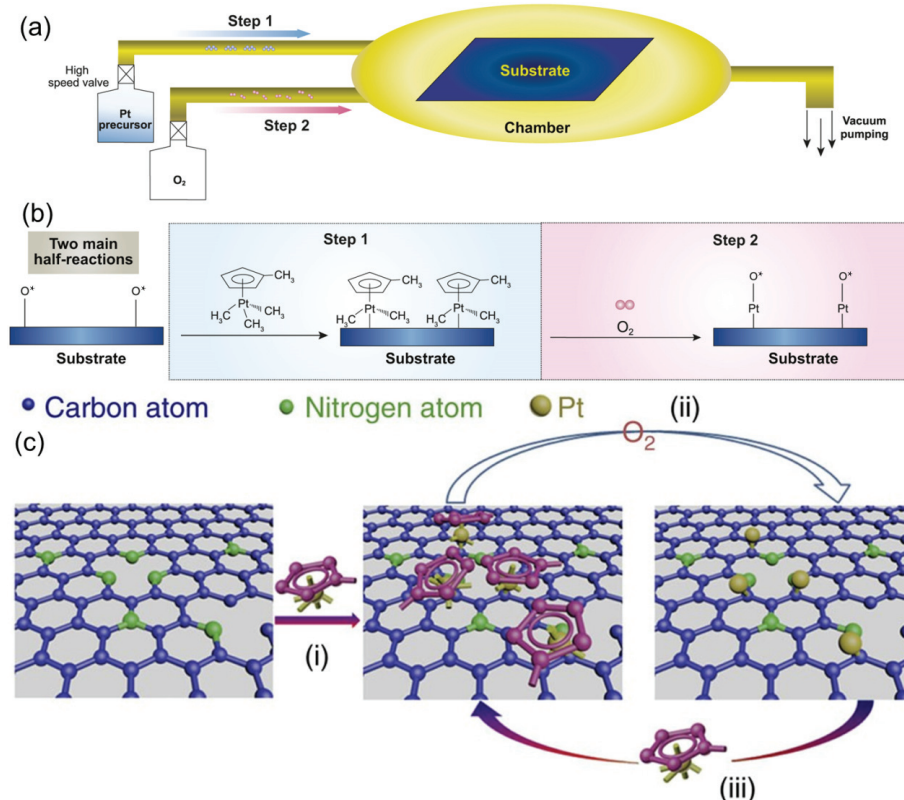


Figure 12 (a) Schematic illustrations of the deposition of single-atomic Pt on substrates through the ALD method. (b) The detailed two main half-reactions during a whole ALD cycle. Reproduced with permission from Ref. [181], © Oxford University Press 2018. (c) Schematic illustration of the Pt ALD mechanism on NGNs. Reproduced with permission from Ref. [182], © Sun, X. et al., under exclusive license to Springer Nature Limited 2016.

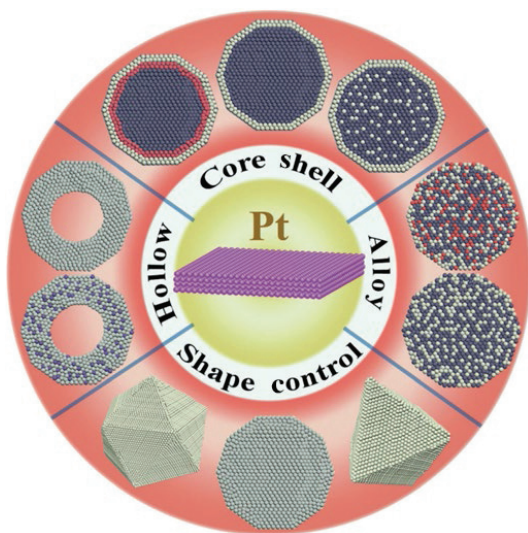


Figure 13 (a) Recent important advances in new active and durable Pt based nanostructures for improved ORR catalysis. Reproduced with permission from [212], © Wiley-VCH GmbH 2015.

fabricate isolated single atomic site catalysts with good stability. Li et al. reported a gentle method to stabilize single atomic site metal by constructing defects on the surface of supports is presented (Fig. 15(a)) [255]. The single atomic site Au supported on defective TiO₂ nanosheets is prepared and it is discovered that the surface defects on TiO₂ nanosheets can effectively stabilize Au single atomic sites through forming the Ti-Au-Ti structure. The Ti-Au-Ti structure can also promote the catalytic properties through reducing the energy barrier and relieving the competitive adsorption on isolated Au atomic sites. The Gogotsi group also used electrochemically exfoliated MXene nanosheets with abundant Mo vacancies for immobilization of individual Pt atoms

to enhance the catalytic activity of MXene for hydrogen precipitation reactions (Fig. 15(b)) [256]. The developed catalyst exhibits a high catalytic ability with low overpotentials of 30 and 77 mV to achieve 10 and 100 mA·cm⁻² and a mass activity about 40 times greater than the commercial platinum-on-carbon catalyst. Sun et al. anchored platinum nanoparticles (Pt NPs) on LiCoO₂ nanosheets to construct multi-functional active center transferable heterostructure electrocatalysts (Fig. 15(c)) [257]. In this electrocatalyst system, the active center can be alternatively switched between Pt species and LiCoO₂ for HER and OER, respectively.

In addition, Li's group reported a simple and practical strategy to synthesize a palladium single-atom catalyst supported on bulk nitrogen-doped carbon foams (Pd-SAs/CNF) [258]. The unique electronic structure of the Pd single-atom site gives the catalyst an isolated site effect, resulting in excellent activity and selectivity in the semi-hydrogenation reaction of 4-nitrophenylacetylene (NPA). This isolated site effect allows Pd-SAs/CNF to preferentially adsorb alkynyl groups over nitro and inhibits further hydrogenation of alkenyl groups due to limited coordination space, leading to the catalytic generation of NPA semi-hydrogenation with ~ 99% conversion and ~ 99% selectivity. Recently, MXenes with oxygen vacancies (O_V) as the active center have shown excellent catalytic performance in photocatalytic aerobic oxidation reactions.

3.3 Crystal structure and morphology

The crystal structure and morphology of catalyst have a significant effect on its catalytic activity. The crystal structure determines the accessibility and arrangement of the active sites on the surface of the catalyst, while the surface morphology can provide more active sites and increase the contact area between the catalyst and the reactants [259, 260]. The morphology of nanoparticles in catalysts has an important effect on the catalytic performance. Smaller size

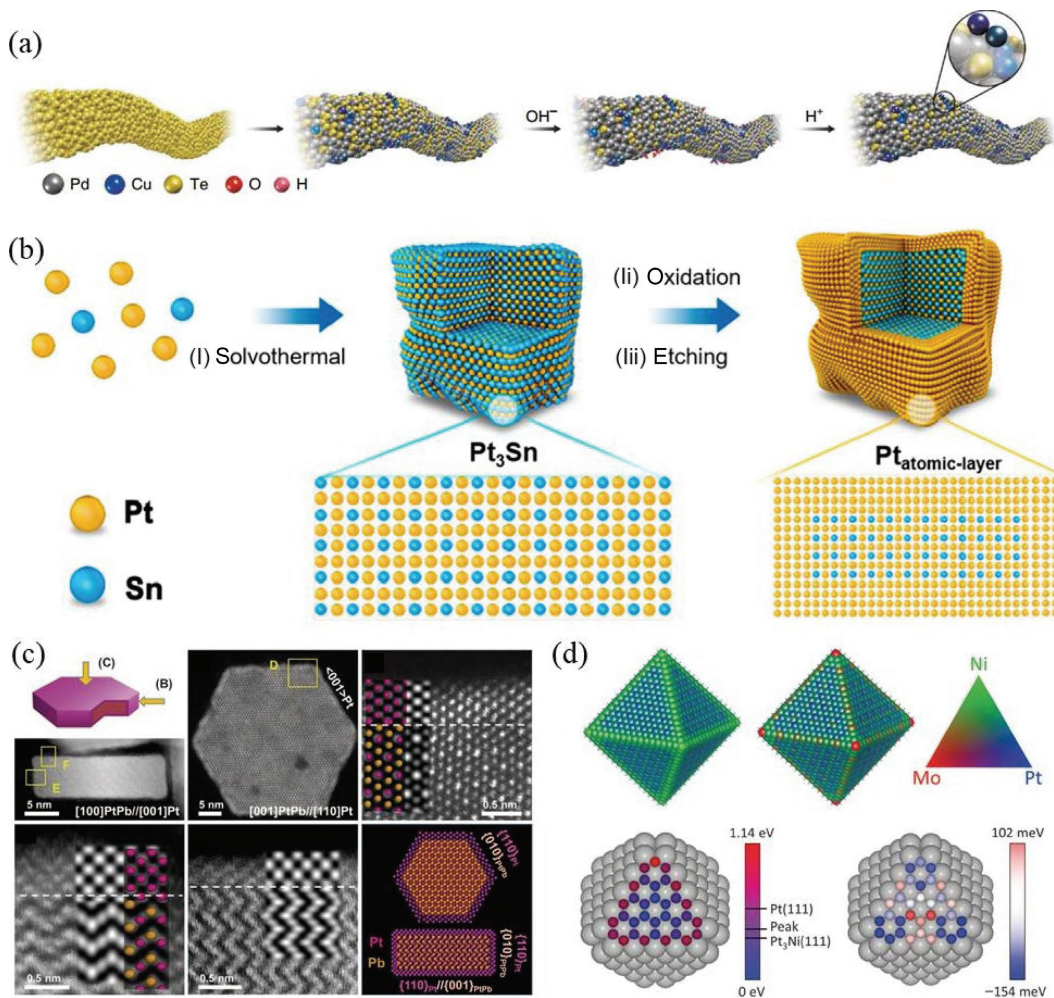


Figure 14 (a) Schematic illustration of the Cu-doped Pd₁₀Te₃ nanowires. Reproduced with permission from Ref. [234], © Li, Y. et al., under exclusive license to Springer Nature Limited 2019. (b) Scheme of synthetic processes of Pt₃Sn intermetallic nanocrystals. Reproduced with permission from Ref. [235], © American Chemical Society 2022. (c) Structure analysis of PtPb/Pt nanoplates. Reproduced with permission from Ref. [236], © American Association for the Advancement of Science 2016. (d) The surface structures for computational results of Mo-Pt₃Ni/C catalysts. Reproduced with permission from Ref. [237] © American Association for the Advancement of Science 2015.

of catalyst have larger specific surface area and more surface active sites, which can enhance the contact between reactants and catalysts and thus enhance the catalytic activity [260–262]. By adjusting the morphology and size of catalysts, the activity of catalysts can be optimized and enhanced. Crystal structure refers to the arrangement of atoms or molecules in a catalyst. Differences in crystal structure can affect the accessibility and properties of the surface active sites for catalyst, which in turn affects the catalytic performance. In recent years, research on surface regulation of catalysts, especially defect chemistry, has received widespread attention [263]. Systematic research progress has been made in designing and regulating the performance of materials through the combination of defect engineering [264]. Defects commonly exist in the preparation and application of materials, which can be used as active site to realize the preparation of specific catalyst materials, and also can be used to promote the occurrence of catalytic reactions. Defect engineering is an effective way to regulate the surface physical/chemical properties of catalytic materials. The presence of defects will significantly change their electronic structure and chemical properties, promote the formation of new physical and chemical properties or strong synergistic effects, and thus optimize the catalytic performance of catalysts [265–267]. Moreover, different exposed crystalline surfaces have different catalytic performance [268–271]. In addition, the crystal structure can also affect the surface diffusion properties, electron transport properties and stability of the catalyst, thus having an impact on

the rate and selectivity of the catalytic reaction. Duan et al. reported a transformation of PtNi alloy nanowires into jagged Pt nanowires by electrochemical alloying (Fig. 16(a)) [272]. The high exposure ratio jagged Pt nanowires have an electrochemical active surface area (ECSA) of up to 118 m²·g⁻¹ of Pt and a specific activity of 11.5 mA·cm⁻² for ORR, and a mass activity of 13.6 A·mg_{Pt}⁻¹. Molecular dynamics (MD) simulations suggest that the highly stressed, undercoordinated rhombus-rich surface structure of the jagged Pt nanowires enhances ORR activity.

The surface morphology of a catalyst refers to the shape, structure and characteristics of its surface. The surface morphology has a significant influence on the catalytic performance of catalysts. On the one hand, surface morphology can regulate the specific surface area and the distribution of active sites on the surface of catalysts, thus increasing the catalytic activity [273–275]. High specific surface area and more active sites can provide more active sites and increase the probability of adsorption and desorption of reactants. On the other hand, the surface morphology can also influence the interfacial interaction and diffusion properties between catalyst and reactants, which in turn affects the reaction rate and selectivity [276–279]. For example, nanostructured surfaces can provide a higher density of localized surface active sites to promote catalytic reactions. Xia et al. group reported a one-dimensional bunched platinum-nickel (Pt-Ni) alloy nanocages with a Pt-skin structure for the oxygen reduction reaction. The catalyst exhibits high stability with

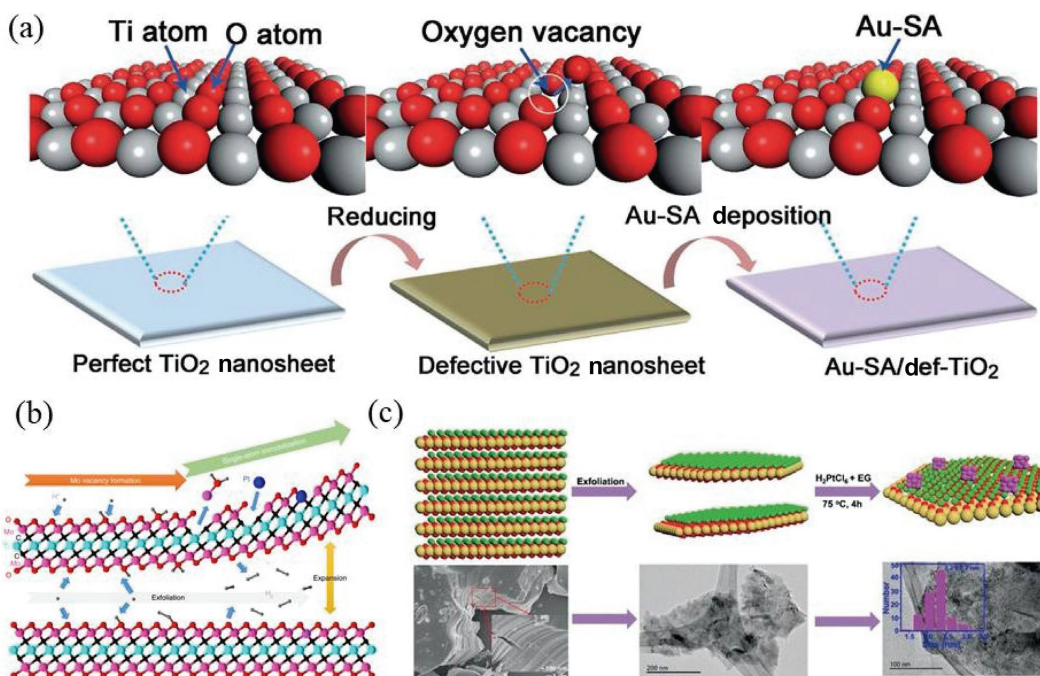


Figure 15 (a) Schematic illustration of synthesis procedure and the results of Au-SA/Def-TiO₂. Reproduced with permission from Ref. [255] © Wiley-VCH GmbH 2018. (b) Illustration of the synthesis mechanism for Mo₂TiC₂O₂-PtSA during the HER process. Reproduced with permission from Ref. [256] © Gogotsi, Y. et al., under exclusive license to Springer Nature Limited 2018. (c) Synthesis and microscopic characterization of Pt/LiCoO₂ heterostructures. Reproduced with permission from Ref. [257] © Wiley-VCH GmbH 2020.

negligible activity decay after 50,000 cycles as compared with a commercial platinum on carbon (Pt/C) catalyst (Fig. 16(b)) [239]. Control of structure at the atomic level can precisely and effectively tune catalytic properties of materials, enabling enhancement in both activity and durability. Vojislav et al. synthesized a highly active and durable class of electrocatalysts by exploiting the structural evolution of platinum-nickel (Pt-Ni) bimetallic nanocrystals (Fig. 16(c)) [280]. The starting material, crystalline PtNi₃ polyhedra, transforms in solution by interior erosion into Pt₃Ni nanoframes with surfaces that offer three-dimensional molecular accessibility. Both the interior and exterior catalytic surfaces of this open-framework structure are composed of the nanosegregated Pt-skin structure, which exhibits enhanced ORR activity.

In general, crystal structure and surface morphology can have important effects on catalytic activity, selectivity and stability of catalysts by regulating the active site distribution, interfacial interactions and diffusion. Therefore, the effects of crystal structure and morphology need to be considered comprehensively when designing and optimizing the catalysts, and the ideal catalytic performance needs to be achieved by appropriate preparation and modification methods.

3.4 Surface active sites

The catalytic performance of an electrocatalyst is closely related to the type, density and availability of its surface active sites. The active sites can be atoms, edge sites, etc. on the metal surface, or functional groups on the surface [281–285]. Surface active sites are able to interact with reactants, providing sites for adsorption and reaction. The highly efficient sites usually have specific structures and compositions that make chemical bond formation, breaking and transfer with reactants easier [15, 16, 284, 286]. A higher density of reactive sites can increase the contact between the reactants and the catalyst and increase the reaction rate. For example, in metal catalysts, the metal atoms on the surface are often active sites that provide efficient electron transfer and reactivity.

Different type of coordination elements has different effects on the reaction selectivity and activity. Jiang et al. synthesized three types of carbon supported Pt single atom catalyst with varied neighboring dopants and Pt site densities (Pt-X-C) to investigate the local coordination environment effect and regulate the selectivity of 2e⁻ or 4e⁻ ORR pathway (Figs. 17(a) and 17(b)) [287]. Through a combined experimental and theoretical approach, it showed that manipulating the local coordination environment of Pt single atoms could effectively regulate the ORR pathway. The Pt-S-C moiety is inclined to the 2e⁻ pathway of O²⁻ to H₂O₂ conversion while Pt-C moiety is mostly favorable to the 4e⁻ pathway of O₂ into H₂O. Specifically, the coordination pattern influences not only the structure and electronic properties of the catalysts, but also the catalytic reaction pathway and the formation of intermediates.

Different types of active sites may have different selectivity for different reactants. Active sites with specific structures or compositions may be more favorable for certain reaction pathways, thus affecting product selectivity. By controlling the structure and distribution of active sites, the selectivity of the catalyst can be modulated. In order to investigate the effect of different coordination numbers on the catalytic performance, Chen et al. reported a polymerization pyrolysis strategy for synthesizing different coordination environment of single-atom Fe-based catalysts, and presented a systematic study on the coordination effect of Fe-N_xC_y catalytic sites in benzene oxidation reaction (BOR) (Figs. 17(c) and 17(d)) [288]. The results demonstrate that Fe atoms anchored by four-coordinating N atoms exhibit the highest BOR performance with benzene conversion of 78.4% and phenol selectivity of 100%. The increase of Fe-N coordination number facilitates the generation and activation of the crucial intermediate O=Fe=O species, thereby enhancing the BOR activity.

3.5 Electronic and energy band structures

The electronic and energy band structures of catalysts also play an important role in the activity and selectivity of catalytic reactions.

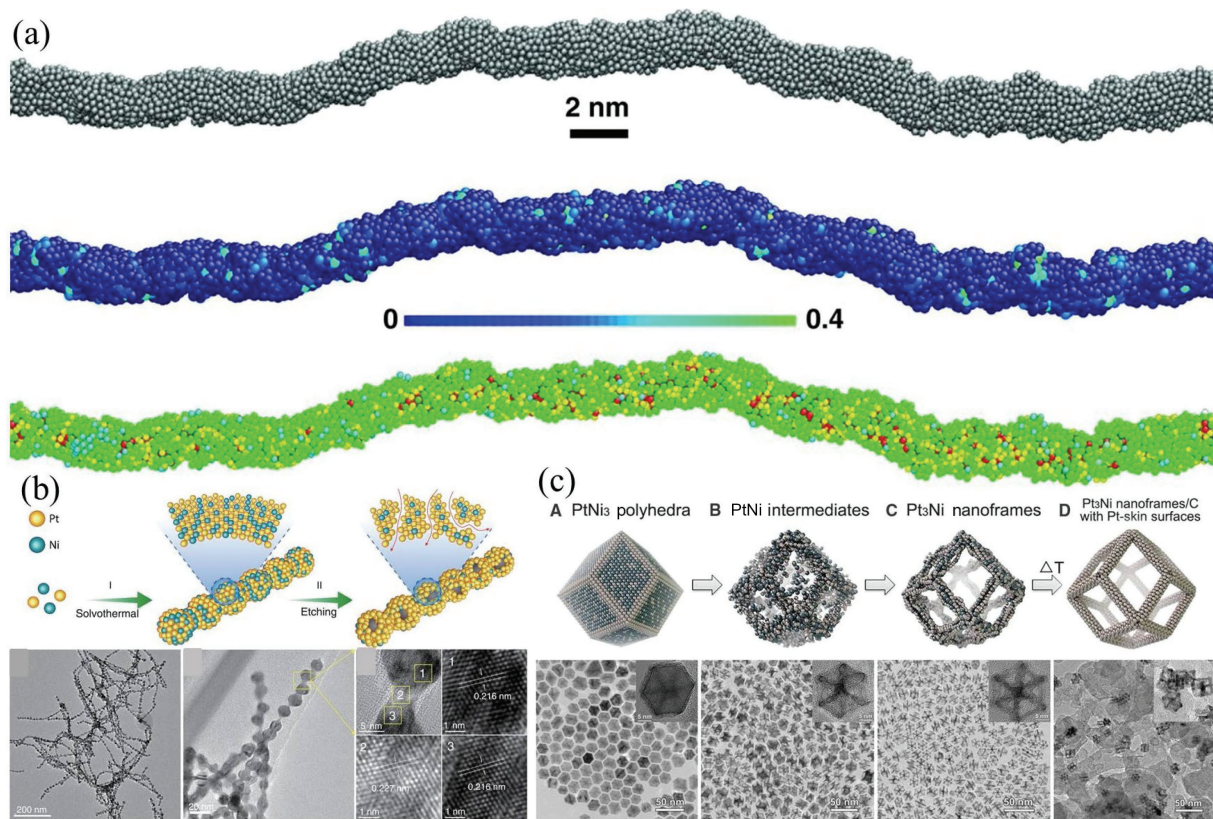


Figure 16 (a) Schematic structural illustration and its picture of the final structure generated by reactive molecular dynamics simulations and the distribution of atomic stress of the jagged Pt nanowires. Reproduced with permission from Ref. [272] © American Association for the Advancement of Science 2016. (b) Structural and compositional characterizations of Pt_{1.5}Ni-BNSs. Reproduced with permission from Ref. [239] © American Association for the Advancement of Science 2019. (c) Schematic illustrations and corresponding TEM images of the samples obtained at four representative stages during the evolution process from polyhedral to nanoframes. Reproduced with permission from Ref. [280] © American Association for the Advancement of Science 2015.

For example, the electronic density of states of the catalyst can regulate the adsorption capacity of the reactants and the stability of the reaction transition state [199, 289, 290]. The electronic structure and energy band structure determine the distribution and energy level arrangement of electrons in the catalyst, which affects the electron transfer and reaction activity between the catalyst and the reactants [291, 292]. A catalyst with a suitable energy band structure can provide the right energy levels, allowing the electrons to adsorb from the reactants, transfer and participate in the reaction more easily. For ORR, catalysts with appropriate energy band structures can provide suitable intermediate energy levels to facilitate the adsorption and reduction reactions of oxygen molecules. Li and co-workers have synthesized a new ordered PtSnZn intermetallic clusters loaded with Al₂O₃ using a stepwise method of electrostatic adsorption and programmed warming reduction [293]. The Pt atoms in the PtSnZn cluster are well isolated from the Pt-Sn and Pt-Zn pairs by Sn and Zn. The PtSnZn/Al₂O₃ catalyst exhibited excellent catalytic performance for propane dehydrogenation with propylene selectivity of ~ 100% and maintained a high propane conversion (> 40%) in stability testing. Experimental and theoretical calculations show that Sn 5p and Zn 4s orbitals form Pt-Sn and Pt-Zn pairs by hybridization with Pt 5d, leading to the shift of the Pt d-band center away from the Fermi energy level. The shift of the Pt d-band center significantly reduces the adsorption energy of propylene and prevents further dehydrogenation of propylene, resulting in a high selectivity and stability of propylene.

The electronic structure and energy band structure can also affect the stability of the catalyst [243, 294–296]. In some electrocatalytic reactions, catalysts may face problems such as electrochemical corrosion, surface reforming and intermediate accumulation. Proper electronic and energy band structures can

improve the stability of catalysts, reduce the occurrence of undesirable reactions (e.g. oxidation, hydrogen precipitation, etc.) and prolong the lifetime for catalyst. The electronic structure and energy band structure also have an impact on the electron transport properties of the catalyst. In electrocatalytic reactions, electron transport within the catalyst is critical. A proper energy band structure can provide the relatively low electron transport impedance and promote fast electron transport, thus improving the conductivity and reaction rate of the catalyst. Moreover, the electronic and energy band structures can also modulate the selectivity of the catalyst [297–300]. Different energy band structures may lead to different reaction paths and intermediate products, which affect the selectivity of the reaction. By adjusting the energy band structure, the selectivity of the catalyst in multiple competing reaction paths can be controlled to achieve selective catalysis of specific products.

In general, electronic and energy band structures have important effects on electrocatalytic performance. A suitable energy band structure can provide suitable energy levels and electron transport paths to facilitate catalytic reactions. Meanwhile, the electronic and energy band structures can also modulate the stability and selectivity of catalysts. Therefore, when designing and optimizing electrocatalysts, the properties of their electronic and energy band structures need to be considered and regulated comprehensively.

4 DFT guided catalysts design

The traditional chemical synthesis route design generally adopts the strategy called “retrosynthetic analysis”, which breaks the complex target molecule up to be synthesized into several small molecular precursors, and then splits the precursors again,

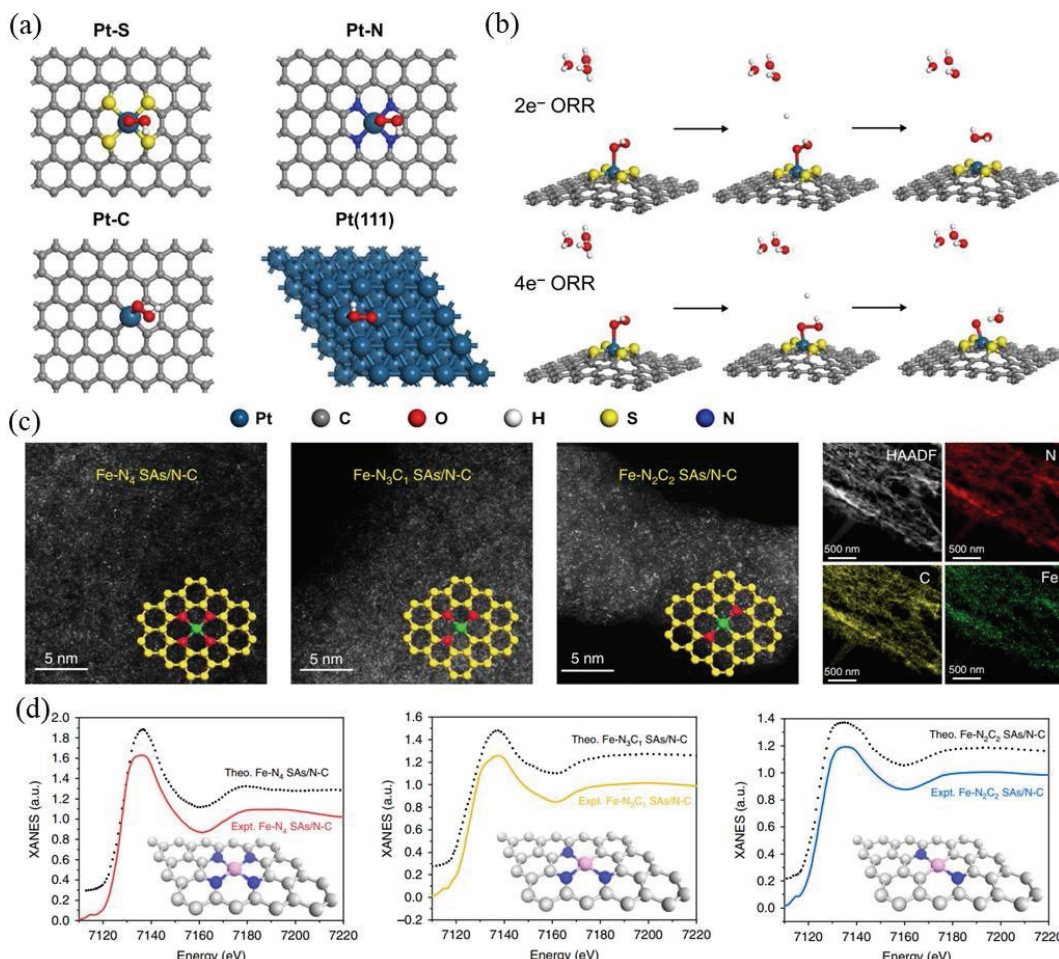


Figure 17 (a) DFT calculations of the ORR selectivity on different Pt-X-C moieties. (b) Illustration of oxygenated intermediates adsorption taking Pt-S₄ as an example, and relevant free energy diagrams for 2e⁻ (red) or 4e⁻ (black) ORR pathway. Reproduced with permission from Ref. [287] © Jiang, K. et al., under exclusive license to Springer Nature Limited 2022. (c) The AC-HAADF-STEM images and the HAADF-STEM-EDS mapping of the Fe-N₄C₁ SAs/N-C. The insets are the corresponding structure model. (d) Comparison between the experimental K-edge XANES spectra and the theoretical spectra of Fe-N₄ SAs/N-C, Fe-N₃C₁ SAs/N-C, Fe-N₂C₂ SAs/N-C, respectively. Reproduced with permission from Ref. [288] © Chen, C. et al., under exclusive license to Springer Nature Limited 2019.

continuously until it reaches the existing compounds in the laboratory [301–303]. With the rapid development of quantum chemistry theory, molecular simulation theory and high-performance computing technology, theoretical calculation has become an indispensable part of contemporary chemical science and an important auxiliary means for experimental research in catalytic science. In the field of chemical engineering, the evaluation of compound properties has entered the flux screening stage, but the chemical synthesis step is still in the manual operation stage. Researchers need to invest a lot of time and effort to analyze the correct chemical synthesis path, but the low yield of artificial synthesis and high trial and error costs result in insufficient commercial application value of synthetic chemistry technology in the fields of drugs and materials. Therefore, it is particularly important to introduce DFT to guide chemical synthesis. Using artificial intelligence retrosynthetic analysis, machine learning, neural network and other technologies to predict the synthesis path, filter the flux, and quickly find the most potential synthesis path is potential pathway. Recently, Waller et al. developed a new calculation and prediction system by using computers to assist retrosynthetic analysis [301]. The system uses Monte Carlo tree to search, and symbolic artificial intelligence is introduced to find the route of retrosynthetic analysis. In addition, two kinds of deep neural networks are introduced in the Monte Carlo tree step to improve the calculation accuracy and efficiency: The expanded decision network is used to find the path, and the filter network is used to preliminarily screen the possible reverse

synthesis path. In this chapter, we will describe the design concept for advanced catalysts from the theory, synthesis, structure, and catalytic performance. We hope that this will provide theoretical guidance for discovering theoretically driven efficient catalysts in specific catalytic reactions, thereby stimulating new ideas.

4.1 Catalysts for water splitting

Hydrogen is considered a clean and renewable energy source that can replace traditional fossil fuels [304, 305]. The large-scale use of hydrogen energy can effectively reduce carbon emissions and have a revolutionary impact on energy utilization. Electrochemical water splitting is widely regarded as a promising method for producing green hydrogen through renewable energy sources [306–310]. The water splitting mainly includes two half reactions: hydrogen evolution reaction and oxygen evolution reaction. Each half reaction follows a different reaction path, which depends on the electrochemical and electronic properties of the electrode surface. The activity, reaction kinetics, and stability vary with the inherent properties of the electrode surface and actual electrochemical conditions. Under standard conditions (25 °C and 1 atm), the theoretical thermodynamic potential of water decomposition is 1.23 V regardless of the electrolyte (acidic or alkaline). In fact, a much higher voltage than the theoretical value (this difference is called overpotential) is required to drive the rapid dissociation of water in the experiment.

Among them, platinum group metals (PGM) are the benchmark catalysts for OER (such as Ru, Ir) and HER (such as

Pt) [304, 311–314]. The scarcity and high prices limit its widespread application. Therefore, developing earth-abundant and efficient catalysts is an important means to solve current technological bottlenecks. During the hydrogen production process, the slow anodic OER reaction kinetics with proton coupling process involving multi-electron participation limits energy conversion efficiency and also affects the stability of proton exchange membrane (PEM) water electrolysis cells [315, 316]. The guidance of DFT provides a solid theoretical foundation for the rational design of excellent catalysts for water splitting [317–320]. The widely used Ir based catalysts currently have insufficient activity, while Ru based catalysts with high activity are prone to dissolution under OER conditions. This is related to the involvement of lattice-oxygen-mediated mechanism (LOM), which may lead to the collapse of crystal structure and also accelerate the leaching of Ru active species, causing to poor stability [311]. Recently, Peng et al. developed a dual-modulation method to curb the LOM and modulate the local electronic structures by incorporation of alkali-earth metal Sr and Ir [317]. Specifically, the ratio of two regulators (Sr and Ir) in ruthenium based catalysts was optimized via using Sr or Ir atom to randomly replacing the Ru atoms through high-throughput DFT calculation (Fig. 18(a)), and Sr-Ru-Ir ternary oxide with high activity and stability was obtained. Then, the calculated lowest overpotential of catalysts with given Sr-Ru-Ir ratios for OER was obtained (Fig. 18(b)). Moreover, the Pourbaix diagram demonstrated that the $\text{Sr}_2\text{Ru}_5\text{Ir}_1\text{O}_{16}$ phase was most active and stable for OER compared to controls (Fig. 18(c)). Then the Sr-Ru-Ir ternary catalysts including the binary and unary controls were synthesized by the sol-gel method. Furthermore, the Ru K-edge and Ir L₃-edge Fourier-transformed extended XAFS (FT-EXAFS) results (Figs. 18(d) and 18(e)) disclosed that the Ru-O bond distance in SrRuIr was slightly elongated compared to reference RuO_2 , while the bond length of Ir-O was shortened compared to bulk IrO_2 , indicating the strong interaction of Ru, O, and Ir atoms in local Ru-O-Ir structures. The electrochemical OER results showed that the SrRuIr oxide catalyst with the best performance achieved a low overpotential of 190 mV at 10 mA·cm⁻² and remained at low 223 mV after 1500 h test. In addition, the XPS and ¹⁸O isotope labeled mass spectrometry studies indicated that the excellent stability of SrRuIr oxide catalysts was attributed to the interactions in the local Ru-O-Ir structure, which inhibited the feasibility of LOM for OER. This high activity was attributed to the optimization of oxygen intermediate binding energy at the high valence Ru site formed after Sr and Ir doping. When the SrRuIr oxide catalyst was applied to the PEM electrolysis (Figs. 18(f) and 18(g)), the results showed that it could obtain a low full cell voltage of 1.50 V at 1 A·cm⁻². This work will provide in-depth understanding for the development of highly active and stable OER electrocatalysts and other electrocatalytic applications.

Similarly, Ge et al. proposed an intuitive descriptor (i.e. Ru charge) to depict the performance and long-term stability of the catalyst [318]. Research has found that although the instability of the catalyst was complex, it was closely related to Ru charge and the difficulty level of Ru-O bond breaking, i.e., the balance of formation energy between oxygen vacancy (ΔG_{VO}) and the Ru vacancy (ΔG_{VRu}). By controlling the M-O-Ru structure to alter the chelating elements around the RuO_6 motif, the catalyst followed the AEM mechanism and avoided the involvement of lattice oxygen under the LOM mechanism (Fig. 18(h)). Then, by studying the relationship between theoretical overpotential, ΔG_{VRu} and Ru charge, it can be found that $\text{Sn}_{0.5}\text{Ru}_{0.5}\text{O}_2$ was the optimum catalyst that followed the AEM mechanism (Figs. 18(i) and 18(j)). Based on the above analysis, researchers screened out SnRuO_x catalysts with appropriate Ru-O bonding strength in local

Sn-O-Ru structure followed the AEM and contributed to excellent activity and stability. As expected, the SnRuO_x only required a low overpotential (η) of 194 mV to drive a current density of 10 mA·cm⁻² (Fig. 18(k)), which was significantly reduced 176 mV than that of commercial RuO_2 . In addition, the overpotential only increased by 26.8 mV during the 250 h test under a current density of 100 mA·cm⁻² (Fig. 18(l)), which was clearly better than the advanced Ir-based catalysts. Overall, this work proposes a feasible concept and establishes a stable and efficient Ru based catalyst, laying the foundation for the application of Ru based materials in proton exchange membrane water electrolyzer (PEMWE).

In addition, Li's group proposed the idea of using cation doping to construct bi-metallic sites to regulate the coordination environment and electronic structure of the catalyst [314]. They first studied the local charge distribution, conductivity, and electronic structure of Co and O of LiCoO_2 doped with single Ru atom through theoretical calculation, and further verified the electronic structure change through magnetic testing. Electrochemical tests have indicated that Ru-Co/exfoliation LiCoO_2 (ELCO) exhibited excellent OER activity, with lower overpotential, higher mass activity, cycling stability, and faster kinetic processes. The author further studied its OER reaction mechanism through theoretical calculation. Through the analysis of its surface local charge distribution and electronic structure, it was confirmed that the interaction between Ru and Co was conducive to the surface charge transfer and the regulation of the electronic structure of the active site, thus optimizing the binding energy with the adsorption of intermediate products, reducing the reaction energy barrier of the rate-determining step (RDS), and accelerating the reaction process. Moreover, the zinc air battery assembled from it also presented superior rate performance and cycle life. This work provides a new perspective for the rational design of high-performance and long-lived catalysts using cationic coordination engineering. Recently, Liberto's group used density functional theory to study the OER process of single atom catalyst with transition metal atoms (Sc, V, Ti, Cr, Mn, Fe, Co, Ni, Cu, Pd and Pt) doped with graphene [321]. It was proposed that the possible formation of superoxide or peroxide complexes should be considered in research. Research has shown that most transition metals can form stable superoxo- and peroxy-intermediates when reacting with molecular oxygen. In addition, these superoxide or peroxide complexes affected the predicted activity in an undeniable manner and may result in several orders of magnitude changes in activity. This work revealed the important role of oxygen complex species in OER and strengthened the concept of SACs as coordination compound analogues, providing a solid theoretical basis for the rational design of efficient catalysts.

HER can be considered as the simplest electrochemical reaction and the foundation for studying more complex multi electron proton transfer reactions. Although it is very simple, it is still a multi-step chemical reaction that includes three processes: adsorption, reduction, and desorption on the electrode surface [322]. So far, the benchmark HER electrocatalyst is still dominated by Pt based materials but its high cost and scarcity hinder its large-scale application. Therefore, it is urgent to design cost-effective and efficient HER electrocatalysts reasonably. In addition to traditional Pt based catalysts, Ru is considered a promising alternative catalyst due to its corrosion resistance and excellent HER performance in alkaline media, which can alleviate the rare and expensive situation of Pt. The electrolysis of water can be achieved in acidic, neutral, and alkaline environments, where the reduction rate of water in neutral/alkaline media is slow because the dissociation reaction of water is slower. Therefore, even the most advanced HER catalyst Pt has a lower activity in



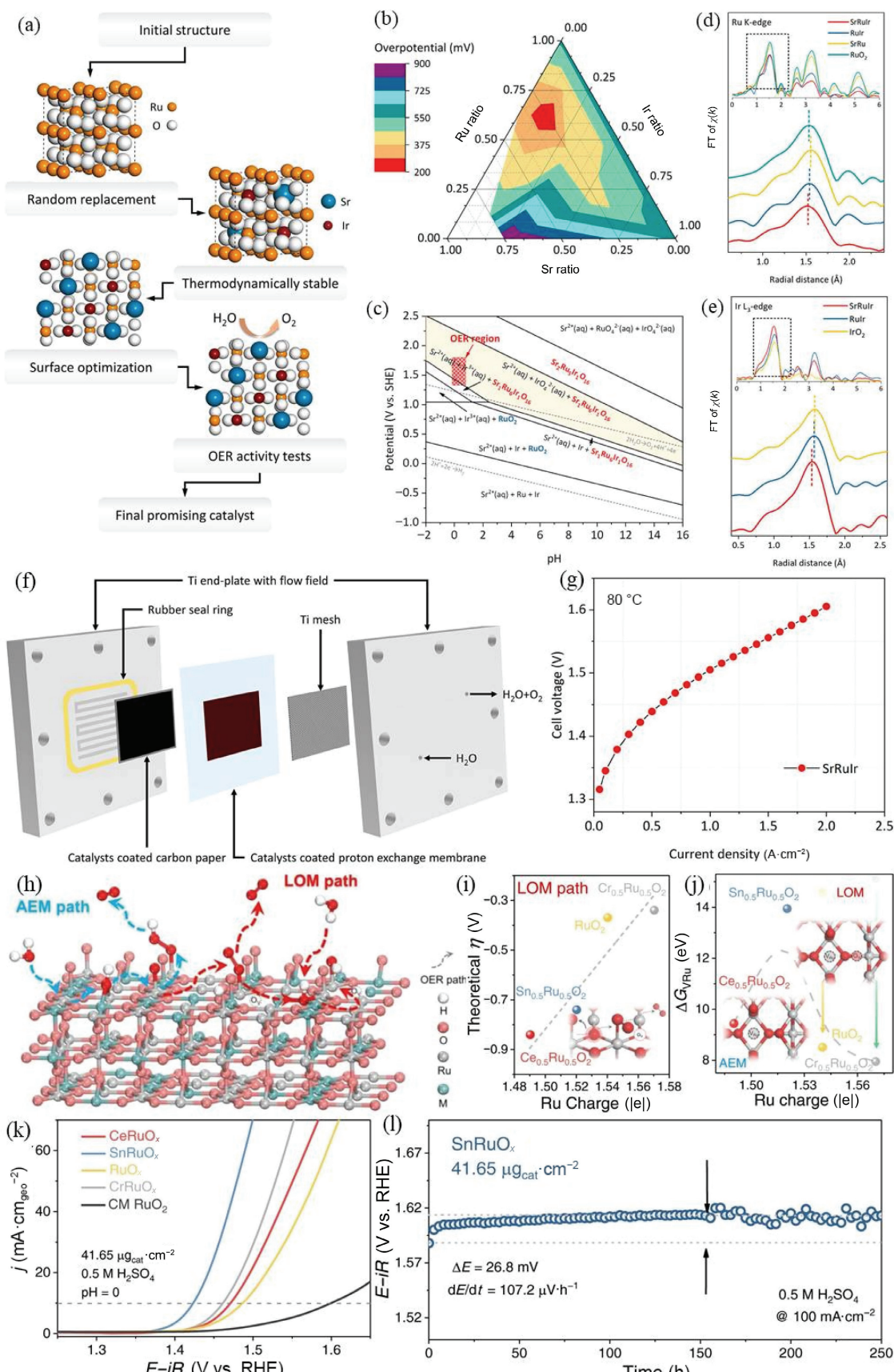


Figure 18 (a) DFT flow diagram of high-throughput screening of electrocatalysts for OER. (b) Calculated overpotential of OER with different ternary compositions. (c) Pourbaix diagram of Sr₂Ru₅Ir₁O₁₆ and Sr₁Ru₆Ir₁O₁₆ oxide calculated using DFT: the Sr₁Ru₆Ir₁O₁₆ phase is stable in the OER region. (d) and (e) Ru K-edge FT-EXAFS spectra (k weight = 3) and Ir L₃-edge FT-EXAFS spectra (k weight = 2) of different samples, respectively. (f) Schematic diagram of the PEM electrolyzer. (g) Steady-state polarization curve of a PEM electrolyzer measured at 80 °C using SrRuIr as anodic catalysts. Reproduced with permission from Ref. [317], © American Chemical Society 2021. (h) Schematics of two pathways for OER (AEM and LOM) on the surface of M_{0.5}Ru_{0.5}O₂ (110). (i) Theoretical overpotential plot under LOM pathway as a function of the Ru charge. (j) The Ru vacancy formation energy (ΔG_{VRu}) of M_{0.5}Ru_{0.5}O₂ is characterized by Ru charge. (k) Geometric area normalized LSV curves of MRuO_x. (l) Chronopotentiometry curve of SnRuO_x nanocatalyst operated at 100 mA·cm⁻² during the 250 h. Reproduced with permission from Ref. [318], © Shi, Z. et al. 2023.

neutral/alkaline media by 2 to 3 orders of magnitude than in acidic media. Although HER exhibits better activity under acidic conditions, corrosion of equipment and catalysts hinders its long working life. Neutral media provide more favorable conditions for the catalyst to maintain the stability of the electrolytic cell and provide a less corrosive environment. The previous reports demonstrated that the HER in neutral/alkaline condition experienced the water dissociation ($M + e^- + H_2O \rightarrow M-H_{ad} + OH^-$, where M represents the active site and H_{ad} refers to the adsorbed H), followed by the Heyrovsky reaction ($H_2O + e^- + M-H_{ad} \rightarrow M + OH^- + H_2$) or the Tafel process ($H_{ad} + H_{ad} \rightarrow H_2$) [254, 289, 323–326]. Compared to acidic HER, the water molecules required additional splitting to provide protons, resulting in slower kinetics in neutral/alkaline media. This caused to a lower hydrogen coverage ($M-H_{ad}$) on the catalyst surface during the HER process. For neutral and alkaline HER, H_2O is the main source of protons. With the increase of pH value, the flexibility of the hydrogen bonded water layer at the interface decreases, which prevents the intermediate from penetrating the

interface water layer and diffusing into the solution, thus inhibiting the regeneration of the surface active site; In alkaline media, non-specific adsorption of OH^- can promote the passage of intermediates through interfacial water layers, but in neutral media, OH^- is almost barely exist, making it difficult for intermediates to diffuse into the overall solution.

In order to verify the critical role of interface water in neutral HER, Chen et al. operated DFT calculations to evaluate the rationality of using RuNC as an interfacial water research platform [319]. Then, the *ab initio* molecular dynamics (AIMD) calculations was conducted to estimate the feasibility of tuning the interfacial water with additive $RuSe_x$. DFT theoretical research has found that in neutral media, interfacial water molecules are interconnected through more hydrogen bonds than in acidic and alkaline media, thereby inhibiting the migration of H_2O^*/OH^* at the electrode/electrolyte interface; Additional $RuSe_x$ can accelerate the transport of H_2O^*/OH^* through the disordered hydrogen bonding network in the interface region, thereby increasing the number of highly active H_2O^* at RuNC surface and enhancing the

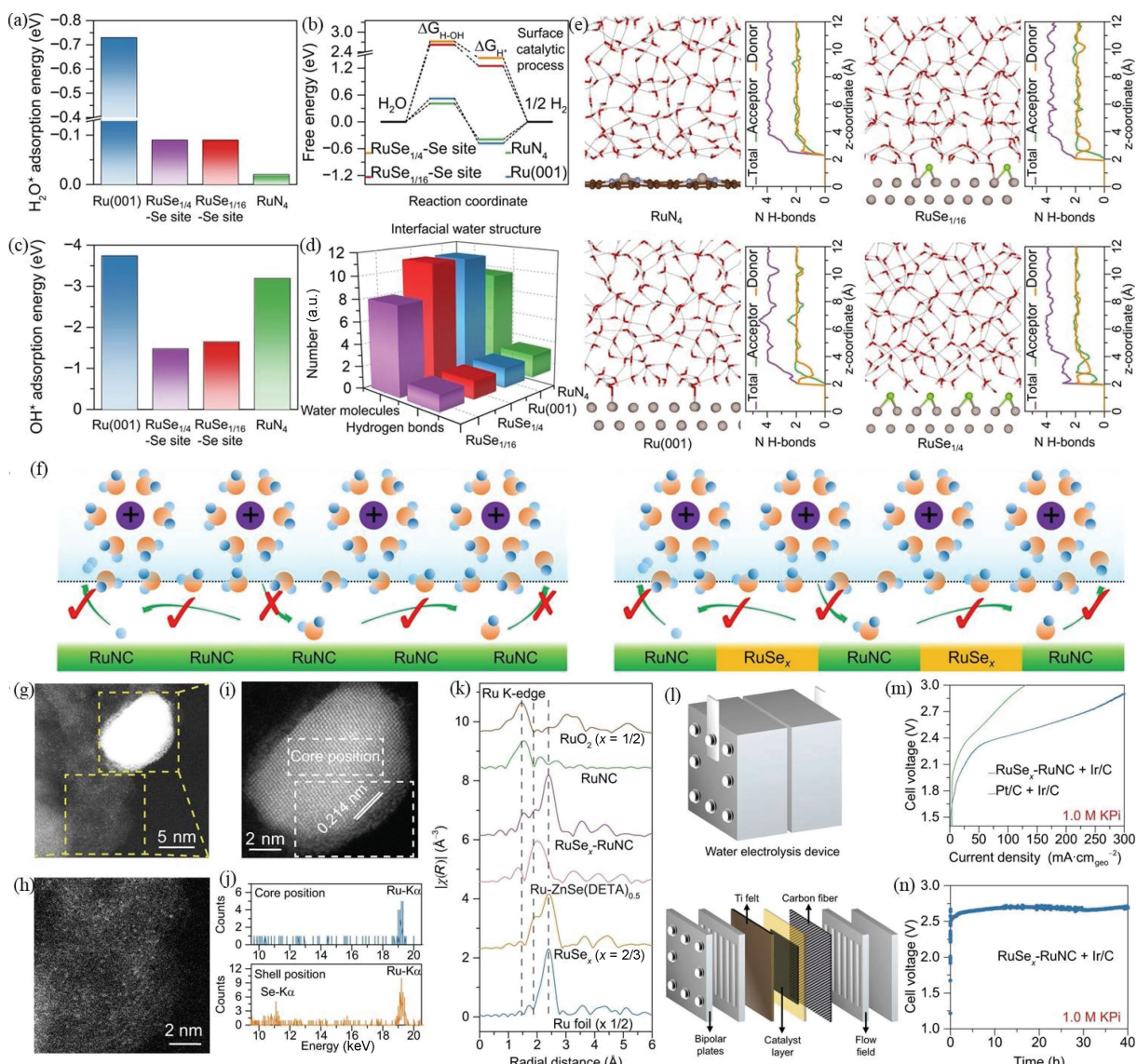


Figure 19 (a) The H_2O^* adsorption energies of different structural models. (b) The free energy changes of water dissociation and the Gibbs free energies of hydrogen adsorption at various models. (c) The OH^* adsorption energies of different structural models. (d) The average number of hydrogen bonds per interfacial water molecule and the corresponding average distribution of hydrogen bond number along the surface. (e) The representative snapshots of the structure of interfacial water molecules and the corresponding average distribution of hydrogen bond number along the surface. (f) Proposed reaction mechanisms of RuNC (left) and $RuSe_x$ -RuNC (right) under neutral HER. (g)–(i) The sub- \AA resolution HAADF-STEM images of $RuSe_x$ and RuNC. (j) The EDX analysis. (k) The FT spectra of Ru K-edge EXANES. (l) Schematic illustration of a typical anion-exchange-membrane water electrolysis device. (m) Electrocatalytic water splitting activity of the $RuSe_x$ -RuNC + commercial Ir/C, and the benchmark commercial Pt/C + commercial Ir/C. (n) Stability tests. Reproduced with permission from Ref. [319], © Sun, K. et al. 2022.

activity of neutral HER (Figs. 19(a)–19(e)). Therefore, the synergistic effect of Ru single atoms and RuSe_x clusters can effectively decouple the interfacial water and surface HER catalytic processes, thereby contributing to better catalytic activity (Fig. 19(f)). Guided by DFT theory, a series of RuSe_x-RuNC composite catalysts were prepared by pyrolysis strategy. Furthermore, the AC-HAADF-STEM and the k^2 -weighted FT-EXAFS spectra (Figs. 19(g)–19(k)) confirmed that the coexistence of RuSe_x and RuNC. The electrochemical results showed that the neutral water electrolysis device assembled by RuSe_x-RuNC can reach a current density of 10 mA·cm⁻² with only needing 1.86 V cell voltage (Figs. 19(l) and 19(m)), and can operate continuously for 40 h at a high current density of 100 mA·cm⁻² without significant performance degradation (Fig. 19(n)), which was far superior to benchmark commercial Pt/C + Ir/C based membrane electrode assembly (MEA). Overall, this work elucidates how to collaborate with single atom and cluster compounds to promote interfacial electrocatalysis at the molecular level, laying the foundation for the design and preparation of efficient electrochemical water splitting catalysts in a neutral environment.

4.2 Catalysts for fuel cell

Fuel cell is a power generation device that primarily converts chemical energy in fuel into electrical energy through oxidation-reduction reactions using oxygen or other oxidants. Fuel cells have gradually gained public attention due to their advantages such as high power density, high energy density, high energy conversion efficiency, and clean and green products [295, 296, 330–332]. However, the slow kinetics of cathodic ORR and other issues seriously hinder the practical application of these devices. In aqueous solutions, ORR usually follows two types reaction processes (Fig. 20(a)) [5, 148, 327, 333–336]: 1) O₂ + 4(H⁺ + e⁻) → 2H₂O, $U = 1.23$ V vs. RHE; 2) O₂ + 2(H⁺ + e⁻) → H₂O₂, $U = 0.70$ V vs. RHE. Although Pt based catalysts have high ORR catalytic activity, their problems in scarcity and stability limit their large-scale application. On the other hand, transition metal nitrogen carbon (M-N-C) nanomaterials have been proven to be effective substitutes for precious metal catalysts. In this situation, it is of great significance to rational design M-N-C based ORR catalysts with high cost-effectiveness, high activity, and high stability. Recently, Zhao et al. utilized DFT to investigate the mechanism of the 2e⁻ or 4e⁻ reaction pathway of ORR over carbon supported single atom Co catalysts [328]. Furthermore, they proposed that the edge effect of the support can affect the electronic structure of the Co-N₄ site and its adsorption on intermediates, thereby regulating its selectivity to the ORR path. At the same time, it was revealed that the position of single atomic sites in the supports and the types and distribution of surrounding functional groups have a significant impact on the reaction activity and selectivity of the catalyst. In carbon carriers, isolated Co atoms have various position distributions, such as edges or bases. Different catalytic sites exhibit different catalytic activity and selectivity due to their different coordination environments. The author first found through theoretical calculations that the Co-N₄ site located at the edge of the carbon carrier has optimized adsorption energy and higher catalytic activity for OOH* intermediates in 2e⁻ ORR process, while the Co-N₄ site located on the base surface was more inclined towards the 4e⁻ ORR pathway (Figs. 20(b)–20(d)). Subsequently, researchers successfully constructed two types of Co SACs with different edge-to-bulk ratios using porous carbon (HPC) and graphite sheets (GFs) as supports. The Co K-edge XANES and FT-EXAFS spectra confirmed that the central Co atom was coordinated with four N atoms to form the coordination structure of Co-N₄ in Co-N/HPC and Co-N/GFs (Figs. 20(e) and 20(f)). Electrochemical testing showed that Co-

N/HPC rich in edge Co-N₄ coordination structures exhibited excellent 2e⁻ ORR activity with exceeding 95% selectivity and achieved a maximum value of 98% at 0.52 V vs. RHE (Fig. 20(g)). However, Co-N/GFs suggested a nearly 4e⁻ ORR pathway. Through further spectroscopic analysis, performance testing, and DFT theoretical calculations, it was found that during the 2e⁻ ORR process, the carbon support was corroded by the generated H₂O₂, forming a series of oxygen-containing functional groups on the surface and edges. These oxygen-containing functional groups can further optimize the adsorption of OOH* intermediates at the Co-N₄ site, enhancing reaction activity while maintaining selectivity of over 90%. This result also provided a reasonable explanation for the differences in ORR selectivity of previously reported Co SACs, offering ideas for promoting H₂O₂ generation through the 2e⁻ ORR pathway.

At present, non-precious metal catalysts with high activity and stability have made significant progress. However, after 30,000 cycles, the activity of noble-metal-free catalysts significantly decreased, mainly due to carbon corrosion and metal leaching of the active center. Researchers generally combined Pt with other metals (Cu, Fe, Co, Ni, Y, etc.) to form alloy nanoparticles or core-shell structured nanoparticles, and optimized their ORR performance by improving and regulating the adsorption of OH intermediate for Pt and the strain for catalyst. However, common Pt-M binary catalysts still suffered from deactivation due to structural damage during long-term electrocatalytic cycles. The introduction of a third metal can further regulate the ORR activity and stability of the catalyst under acidic conditions. In addition, the previous reports indicated that the proportion and distribution of various components in Pt ternary catalysts are crucial for the activity and stability of the catalyst. However, systematic research on the impact of the proportion and distribution of each component on ORR performance through experiments and theoretical calculations still faced enormous challenges because of the complexity of its system. Based on the neural network potential (NNP) algorithm, Han et al. combined first principles DFT with machine learning technology to systematically calculate, simulate, and screen the composition, element distribution, and ORR performance of ternary PtFeCu nanoparticles. Subsequently, they successfully synthesized PtFeCu nanoparticles with different compositions through a simple and rapid ultrasonic method [47]. This catalyst exhibited excellent ORR activity and stability in acidic media, greatly overcoming the problem of insufficient activity and stability of non-precious metal catalysts. In conclusion, this work deeply studied the regulation of Pt strain energy on the surface of ternary catalyst PtFeCu and the inhibition of segregation on the surface of Fe by introducing Cu, so as to optimize the catalytic activity and stability of PtFeCu for ORR. The use of machine learning technology provided convenience for selecting the optimal proportion and distribution of metal components.

In addition to ORR, hydrogen oxidation reaction (HOR) is also a key reaction in clean/sustainable energy converter components such as cation exchange membrane fuel cells (AEMFCs). Therefore, the design of high catalytic activity anode catalysts suitable for such fuel cells has received widespread attention. Previous studies have indicated that the nanocrystals (NCs) supported atomically dispersed metal can tune the electronic structure of the supports of NCs, causing to the changes of activation barriers for reactants and the binding strength of intermediates, thus optimizing the catalytic performance [337, 338]. In view of this, Wang et al. reported on a new type of RuNi1 catalyst for HOR, in which Ni atoms were dispersed on Ru nanocrystals [329]. The prepared RuNi1 catalyst exhibited excellent catalytic activity and stability for HOR in alkaline media, superior to Ru-Ni bimetallic nanocrystals, bare Ru nanocrystals,

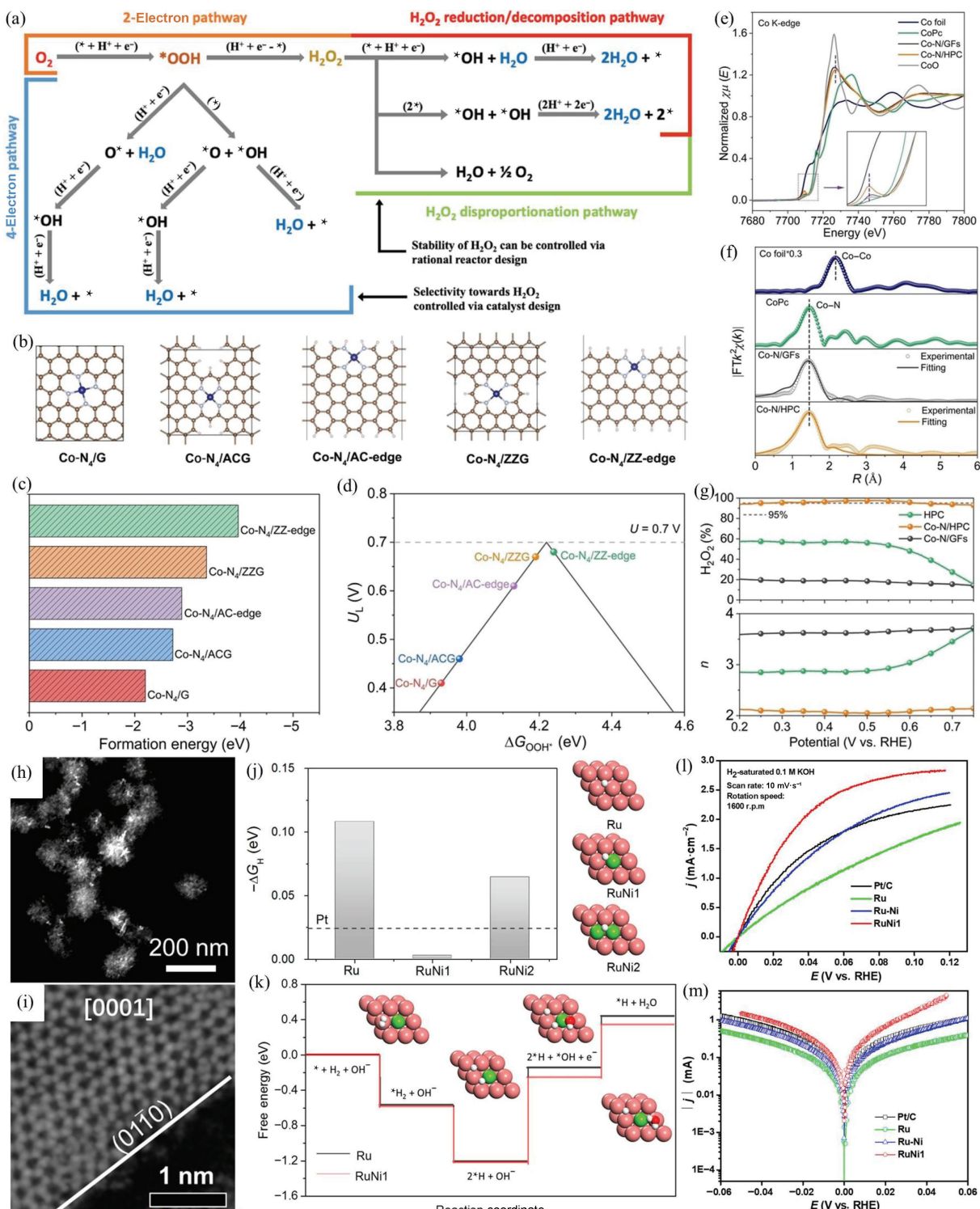


Figure 20 (a) Unified two- and four-electron pathways in electrochemical ORR. Reproduced with permission from Ref. [327], © Wiley-VCH GmbH 2020. (b) The optimized structural models of $\text{Co-N}_4/\text{G}$, $\text{Co-N}_4/\text{ACG}$, $\text{Co-N}_4/\text{AC-edge}$, $\text{Co-N}_4/\text{ZZG}$, and $\text{Co-N}_4/\text{ZZ-edge}$. Color code: the brown, grey, blue, and pink balls refer to C, N, Co, and H atoms, respectively. (c) Calculated formation energies of different structure models. (d) The calculated volcano plot of $2\text{e}^-\text{-ORR}$. The U_L is plotted as a function of ΔG_{OOH^-} . (e) Co K-edge XANES spectra of various samples (inset: the enlarged image of selected area). (f) k^2 -weighted FT-EXAFS curves of Co-N/HPC and reference samples. (g) Calculated $2\text{e}^-\text{-ORR}$ selectivity and electron transfer number (n) as a function of applied potentials. Reproduced with permission from Ref. [328], © Wiley-VCH GmbH 2022. (h) and (i) HAADF-STEM image of RuNi1. (j) Calculated hydrogen adsorption energies on pure Ru, single-atomic Ni and bi-atomic Ni dispersed on Ru catalysts (left). The schematic diagrams of Ru, RuNi1, and RuNi2 structural models (right). (k) Free energy diagrams of HOR on Ru and RuNi1. Color: orange, Ru; green, Ni; red, O; white, H. (l) HOR polarization curves of RuNi1 and reference Pt/C, Ru and Ru-Ni. (m) Tafel slopes of Pt/C, Ru, Ru-Ni and RuNi1 for HOR/HER. Reproduced with permission from Ref. [329], © American Chemical Society 2020.

and commercial Pt/C catalysts. Researchers successfully synthesized the RuNi1 NCs catalysts using a typical wet chemical strategy. During the growth process of RuNi1 NCs, ultra-thin branched nanostructures were first formed, and then rapidly evolved into ultra-thin nanosheets with serrated edge surfaces. The AC-HAADF-STEM image further revealed the dispersion of

single Ni atom and Ru at the atomic level (Figs. 20(h) and 20(i)). DFT simulations showed that the separation of Ni atoms on Ru nanocrystals not only optimized the binding energy of hydrogen (Figs. 20(j) and 20(k)), but also reduced the free energy of water formation, contributing to excellent electrocatalytic HOR activity of RuNi1 catalyst. As expected, the anodic current density of

RuNi1 NCs was obvious higher than those of reference catalysts under a potential range of 0.0–0.12 V vs. REH, suggesting the excellent HOR performance in comparison to Ru–Ni, Ru NCs, and Pt/C catalysts (Fig. 20(l)). In addition, under an overpotential of 50 mV, the J_k for RuNi1 was 4.679 mA·cm_{disk}⁻² (Fig. 20(m)), which was approximately 5.5 times that of commercial Pt/C (0.853 mA·cm_{disk}⁻²).

Moreover, Sahoo et al. reported that using *ab initio* theory calculation methods to study the mechanism of Pd-CeO₂ catalyst for HOR [341]. The DFT theory based on exchange correlation functional, generalized gradient approximation and Hubbard correction was used to describe the electronic structure and related functional properties of the catalyst. The author simulated and calculated the conditions of different Pd concentrations on the surface of CeO₂, and calculated the Tafel slope in the dissociation of hydrogen molecules and the Volmer reaction to generate H₂O molecules. It was revealed that the HOR catalytic activity of Pd-CeO₂ catalyst was significantly improved compared to Pd or CeO₂ species alone, and further the 10 at.% Pd modified CeO₂ expressed the best catalytic activity. This was attributed to the synergistic effect of many factors, including hydrogen, OH, H₂O binding energy, and the optimization of charge transfer between catalyst/substrate/adsorbent. This study utilized *ab initio* theoretical analysis to understand the catalytic mechanism of HOR from electronic, atomic, and molecular perspectives, providing experience and guidance for the development of high-efficiency catalysts and reducing the amount of noble metals.

4.3 Catalysts for NRR

Ammonia (NH₃) is crucial for humans and ecosystems as a raw material for fertilizers and a clean energy carrier [342–344]. However, the extremely high bond energy of the N≡N resulted in only about 15% conversion efficiency from N₂-to-NH₃ in the traditional Haber-Bosch process [339, 345–347]. Compared with the high-energy consuming Haber Bosch process (400 °C, 40 MPa), the electrochemical NRR provided a sustainable and environmentally friendly solution for ambient ammonia synthesis, which can be directly produced from N₂ in the atmosphere as a green fuel [348, 349]. However, the biggest limitation of NRR is poor Faraday efficiency and lower NH₃ yield under ambient conditions, which seriously restricts its practical application. This bottleneck is mainly attributed to the poor selectivity and activity of the currently designed NRR electrocatalysts. Firstly, the poor selectivity of NRR is because of its competitive HER dominating the NRR process, which in fact affects almost all traditional electrocatalysts used for NRR. Secondly, the poor catalytic activity of NRR is attributed to the weak affinity of N₂ to the catalyst, which was due to the chemical inertness of N₂ and the lack of electronic defect sites on the catalyst to accept the lone pair electrons of N₂, which hindered the activation of N₂ and correspondingly reduced the efficiency of NRR. In order to overcome these limitations, it is necessary to suppress the traditional hydrogen adsorption process and improve the inherent catalytic activity of the catalyst for NRR.

DFT theoretical studies and previous reports have verified that electrochemical conversion of nitrogen to ammonia is feasible within a specific potential window under ambient conditions [349, 350]. According to reports, boron sites doped in the carbon skeleton induce electronic defects, which will significantly enhance electrocatalytic performance and therefore have essential guiding significance in NRR [351]. However, the amount of boron doping in the carbon skeleton is greatly limited, thereby reducing its reaction activity. Considering this, COF materials with rich active site provide an appropriate platform for designing multi-sites catalysts. In addition, the chemical environment of boron sites in

COF is flexible and adjustable, which has great potential to further improve its intrinsic activity. For example, Yan and co-workers reported that promoting N₂ to enter boron rich covalent organic frameworks through electrochemical excitation can achieve efficient NRR activity [339]. DFT and MD simulations demonstrated that under electrochemical conditions, boron sites are bonded with nitrogen-containing substances, promoting a stronger affinity of amorphous COFs for N₂, thereby enhancing intermolecular collisions (Figs. 21(a)–21(g)). Surprisingly, the electrochemically excited COF (Eex-COF)/NC achieved superior electrocatalytic nitrogen reduction performance (Figs. 21(h) and 21(i)): breaking the maximum value of 45.43% for Faradaic efficiency and NH₃ yield rate of 12.53 μg·h⁻¹·mg⁻¹ at -0.2 V vs. RHE, which was a record breaking performance among the metal-free catalysts to date. In contrast, the NC substrate presented a poor NRR performance so that its contribution to the synthesis of ammonia in Eex-COF/NC can be ignored. In addition, the HER process in Eex-COF/NC can be greatly suppressed in the voltage range from -0.1 to -0.3 V vs. RHE based on more electrons captured by NRR (Fig. 21(j)). Ling et al. used ZIF to electronically modify the d-band structure of PtAu electrocatalysts, significantly improving the selectivity and activity of the catalysts [340].

Specifically, researchers fabricated a model structure of coating the Pt/Au electrocatalyst with a layer of ZIF to induce direct chemical/electronic interactions, reduce the d-band position of the electrocatalyst, weaken H adsorption, and simultaneously construct electron deficient sites to promote the interaction between the catalyst and N₂ to efficiently drive the NRR kinetic process (Figs. 21(k)–21(m)). Impressively, the obtained 60 nm Pt/Au@ZIF exhibited excellent NRR activity under wide applied potentials window (-2.1 to -2.9 V) (Figs. 21(n) and 21(o)). Compared with those without ZIF modification, the 60 nm Pt/Au@ZIF electrocatalyst with ZIF modification achieved high FE of > 44% and 60-fold NH₃ yield rate improvement from (2.5 ± 1.1) to (161.9 ± 16.7) μg·mg_{cat}⁻¹·h⁻¹ under ambient conditions, among the ZIF can also serve as a hydrophobic layer to suppress HER. In summary, the theoretical guidance of the electrocatalytic design strategy proposed in this work is universal and can be extended to different metal electrocatalysts. In addition, Yu et al. found that the monolayer C₂N porous material served as a very good carrier for preparing single atom material via DFT calculations [354]. After careful screening, it was found that transition metals can form metal-N coordination compounds through the N atoms at the edge of the pores, thereby forming stable SAC and dual atom catalysts (DAC). Detailed DFT calculations confirmed that the IVB group atoms (Ti, Zr and Hf) can effectively catalyze N₂ to form ammonia for the SAC system. Furthermore, the Cr-Cr system tended to form NH₃ in the case of DACs, but the V-V system typically converted N₂ into N₂H₄. The calculation of electronic structure further revealed that the symmetry of *d* orbitals in SAC and DAC catalysts influenced their orbital overlap with N₂, thus affecting their catalytic activity and selectivity.

4.4 Catalysts for eCO₂RR

The massive emission of CO₂ leads to global warming [355], which in turn induces frequent occurrence of extreme weather phenomena such as typhoon, high temperature, rainstorm, debris flow, droughts and so on. The increase in CO₂ emissions is mainly caused by the extensive use of fossil fuels by humans, and high energy consumption means high CO₂ emissions. Taking measures to reduce CO₂ emissions has become a hot topic of common concern among scholars, experts, and national leaders from various countries. The CO₂ is the main greenhouse gas and a widely existing carbon resource. The researchers have proposed a

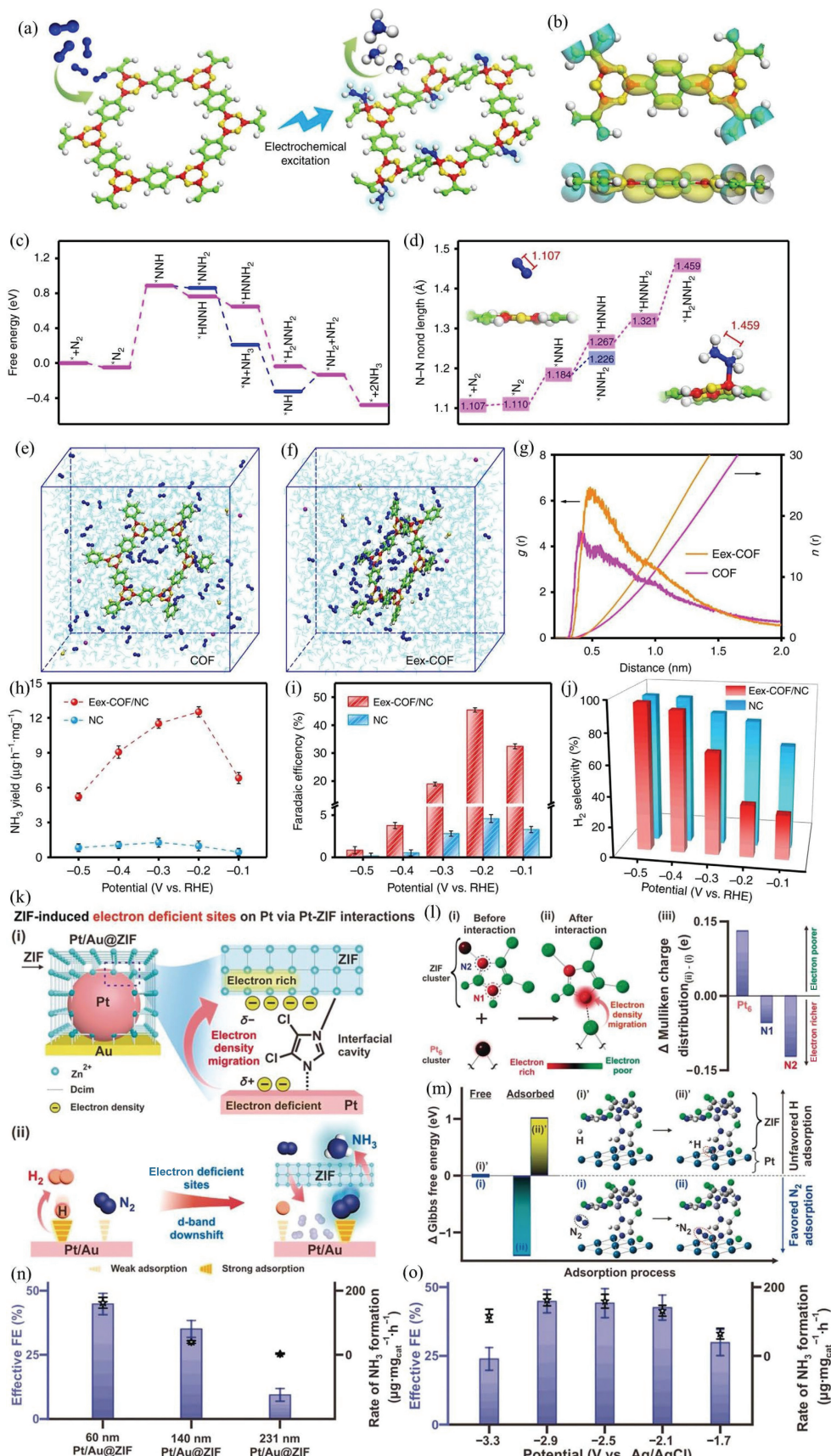


Figure 21 (a) Schematic illustration form COF to Eex-COF under the electrochemical excitation effect. (b) The calculated charge distribution. (c) The free energy diagrams and (d) changes of N-N bond length for ammonia synthesis. The molecular dynamics simulation snapshots of (e) COF and (f) Eex-COF. The red, green, blue, yellow, and gray spheres represent B, C, N, O, and H atoms, respectively. (g) Radial distribution function (RDF) and integrated RDF of nitrogen molecules around different models. (h) NH_3 yield rates, (i) corresponding Faradaic efficiencies, and (j) H_2 selectivity of Eex-COF/NC and NC. The error bars correspond to the standard deviations of measurements over three separately prepared samples under the same conditions. Reproduced with permission from Ref. [339], © Liu, S. et al. 2019. (k) The main functions of ZIF induced electron deficient sites on Pt via Pt-ZIF interactions. (l) Electron density distributions. (m) Gibbs free energy for i) free and ii) adsorbed states of N_2 and H on Pt/Au@ZIF. (n) The Faradaic efficiency and rate of ammonia formation by various Pt/Au@ZIF samples. (o) Evaluating NRR performance of 60 nm Pt/Au@ZIF at various potentials. Reproduced with permission from Ref. [340], © Wiley-VCH GmbH 2020.

variety of coupling strategies including thermal catalysis, electrocatalysis [356–360], photocatalysis [361], synthetic biology and a variety of coupling strategies to achieve the chemical conversion of CO₂. Electrochemical CO₂ reduction reaction (eCO₂RR) has received widespread attention due to its advantages of environmental friendliness, availability of clean energy, controllable reaction pathways, and strong technical compatibility. The use of electrochemical reduction technology can convert CO₂ into high value-added chemicals and fuels [168, 362, 363], which is also an important way to reduce carbon emissions and achieve carbon neutrality. Recently, SACs have shown clear and unique active centers in some fields such as electrocatalytic reactions, organic transformations, and environmental catalysis, and have achieved excellent activity and selectivity [329, 364–366]. Especially, Cu SAC shows good application prospects in electrocatalytic CO₂RR [5, 367, 368]. Recently, Wang et al. reported a Cu SAC using Lewis acid as a support for electrocatalytic conversion of CO₂ to methane (CH₄) [352]. Theoretical calculation results demonstrated that the Lewis acid sites in metal oxides (such as Al₂O₃, Cr₂O₃) can adjust the electronic structure of Cu single atoms (SAs) by optimizing the intermediate adsorption, thus promoting the methanation of CO₂ (Figs. 22(a)–22(d)). Guided by DFT theory, the Cu/p-Al₂O₃ SAC was successfully prepared. Furthermore, the high resolution TEM (HRTEM), EDS elemental mapping images, AC-HAADF-STEM and X-ray absorption spectroscopy (XAS) clearly displayed that isolated Cu atoms species appeared on p-Al₂O₃, indicating the presence of single atom copper (Figs. 22(e)–22(j)). The electrochemical test results demonstrated that at -1.2 V vs. RHE, the FE reached 62%, and the corresponding CH₄ generation current density was 153.0 mA·cm⁻² (Figs. 22(k) and 22(l)). This work developed an effective strategy to tune the electronic structure of Cu SACs, thereby achieving efficient electrocatalytic conversion of CO₂RR to CH₄.

Moreover, compared with SACs, diatomic catalysts have a more prominent synergistic catalysis effect in the electroreduction of carbon dioxide. Chen et al. reported the synthesis of Ni-Cu diatomic pair catalysts and investigated their catalytic performance for eCO₂RR [353]. Firstly, they compared the adsorption effects of COOH and CO intermediates on NiN₄ and NiMN₆ (M = Zn, Co, Cu, Cr, Mn, Ti and V) configurations using DFT calculations (Fig. 22(m)). The DFT calculation results showed that the free energy of all NiMN₆ configurations for adsorbing COOH and CO was lower than NiN₄, with NiMnN₆ and NiCuN₆ having lower reaction barriers, with values of 0.44 and 0.59 eV, respectively (Fig. 22(n)). The rate-determining steps were CO desorption and COOH adsorption. On the other hand, the difference between the HER barrier of NiCuN₆ and the barrier of eCO₂RR was greater than that of NiMnN₆, so the selectivity was better for NiCuN₆ (Fig. 22(o)). In the experiment, the author prepared Ni/Cu N-C diatomic catalyst using ZIF-8 structure precursor (Fig. 22(p)). The HRTEM and AC-HAADF-STEM revealed that neighboring bright dots can be obviously observed (Figs. 22(q) and 22(r)), suggesting the successful construction of Ni-Cu atomic pair catalysts. The EXAFS results showed a Ni-Cu bond length of 2.08 Å and confirmed the structure of NiCuN₆ (Figs. 22(s) and 22(t)). The XANES and XAFS results fully confirmed that the addition of Cu can stabilize the single atom structure and valence state of Ni without being reduced. The electrochemical test results showed that the reaction current of Ni/Cu-N-C was higher than those of Ni-N-C and Cu-N-C in the CO₂ saturated 0.5 M KHCO₃ electrolyte (Figs. 22(u)–22(w)). The CO Faraday efficiency reached a maximum of 97.7% (-0.7 V vs. RHE), and the Tafel slope was 175 mV·dec⁻¹. The electrochemical activity was stable within 60 h. In the flowing electrolytic cell, the reaction current density

exceeded 100 mA·cm⁻², and the CO Faraday efficiency surpassed 80%.

Apart from SACs and diatomic catalysts, the metals, metal/metal oxide composites catalysts have all been investigated as electro-catalysts for eCO₂RR. A large number of studies have shown that when CO₂ is activated, its geometric structure changes from a symmetric linear junction to a curved CO₂. As a key intermediate of eCO₂RR, it can combine with electrons on different types of electrodes to form different sorts of adsorption states. This will result in different reduction pathways and ultimately different products, such as formic acid, CO or C₂₊ hydrocarbons or oxygenates [369]. For example, when CO₂ molecule obtains e⁻ on electrodes such as gold (Au), silver (Ag), and zinc (Zn), it is coordinated and adsorbed on the surface of these electrodes, further reacting with e⁻ and H⁺ to form OC^{*}-OH intermediates, which then undergo the process of removing H₂O to generate CO products. When CO₂ is not easily adsorbed on electrodes such as tin (Sn), indium (In), mercury (Hg), cadmium (Cd), and lead (Pb), it reacts with adjacent H₂O or H⁺ to generate HCOO or HCOOH. In addition, products such as C₂₊ hydrocarbons or oxygenates are usually formed on the surface of copper electrodes.

Based on previous experiments and theoretical induction, the effect of theoretical guidance on discovering efficient catalysts in eCO₂RR can be summarized as follows: 1) DFT theoretical calculation can provide guidance for the determination of CO₂ conversion reaction path for the study of reaction intermediate, thermodynamic stability and kinetic energy barrier at the interface between electrode materials and electrolyte; 2) the effects of electrolyte solvation on the reaction performance were studied, and the microscopic effects of its electrostatic, hydrogen bond, and Van der Waals force on the electrode electrolyte interface were analyzed to provide guidance for the construction of the eCO₂RR to syngas system; 3) DFT calculation can explore the proton-electron transfer path in the process of eCO₂RR reaction, and then establish the mathematical model of equilibrium reaction and equilibrium interfacial mass transfer in multiphase medium during electron transfer. It further reveals the binding capacity of the catalyst to CO₂ and intermediates, which will directly affect the product selectivity of CO/HCOOH.

4.5 Catalysts for catalytic conversion of carbon/nitrogen containing compounds

The conversion and utilization of CO₂ is an important way to reduce CO₂ emissions. In recent years, researchers have conducted extensive research on the thermal conversion of CO₂ to methanol, olefins, and oil products, and have achieved a series of breakthrough achievements. Methane and carbon dioxide are two abundant substances in nature. By catalytic co-conversion to produce chemical raw materials, the dependence of the chemical industry on traditional fossil fuels can be reduced, which helps to alleviate the greenhouse effect [370]. The synthesis gas (a mixture of CO and H₂) produced by dry reforming of methane (DRM) is an important raw material for alcohols, olefins, and Fischer-Tropsch products [371, 372]. However, the inherent inactive of CH₄ and CO₂ molecules, along with the high endothermic properties of DRM in the reaction, requires high temperatures ($T > 1000$ K) to drive this thermal catalytic reaction, which inevitably causes to coke deposition and catalyst deactivation [373]. Although a large number of catalytic materials (such as polyatomic clusters) have been found to be capable of activating CH₄ or CO₂, the number of catalysts that can promote the co-conversion of CH₄ and CO₂ under specific reaction conditions is still very limited to date [376–379]. The catalytic conversion of CH₄ and CO₂ to syngas involves complex basic

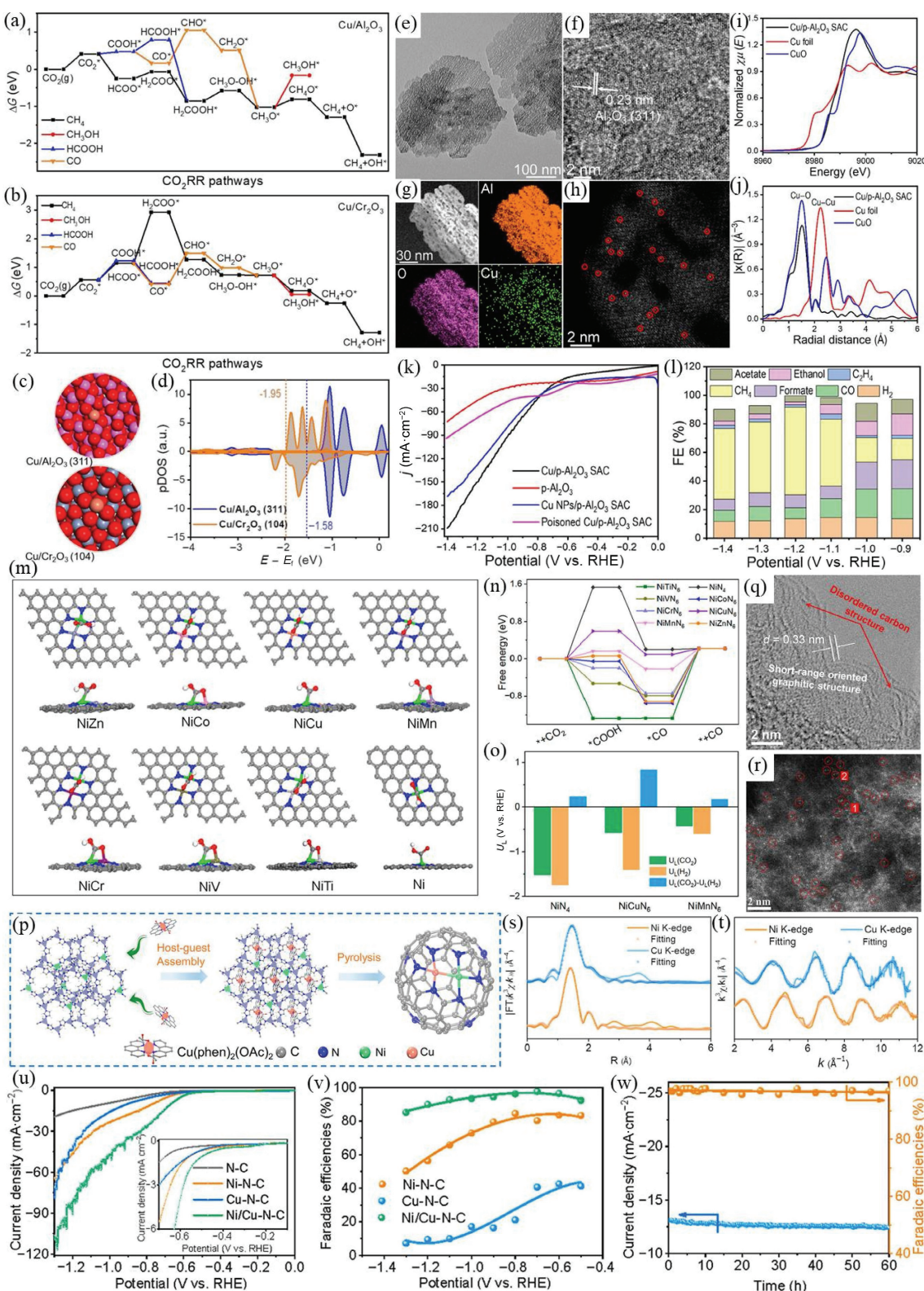


Figure 22 (a) Free energy diagrams for the CO₂RR over Cu/Al₂O₃ SAC and (b) Cu/Cr₂O₃ SAC. (c) Electronic structure and (d) projected densities of states (pDOS) of d-orbitals with an aligned Fermi level of Cu/Al₂O₃ SAC and Cu/Cr₂O₃ SAC. Color code: Cu, brick red; Al, purple; Cr, gray; O, red. (e)–(h) TEM image, HRTEM image, the corresponding EDS elemental mapping images, and AC-HAADF-STEM image (atom-dispersed Cu is highlighted in red circles) of the Cu/p-Al₂O₃ SAC. (i) Cu K-edge XANES spectra and (j) Cu K-edge FT k^2 -weighted $\chi(k)$ function of the Cu/p-Al₂O₃ SAC, Cu foil, and CuO. (k) LSV curves for the Cu/p-Al₂O₃ SAC, p-Al₂O₃, Cu NPs/p-Al₂O₃ and poisoned Cu/p-Al₂O₃ SAC. (l) FEs of various products determined for the Cu/p-Al₂O₃ SAC. Reproduced with permission from Ref. [352], © American Chemical Society 2021. (m) Optimized configurations for COOH* adsorbed on the NiMn₆ (M = Zn, Co, Cu, Mn, Cr, V and Ti) and pristine NiN₄ sites. (n) Gibbs free energy profiles for the electroreduction of CO₂ to CO on the NiMn₆ and NiN₄ sites (gray: C; red: O; blue: N; green: Ni; gray-blue: Zn; pink: Co; orange: Cu; pinkish: Mn; purple: Cr; army green: V; and light gray: Ti). (o) Calculated limiting potentials for CO₂ reduction, H₂ evolution, and their difference. (p) Schematic illustration of the synthetic procedure of the diatomic Ni/Cu-N-C catalyst. (q) HRTEM image of Ni/Cu-N-C. (r) AC-HAADF-STEM image of Ni/Cu-N-C. (s) and (t) Experimental and fitting EXAFS curves of Ni/Cu-N-C in R and k spaces. (u) LSV curves acquired in CO₂-saturated 0.5 M KHCO₃ solution on a rotating disc electrode at a rotating speed of 1600 rpm. The inset highlights the LVS curves in the potential range from -0.1 to -0.7 V. (v) Faradaic efficiency for CO production at various applied potentials. (w) Current–time response and the corresponding Faradaic efficiency for CO production on NiCuN₆ at a fixed potential of -0.7 V. Reproduced with permission from Ref. [353], © American Chemical Society 2022.

steps, and in actual thermal catalysis, almost all basic reactions are carried out under high temperature conditions. Asmis's et al. calculated the reaction paths of RhTiO_2^- with CH_4 , $\text{RhTiO}_2\text{CH}_4^-$ with CO_2 respectively using DFT [370]. As shown in Figs. 23(a) and 23(b), CH_4 first formed stable intermediate I2 through oxidative addition ($\text{I}1 \rightarrow \text{I}2$), and then reacted with CO_2 to generate I5. After a series of conversion steps, $\text{RhTiO}_2\text{CO}^-$ was further generated. Eventually, the second CO was desorbed to produce RhTiO_2^- and sealed the cycle path involving DRM to syngas. The total endothermic of the whole process was 2.74 eV. A deep understanding of the basic steps of the specific reactions in this study will promote the application of temperature programmed methods, laying a solid foundation for accurately designing the actual catalytic reaction process of DRM at room or high temperatures.

In addition, methanol is the upstream raw material for the preparation of formaldehyde, dimethyl ether, acetic acid, methyl tert-butyl ether (MTBE), dimethyl formamide (DMF),

methylamine and a series of important chemical products. In 2006, George A. Olah et al. introduced the “hydrogen economy” and its limitations in the book “Crossing the Oil and Gas Age: the Methanol Economy”, and then proposed the concept of “methanol economy”, and very forward-looking put forward the idea of using industrial emissions and natural CO_2 to synthesize methanol and dimethylether (DME). Using the greenhouse gas CO_2 as raw material to synthesize methanol is a green and environmentally friendly potential technology, so it has attracted widespread attention. Traditional copper-based catalysts are the most widely studied catalysts for CO_2 hydrogenation to methanol. The classic catalyst is mainly composed of Cu and ZnO catalytic active components, and supports such as Al_2O_3 , SiO_2 , and ZrO_2 etc. The reaction of CO_2 hydrogenation to methanol is an exothermic reaction with reduced molecular number, so high pressure and low temperature are thermodynamically advantageous. However, CO_2 molecules are extremely stable, so high temperatures are kinetically conducive to the conversion of

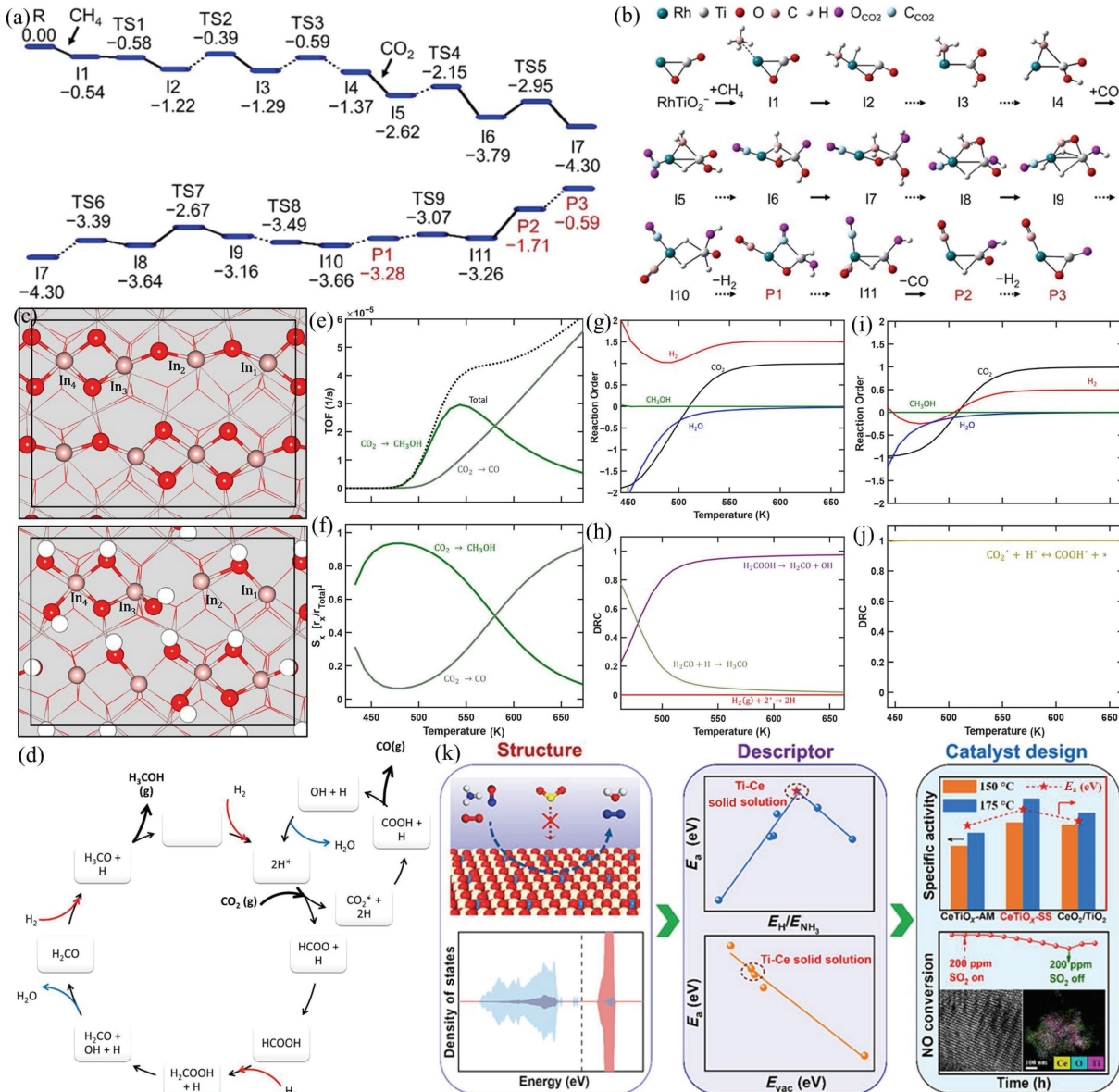


Figure 23 (a) and (b) DFT-calculated potential energy profile for the reaction of $\text{RhTiO}_2^- + \text{CH}_4 + \text{CO}_2$ (R) reaction. Reproduced with permission from Ref. [370], © Wiley-VCH GmbH 2021. (c) Structural model of pristine (top) and 83% H covered (bottom) In_2O_3 (110). (d) Schematic of the investigated catalytic cycle for CO_2 hydrogenation and the RWGS over In_2O_3 (110). (e) Turnover frequency and (f) Selectivity as a function of temperature. Temperature-dependent kinetic analysis of the RWGS reaction: (g) reaction orders of CO_2 , H_2 , H_2O , and CH_3OH ; (h) degree of rate control. Temperature-dependent kinetic analysis of the RWGS reaction: (i) reaction orders of CO_2 , H_2 , H_2O , and CH_3OH ; (j) degree of rate control. Reproduced with permission from Ref. [374], © American Chemical Society 2021. (k) DFT calculations guide the design of effective Ti-Ce solid solution catalysts for $\text{NH}_3\text{-SCR}$. Reproduced with permission from Ref. [375], © American Chemical Society 2022.

carbon dioxide. It can be seen that high pressure and appropriate temperature are in favor of the high yield of methanol. In view of this, the Grönbeck group reported using DFT calculation simulation integrating of mean-field microkinetic modeling to reveal the reaction path and mechanism of CO₂ hydrogenation to methanol on the In₂O₃ (110) crystal plane model [374]. The author studied the reaction process of CO₂ hydrogenation to obtain HCOOH and the competitive reverse water-gas shift (RWGS) through establishing appropriate models (Figs. 23(c) and 23(d)). The changes of turn of frequency (TOF), selectivity and reaction orders with temperature were studied by theoretical calculation modeling method, and the calculated results were consistent with the relevant experimental results (Figs. 23(e)–23(j)). The author found that in the temperature range of 470–670 K, the generation of methanol was dynamically controlled by the reaction of H₂COOH cutting off to produce H₂CO + OH, and the kinetics of RWGS was only closely related to CO₂ hydrogenation to generate COOH. In general, research on reaction kinetics has shown that enhancing the stability of H₂ adsorption is a very vital strategy for improving catalytic reaction activity.

Moreover, nitrogen oxides (NO_x) emitted from industrial waste gas and vehicle exhaust is one of the main precursors of fine particles (PM 2.5) in the atmosphere, which can also produce photochemical smog and acid precipitation, seriously endangering human life and health and damaging the ecological environment. Developing efficient catalysts for NO_x catalytic purification (denitrification) is a key technical issue in achieving NO_x emission reduction. Recently, Liu et al. adopted the strategy of DFT theoretical calculation to guide catalyst structure design for selective catalytic reduction of NO_x with NH₃ (NH₃-SCR) (Fig. 23(k)) [375]. The surface structure of Ti-doped CeO₂ solid solution was precisely controlled at the atomic level, and a high activity and high sulfur resistance Ce-Ti solid solution catalyst with low temperature NH₃-SCR was obtained. Through comprehensive analysis of DFT calculations and experimental results, it was concluded that E_H/E_{NH_3} and E_{vac} were the “reaction descriptors” that affected the activity of Ce-Ti-based catalysts. The special geometric structure and electronic structure of Ti site in Ce-Ti solid solution facilitated it to play the role of SO₂ capture site, thus effectively protecting the catalytic active center. This study provided a new understanding and theoretical basis for the design of high activity and high sulfur resistance rare earth cerium based low-temperature NH₃-SCR catalysts.

Propylene is an important chemical raw material, with not only diversified production processes but also a rich downstream industrial chain, playing a huge role in industrial production. The propane dehydrogenation to obtain propylene production is currently one of the most promising technologies and has attracted widespread attention in recent years [380–382]. However, the existing PDH process mainly relies on mature process packages imported at high prices, and the catalyst as the core of the process is firmly controlled by developed countries. Although a large number of propane dehydrogenation catalysts have been developed in current research, their performance still needs to be improved. Compared with the traditional experimental trial and error method, refining the predictive descriptors through DFT calculation can accelerate the process of catalyst design. However, it is still a huge challenge to reasonably interpret the micro-environment of catalytic sites in alloys and extract corresponding descriptors that are directly related to catalytic performance. Gong et al. proposed a methodology of “predicting catalytic performance through catalytic micro-environment” [383]. The core of this method is to quantitatively interpret the catalytic microenvironment and then correlate it with

changes in catalytic performance. Considering the influence of geometry and electronic structure on the catalytic environment, this study specifically adopts the idea of “decoupling these two and quantitatively describing them separately”. With the “repulsive effect of adsorbate and active site” as the link, the quantitative description of these two is coupled using a simple mathematical form to condense the “degree-of-isolation” of the micro environment descriptor. In theoretical calculations and experiments, both the “isolation degree” and propylene selectivity exhibit a “Volcanic” relationship, revealing the Sabatier principle for the design of single site alloy catalysts. This indicates that the repulsive effect of sites on adsorbates should not be too strong or too weak, and catalysts with moderate “degree-of-isolation” will present the excellent catalytic performance.

5 Summary and perspective

Traditional material synthesis involves multiple parameters and often requires constant trial and error to obtain ideal synthesis conditions, which is not only time-consuming and laborious, but also has a low success rate [384]. Especially for materials with complex components or structures, such as organic molecules, polymers, and organic-inorganic hybrid materials, due to their enormous adjustability in chemical space and synthesis pathways, they often require significant trial and error costs. And in this process, experienced and intuitive experimenters are also required to design and complete experiments. So developing new tools can help efficiently and quickly explore the synthesis reaction space.

Following the synthesis, the fine structure and composition in atomic scale materials must be probed utilizing advanced characterization technology to confirm the atomically dispersed structure and investigate the intrinsic atomic and electronic structures, further reveal the relationship between the structure and the catalytic activity. Advanced characterization techniques are important for the development of efficient catalysts, which will provide strong evidence for the electronic and structural properties. The aberration-corrected scanning transmission electron microscopy (AC-STEM) with sub-Å resolution can directly observe the distribution of metal sites at atomic level, and even obtain single atoms [385]. Meanwhile, synchrotron-radiated XAFS is also a powerful tool for obtaining detailed information to determine the local atomic and electronic structures of catalysts [386]. The FT-EXAFS spectrum can be used to extract the coordination number and bond length changes between the central atom and the adjacent atoms. The wavelet transform is a perfect complement to FT, which can also distinguish backscattered atoms when they substantially overlap in R space, but provide strong resolution in k and R space [387]. In addition, DFT can also better confirm the configuration of catalysts and provide important information on the atomic structure [388].

Furthermore, compared to the preparation of relatively mature nanocatalysts, atomically dispersed materials often face greater challenges and difficulties in design and synthesis. The main challenge in the field of SACs is to firmly anchor individual metal atoms onto high surface area and low-cost carriers with high-density metal atoms. It has been determined that the catalytic activity is limited by the low single atom loading on the carrier (usually less than 5 wt.%). The aggregation during the synthesis process usually limits the metal loading of single atoms. During this process, further metal atom deposition tends to adsorb onto existing metal atoms, leading to agglomeration. Therefore, for industrial applications, new ALD strategies, such as region-selectivity deposition, should be explored to improve the loading of single atoms on the supports. The stable SAC with high metal load is expected to make breakthroughs in many fields such as



energy production, vehicle emission control, water purification and chemical production.

With the continuous development of artificial intelligence technology, it has begun to play a powerful role in the field of chemical synthesis. As the core of artificial intelligence, machine learning has now penetrated into all aspects of the research field. Among them, machine learning has shown great potential in guiding accelerated material research. Recently, with the rise of machine learning methods, it has become a new research hotspot and presented great potential in substantially accelerating materials development [48–50]. For example, Atwood et al. used machine learning algorithms for the synthesis and preparation of metal organic nanocapsules for the first time [389], which can reduce the number of synthesis reactions to reduce human and material investment, and can also deeply analyze the chemical insights behind reaction conditions to guide the next research direction. This method can also be extended to the synthesis and discovery of other inorganic–organic hybrid compound by changing the chemical characteristics of the machine learning algorithm. At the same time, the machine learning algorithm and high-throughput synthesis will also bring infinite possibilities for the discovery and development of advanced catalysts. In addition, the relevant models of machine learning have been successfully applied to the performance prediction of perovskite halides, metallic glasses, shape memory alloys and inorganic organic hybrid material, and have shown relatively ideal results [49]. DFT technology based on machine learning has shown great advantages in efficient catalyst screening. Its advantage lies in the high efficiency given by “data driven” source, while its disadvantage lies in the dependence on a large number of high-quality data caused by “data driven”. Based on this, we call on researchers to provide accurate, detailed, and repeatable calculations and experimental data as much as possible in their research work, which will inevitably promote more important progress in catalyst research and development. We also hope that in the future, artificial intelligence can achieve more and more breakthroughs in more diverse research fields.

Acknowledgements

This work was supported by the National Key R&D Program of China (No. 2018YFA0702003), the National Natural Science Foundation of China (Nos. 21890383 and 22171157). L. G. W. acknowledges the funding support from the Project funded by China Postdoctoral Science Foundation (No. 2022M711787) and the Shuimu Tsinghua Scholar program (No. 2021SM071) of Tsinghua University, China.

References

- [1] Yang, J. R.; Li, W. H.; Tang, H. T.; Pan, Y. M.; Wang, D. S.; Li, Y. D. CO₂-mediated organocatalytic chlorine evolution under industrial conditions. *Nature* **2023**, *617*, 519–523.
- [2] Smil, V. Detonator of the population explosion. *Nature* **1999**, *400*, 415–415.
- [3] Morawetz, H. Difficulties in the emergence of the polymer concept—an essay. *Angew. Chem., Int. Ed.* **1987**, *26*, 93–97.
- [4] Mühlaupt, R. Hermann staudinger and the origin of macromolecular chemistry. *Angew. Chem., Int. Ed.* **2004**, *43*, 1054–1063.
- [5] Wang, L. G.; Wang, D. S.; Li, Y. D. Single-atom catalysis for carbon neutrality. *Carbon Energy* **2022**, *4*, 1021–1079.
- [6] Baláž, P.; Achimovičová, M.; Baláž, M.; Billik, P.; Cherkezova-Zheleva, Z.; Criado, J. M.; Delogu, F.; Dutková, E.; Gaffet, E.; Gotor, F. J. et al. Hallmarks of mechanochemistry: From nanoparticles to technology. *Chem. Soc. Rev.* **2013**, *42*, 7571–7637.
- [7] Tan, C. L.; Cao, X. H.; Wu, X. J.; He, Q. Y.; Yang, J.; Zhang, X.; Chen, J. Z.; Zhao, W.; Han, S. K.; Nam, G. H. et al. Recent advances in ultrathin two-dimensional nanomaterials. *Chem. Rev.* **2017**, *117*, 6225–6331.
- [8] Wang, X.; Zhuang, J.; Peng, Q.; Li, Y. D. A general strategy for nanocrystal synthesis. *Nature* **2005**, *437*, 121–124.
- [9] Shi, Y. M.; Zhang, B. Recent advances in transition metal phosphide nanomaterials: Synthesis and applications in hydrogen evolution reaction. *Chem. Soc. Rev.* **2016**, *45*, 1529–1541.
- [10] Gao, J. H.; Gu, H. W.; Xu, B. Multifunctional magnetic nanoparticles: Design, synthesis, and biomedical applications. *Acc. Chem. Res.* **2009**, *42*, 1097–1107.
- [11] Gao, M. R.; Xu, Y. F.; Jiang, J.; Yu, S. H. Nanostructured metal chalcogenides: Synthesis, modification, and applications in energy conversion and storage devices. *Chem. Soc. Rev.* **2013**, *42*, 2986–3017.
- [12] Guo, S. J.; Dong, S. J. Graphene nanosheet: Synthesis, molecular engineering, thin film, hybrids, and energy and analytical applications. *Chem. Soc. Rev.* **2011**, *40*, 2644–2672.
- [13] Wang, G. F.; Peng, Q.; Li, Y. D. Lanthanide-doped nanocrystals: Synthesis, optical-magnetic properties, and applications. *Acc. Chem. Res.* **2011**, *44*, 322–332.
- [14] Xu, H. X.; Zeiger, B. W.; Suslick, K. S. Sonochemical synthesis of nanomaterials. *Chem. Soc. Rev.* **2013**, *42*, 2555–2567.
- [15] Qiao, B. T.; Wang, A. Q.; Yang, X. F.; Allard, L. F.; Jiang, Z.; Cui, Y. T.; Liu, J. Y.; Li, J.; Zhang, T. Single-atom catalysis of CO oxidation using Pt₁/FeO_x. *Nat. Chem.* **2011**, *3*, 634–641.
- [16] Wang, A. Q.; Li, J.; Zhang, T. Heterogeneous single-atom catalysis. *Nat. Rev. Chem.* **2018**, *2*, 65–81.
- [17] Wang, S. W.; Wang, L. G.; Wang, D. S.; Li, Y. D. Recent advances of single-atom catalysts in CO₂ conversion. *Energy Environ. Sci.* **2023**, *16*, 2759–2803.
- [18] Liang, X.; Fu, N. H.; Yao, S. C.; Li, Z.; Li, Y. D. The progress and outlook of metal single-atom-site catalysis. *J. Am. Chem. Soc.* **2022**, *144*, 18155–18174.
- [19] Xu, Q.; Guo, C. X.; Li, B. B.; Zhang, Z. D.; Qiu, Y. J.; Tian, S. B.; Zheng, L. R.; Gu, L.; Yan, W. S.; Wang, D. S. et al. Al³⁺ dopants induced Mg²⁺ vacancies stabilizing single-atom Cu catalyst for efficient free-radical hydrophosphinylation of alkenes. *J. Am. Chem. Soc.* **2022**, *144*, 4321–4326.
- [20] Chen, Y. J.; Jiang, B.; Hao, H. G.; Li, H. J.; Qiu, C. Y.; Liang, X.; Qu, Q. Y.; Zhang, Z. D.; Gao, R.; Duan, D. M. et al. Atomic-level regulation of cobalt single-atom enzymes: Engineering high-efficiency catalase mimics. *Angew. Chem., Int. Ed.* **2023**, *62*, e202301879.
- [21] Ji, S. F.; Chen, Y. J.; Wang, X. L.; Zhang, Z. D.; Wang, D. S.; Li, Y. D. Chemical synthesis of single atomic site catalysts. *Chem. Rev.* **2020**, *120*, 11900–11955.
- [22] Chen, Y. J.; Ji, S. F.; Chen, C.; Peng, Q.; Wang, D. S.; Li, Y. D. Single-atom catalysts: Synthetic strategies and electrochemical applications. *Joule* **2018**, *2*, 1242–1264.
- [23] Lang, R.; Du, X. R.; Huang, Y. K.; Jiang, X. Z.; Zhang, Q.; Guo, Y. L.; Liu, K. P.; Qiao, B. T.; Wang, A. Q.; Zhang, T. Single-atom catalysts based on the metal-oxide interaction. *Chem. Rev.* **2020**, *120*, 11986–12043.
- [24] Zhuo, H. Y.; Zhang, X.; Liang, J. X.; Yu, Q.; Xiao, H.; Li, J. Theoretical understandings of graphene-based metal single-atom catalysts: Stability and catalytic performance. *Chem. Rev.* **2020**, *120*, 12315–12341.
- [25] Gao, C.; Low, J.; Long, R.; Kong, T. T.; Zhu, J. F.; Xiong, Y. J. Heterogeneous single-atom photocatalysts: Fundamentals and applications. *Chem. Rev.* **2020**, *120*, 12175–12216.
- [26] Wei, Y. S.; Zhang, M.; Zou, R. Q.; Xu, Q. Metal-organic framework-based catalysts with single metal sites. *Chem. Rev.* **2020**, *120*, 12089–12174.
- [27] Qin, R. X.; Liu, K. L.; Wu, Q. Y.; Zheng, N. F. Surface coordination chemistry of atomically dispersed metal catalysts. *Chem. Rev.* **2020**, *120*, 11810–11899.
- [28] Kaiser, S. K.; Chen, Z. P.; Akl, D. F.; Mitchell, S.; Pérez-Ramírez, J. Single-atom catalysts across the periodic table. *Chem. Rev.* **2020**, *120*, 11703–11809.
- [29] Seh, Z. W.; Kibsgaard, J.; Dickens, C. F.; Chorkendorff, I.;

- Nørskov, J. K.; Jaramillo, T. F. Combining theory and experiment in electrocatalysis: Insights into materials design. *Science* **2017**, *355*, eaad4998.
- [30] Suen, N. T.; Hung, S. F.; Quan, Q.; Zhang, N.; Xu, Y. J.; Chen, H. M. Electrocatalysis for the oxygen evolution reaction: Recent development and future perspectives. *Chem. Soc. Rev.* **2017**, *46*, 337–365.
- [31] Shao, M. H.; Chang, Q. W.; Dodelet, J. P.; Chenitz, R. Recent advances in electrocatalysts for oxygen reduction reaction. *Chem. Rev.* **2016**, *116*, 3594–3657.
- [32] Hong, W. T.; Risch, M.; Stoerzinger, K. A.; Grimaud, A.; Suntivich, J.; Shao-Horn, Y. Toward the rational design of non-precious transition metal oxides for oxygen electrocatalysis. *Energy Environ. Sci.* **2015**, *8*, 1404–1427.
- [33] Wang, Y.; Zheng, M.; Li, Y. R.; Ye, C. L.; Chen, J.; Ye, J. Y.; Zhang, Q. H.; Li, J.; Zhou, Z. Y.; Fu, X. Z. et al. p-d orbital hybridization induced by a monodispersed Ga site on a Pt₃Mn nanocatalyst boosts ethanol electrooxidation. *Angew. Chem., Int. Ed.* **2022**, *61*, e202115735.
- [34] Hoffmann, M. R.; Martin, S. T.; Choi, W.; Bahnemann, D. W. Environmental applications of semiconductor photocatalysis. *Chem. Rev.* **1995**, *95*, 69–96.
- [35] Asahi, R.; Morikawa, T.; Ohwaki, T.; Aoki, K.; Taga, Y. Visible-light photocatalysis in nitrogen-doped titanium oxides. *Science* **2001**, *293*, 269–271.
- [36] Ong, W. J.; Tan, L. L.; Ng, Y. H.; Yong, S. T.; Chai, S. P. Graphitic carbon nitride (g-C₃N₄)-based photocatalysts for artificial photosynthesis and environmental remediation: Are we a step closer to achieving sustainability. *Chem. Rev.* **2016**, *116*, 7159–7329.
- [37] Fox, M. A.; Dulay, M. T. Heterogeneous photocatalysis. *Chem. Rev.* **1993**, *93*, 341–357.
- [38] Wang, G.; Chen, Z.; Wang, T.; Wang, D. S.; Mao, J. J. P and Cu dual sites on graphitic carbon nitride for photocatalytic CO₂ reduction to hydrocarbon fuels with high C₂H₆ evolution. *Angew. Chem., Int. Ed.* **2022**, *61*, e202210789.
- [39] Wang, G.; Wu, Y.; Li, Z. J.; Lou, Z. Z.; Chen, Q. Q.; Li, Y. F.; Wang, D. S.; Mao, J. J. Engineering a copper single-atom electron bridge to achieve efficient photocatalytic CO₂ conversion. *Angew. Chem., Int. Ed.* **2023**, *62*, e202218460.
- [40] Tackett, B. M.; Gomez, E.; Chen, J. G. Net reduction of CO₂ via its thermocatalytic and electrocatalytic transformation reactions in standard and hybrid processes. *Nat. Catal.* **2019**, *2*, 381–386.
- [41] Meng, X. G.; Cui, X. J.; Rajan, N. P.; Yu, L.; Deng, D. H.; Bao, X. H. Direct methane conversion under mild condition by thermo-, electro-, or photocatalysis. *Chem* **2019**, *5*, 2296–2325.
- [42] Zhang, F. F.; Zhu, Y. L.; Lin, Q.; Zhang, L.; Zhang, X. W.; Wang, H. T. Noble-metal single-atoms in thermocatalysis, electrocatalysis, and photocatalysis. *Energy Environ. Sci.* **2021**, *14*, 2954–3009.
- [43] Gan, T.; Wang, D. S. Atomically dispersed materials: Ideal catalysts in atomic era. *Nano Res.*, in press, DOI: 10.1007/s12274-023-5700-4.
- [44] Meng, G.; Lan, W.; Zhang, L. L.; Wang, S. B.; Zhang, T. H.; Zhang, S.; Xu, M.; Wang, Y.; Zhang, J.; Yue, F. X. et al. Synergy of single atoms and lewis acid sites for efficient and selective lignin disassembly into monolignol derivatives. *J. Am. Chem. Soc.* **2023**, *145*, 12884–12893.
- [45] Ning, S. B.; Ou, H. H.; Li, Y. G.; Lv, C. C.; Wang, S. F.; Wang, D. S.; Ye, J. H. Co⁰–Co³⁺ interface double-site-mediated C–C coupling for the photothermal conversion of CO₂ into light olefins. *Angew. Chem., Int. Ed.* **2023**, *62*, e202302253.
- [46] Ling, C. Y.; Cui, Y.; Lu, S. H.; Bai, X. W.; Wang, J. L. How computations accelerate electrocatalyst discovery. *Chem* **2022**, *8*, 1575–1610.
- [47] Chun, H.; Lee, E.; Nam, K.; Jang, J. H.; Kyung, W.; Noh, S. H.; Han, B. First-principle-data-integrated machine-learning approach for high-throughput searching of ternary electrocatalyst toward oxygen reduction reaction. *Chem Catal.* **2021**, *1*, 855–869.
- [48] Yang, J. R.; Li, W. H.; Wang, D. S. Machine learning: The trends of developing high-efficiency single-atom materials. *Chem Catal.* **2021**, *1*, 24–26.
- [49] Tang, B. J.; Lu, Y. H.; Zhou, J. D.; Chouhan, T.; Wang, H.; Golani, P.; Xu, M. Z.; Xu, Q.; Guan, C. T.; Liu, Z. Machine learning-guided synthesis of advanced inorganic materials. *Mater. Today* **2020**, *41*, 72–80.
- [50] Raccuglia, P.; Elbert, K. C.; Adler, P. D. F.; Falk, C.; Wenny, M. B.; Mollo, A.; Zeller, M.; Friedler, S. A.; Schrier, J.; Norquist, A. J. Machine-learning-assisted materials discovery using failed experiments. *Nature* **2016**, *533*, 73–76.
- [51] Brent, J. R.; Savjani, N.; O'Brien, P. Synthetic approaches to two-dimensional transition metal dichalcogenide nanosheets. *Prog. Mater. Sci.* **2017**, *89*, 411–478.
- [52] Chen, Y.; Fan, Z. X.; Zhang, Z. C.; Niu, W. X.; Li, C. L.; Yang, N. L.; Chen, B.; Zhang, H. Two-dimensional metal nanomaterials: Synthesis, properties, and applications. *Chem. Rev.* **2018**, *118*, 6409–6455.
- [53] Li, J.; Jing, X. C.; Li, Q. Q.; Li, S. W.; Gao, X.; Feng, X.; Wang, B. Bulk COFs and COF nanosheets for electrochemical energy storage and conversion. *Chem. Soc. Rev.* **2020**, *49*, 3565–3604.
- [54] Dong, R. H.; Zhang, T.; Feng, X. L. Interface-assisted synthesis of 2D materials: Trend and challenges. *Chem. Rev.* **2018**, *118*, 6189–6235.
- [55] Feinle, A.; Elsaesser, M. S.; Hüsing, N. Sol-gel synthesis of monolithic materials with hierarchical porosity. *Chem. Soc. Rev.* **2016**, *45*, 3377–3399.
- [56] Ma, R. Z.; Sasaki, T. Nanosheets of oxides and hydroxides: Ultimate 2D charge-bearing functional crystallites. *Adv. Mater.* **2010**, *22*, 5082–5104.
- [57] Mei, J.; Liao, T.; Kou, L. Z.; Sun, Z. Q. Two-dimensional metal oxide nanomaterials for next-generation rechargeable batteries. *Adv. Mater.* **2017**, *29*, 1700176.
- [58] Nicolosi, V.; Chhowalla, M.; Kanatzidis, M. G.; Strano, M. S.; Coleman, J. N. Liquid exfoliation of layered materials. *Science* **2013**, *340*, 1226419.
- [59] Coleman, J. N.; Lotya, M.; O'Neill, A.; Bergin, S. D.; King, P. J.; Khan, U.; Young, K.; Gaucher, A.; De, S.; Smith, R. J. et al. Two-dimensional nanosheets produced by liquid exfoliation of layered materials. *Science* **2011**, *331*, 568–571.
- [60] Abid, N.; Khan, A. M.; Shujait, S.; Chaudhary, K.; Ikram, M.; Imran, M.; Haider, J.; Khan, M.; Khan, Q.; Maqbool, M. Synthesis of nanomaterials using various top-down and bottom-up approaches, influencing factors, advantages, and disadvantages: A review. *Adv. Colloid Interface Sci.* **2022**, *300*, 102597.
- [61] Schiøtz, J.; Di Tolla, F. D.; Jacobsen, K. W. Softening of nanocrystalline metals at very small grain sizes. *Nature* **1998**, *391*, 561–563.
- [62] Pietryga, J. M.; Park, Y. S.; Lim, J.; Fidler, A. F.; Bae, W. K.; Brovelli, S.; Klimov, V. I. Spectroscopic and device aspects of nanocrystal quantum dots. *Chem. Rev.* **2016**, *116*, 10513–10622.
- [63] Melnychuk, C.; Guyot-Sionnest, P. Multicarrier dynamics in quantum dots. *Chem. Rev.* **2021**, *121*, 2325–2372.
- [64] Xia, Y.; Chen, W.; Zhang, P.; Liu, S. S.; Wang, K.; Yang, X. K.; Tang, H. D.; Lian, L. Y.; He, J. G.; Liu, X. X. et al. Facet control for trap-state suppression in colloidal quantum dot solids. *Adv. Funct. Mater.* **2020**, *30*, 2000594.
- [65] Xia, Y.; Liu, S. S.; Wang, K.; Yang, X. K.; Lian, L. Y.; Zhang, Z. M.; He, J. G.; Liang, G. J.; Wang, S.; Tan, M. L. et al. Cation-exchange synthesis of highly monodisperse PbS quantum dots from ZnS nanorods for efficient infrared solar cells. *Adv. Funct. Mater.* **2020**, *30*, 1907379.
- [66] Fan, J. Z.; Andersen, N. T.; Biondi, M.; Todorović, P.; Sun, B.; Ouellette, O.; Abed, J.; Sagar, L. K.; Choi, M. J.; Hoogland, S. et al. Mixed lead halide passivation of quantum dots. *Adv. Mater.* **2019**, *31*, 1904304.
- [67] Wang, R. L.; Wu, X.; Xu, K. M.; Zhou, W. J.; Shang, Y. Q.; Tang, H. Y.; Chen, H.; Ning, Z. J. Highly efficient inverted structural quantum dot solar cells. *Adv. Mater.* **2018**, *30*, 1704882.
- [68] Yang, J.; Ling, T.; Wu, W. T.; Liu, H.; Gao, M. R.; Ling, C.; Li, L.; Du, X. W. A top-down strategy towards monodisperse colloidal lead sulphide quantum dots. *Nat. Commun.* **2013**, *4*, 1695.
- [69] Tavakoli, M. M.; Dastjerdi, H. T.; Yadav, P.; Prochowicz, D.; Si, H. Y.; Tavakoli, R. Ambient stable and efficient monolithic tandem



- perovskite/PbS quantum dots solar cells via surface passivation and light management strategies. *Adv. Funct. Mater.* **2021**, *31*, 2010623.
- [70] Wang, Y.; Liu, X. Q.; Liu, J.; Han, B.; Hu, X. Q.; Yang, F.; Xu, Z. W.; Li, Y. C.; Jia, S. R.; Li, Z. et al. Carbon quantum dot implanted graphite carbon nitride nanotubes: Excellent charge separation and enhanced photocatalytic hydrogen evolution. *Angew. Chem., Int. Ed.* **2018**, *57*, 5765–5771.
- [71] Jin, Y. C.; Hu, C. G.; Dai, Q. B.; Xiao, Y.; Lin, Y.; Connell, J. W.; Chen, F. Y.; Dai, L. M. High-performance Li-CO₂ batteries based on metal-free carbon quantum dot/holey graphene composite catalysts. *Adv. Funct. Mater.* **2018**, *28*, 1804630.
- [72] Younis, A.; Hu, L.; Sharma, P.; Lin, C. H.; Mi, Y.; Guan, X. W.; Zhang, D. W.; Wang, Y. T.; He, T. Y.; Liu, X. F. et al. Enhancing resistive switching performance and ambient stability of hybrid perovskite single crystals via embedding colloidal quantum dots. *Adv. Funct. Mater.* **2020**, *30*, 2002948.
- [73] Arancibia, V.; Valderrama, M.; Silva, K.; Tapia, T. Determination of chromium in urine samples by complexation-supercritical fluid extraction and liquid or gas chromatography. *J. Chromatogr. B* **2003**, *785*, 303–309.
- [74] Bottini, M.; Balasubramanian, C.; Dawson, M. I.; Bergamaschi, A.; Bellucci, S.; Mustelin, T. Isolation and characterization of fluorescent nanoparticles from pristine and oxidized electric arc-produced single-walled carbon nanotubes. *J. Phys. Chem. B* **2006**, *110*, 831–836.
- [75] Lim, S. Y.; Shen, W.; Gao, Z. Q. Carbon quantum dots and their applications. *Chem. Soc. Rev.* **2015**, *44*, 362–381.
- [76] Bouzas-Ramos, D.; Canga, J. C.; Mayo, J. C.; Sainz, R. M.; Encinar, J. R.; Costa-Fernandez, J. M. Carbon quantum dots codoped with nitrogen and lanthanides for multimodal imaging. *Adv. Funct. Mater.* **2019**, *29*, 1903884.
- [77] Zhang, G.; Ji, Q. H.; Wu, Z.; Wang, G. C.; Liu, H. J.; Qu, J. H.; Li, J. H. Facile “spot-heating” synthesis of carbon dots/carbon nitride for solar hydrogen evolution synchronously with contaminant decomposition. *Adv. Funct. Mater.* **2018**, *28*, 1706462.
- [78] Zhou, S. J.; Tang, R.; Yin, L. W. Slow-photon-effect-induced photoelectrical-conversion efficiency enhancement for carbon-quantum-dot-sensitized inorganic CsPbBr₃ inverse opal perovskite solar cells. *Adv. Mater.* **2017**, *29*, 1703682.
- [79] Wang, Z. F.; Yuan, F. L.; Li, X. H.; Li, Y. C.; Zhong, H. Z.; Fan, L. Z.; Yang, S. H. 53% efficient red emissive carbon quantum dots for high color rendering and stable warm white-light-emitting diodes. *Adv. Mater.* **2017**, *29*, 1702910.
- [80] Li, W. D.; Liu, Y.; Wu, M.; Feng, X. L.; Redfern, S. A. T.; Shang, Y.; Yong, X.; Feng, T. L.; Wu, K. F.; Liu, Z. Y. et al. Carbon-quantum-dots-loaded ruthenium nanoparticles as an efficient electrocatalyst for hydrogen production in alkaline media. *Adv. Mater.* **2018**, *30*, 1800676.
- [81] Hills, G.; Lau, C.; Wright, A.; Fuller, S.; Bishop, M. D.; Srimani, T.; Kanhaiya, P.; Ho, R.; Amer, A.; Stein, Y. et al. Modern microprocessor built from complementary carbon nanotube transistors. *Nature* **2019**, *572*, 595–602.
- [82] Bai, Y. X.; Zhang, R. F.; Ye, X.; Zhu, Z. X.; Xie, H. H.; Shen, B. Y.; Cai, D. L.; Liu, B. F.; Zhang, C. X.; Jia, Z. et al. Carbon nanotube bundles with tensile strength over 80 GPa. *Nat. Nanotechnol.* **2018**, *13*, 589–595.
- [83] Yang, F.; Wang, X.; Zhang, D. Q.; Yang, J.; Luo, D.; Xu, Z. W.; Wei, J. K.; Wang, J. Q.; Xu, Z.; Peng, F. et al. Chirality-specific growth of single-walled carbon nanotubes on solid alloy catalysts. *Nature* **2014**, *510*, 522–524.
- [84] Liang, S.; Zhang, M. Y.; He, S.; Tian, M. K.; Choi, W.; Lian, T. Q.; Lin, Z. Q. Metal halide perovskite nanorods with tailored dimensions, compositions and stabilities. *Nat. Synth.*, in press, DOI: 10.1038/s44160-023-00307-5.
- [85] Zhuang, T. T.; Li, Y.; Gao, X. Q.; Wei, M. Y.; De Arquer, F. P. G.; Todorović, P.; Tian, J.; Li, G. P.; Zhang, C.; Li, X. Y. et al. Regioselective magnetization in semiconducting nanorods. *Nat. Nanotechnol.* **2020**, *15*, 192–197.
- [86] Zhou, G. M.; Xu, L.; Hu, G. W.; Mai, L.; Cui, Y. Nanowires for electrochemical energy storage. *Chem. Rev.* **2019**, *119*, 11042–11109.
- [87] Wang, D. F.; Bao, D. L.; Zheng, Q.; Wang, C. T.; Wang, S. Y.; Fan, P.; Mishra, S.; Tao, L.; Xiao, Y.; Huang, L. et al. Twisted bilayer zigzag-graphene nanoribbon junctions with tunable edge states. *Nat. Commun.* **2023**, *14*, 1018.
- [88] Christoff-Tempesta, T.; Cho, Y.; Kim, D. Y.; Geri, M.; Lamour, G.; Lew, A. J.; Zuo, X. B.; Lindemann, W. R.; Ortony, J. H. Self-assembly of aramid amphiphiles into ultra-stable nanoribbons and aligned nanoribbon threads. *Nat. Nanotechnol.* **2021**, *16*, 447–454.
- [89] Cheung, K. Y.; Watanabe, K.; Segawa, Y.; Itami, K. Synthesis of a zigzag carbon nanobelt. *Nat. Chem.* **2021**, *13*, 255–259.
- [90] Iijima, S. Helical microtubules of graphitic carbon. *Nature* **1991**, *354*, 56–58.
- [91] Iijima, S.; Ichihashi, T. Single-shell carbon nanotubes of 1-nm diameter. *Nature* **1993**, *363*, 603–605.
- [92] Journet, C.; Maser, W. K.; Bernier, P.; Loiseau, A.; De La Chapelle, M. L.; Lefrant, S.; Deniard, P.; Lee, R.; Fischer, J. E. Large-scale production of single-walled carbon nanotubes by the electric-arc technique. *Nature* **1997**, *388*, 756–758.
- [93] Gwyther, R. E. A.; Nekrasov, N. P.; Emelianov, A. V.; Nasibulin, A. G.; Ramakrishnan, K.; Bobrinetskiy, I.; Jones, D. D. Differential bio-optoelectronic gating of semiconducting carbon nanotubes by varying the covalent attachment residue of a green fluorescent protein. *Adv. Funct. Mater.* **2022**, *32*, 2112374.
- [94] Liao, Y. P.; Jiang, H.; Wei, N.; Laiho, P.; Zhang, Q.; Khan, S. A.; Kauppinen, E. I. Direct synthesis of colorful single-walled carbon nanotube thin films. *J. Am. Chem. Soc.* **2018**, *140*, 9797–9800.
- [95] Guo, Y. F.; Shi, E. Z.; Zhu, J. D.; Shen, P. C.; Wang, J. T.; Lin, Y. X.; Mao, Y. W.; Deng, S. B.; Li, B. N.; Park, J. H. et al. Soft-lock drawing of super-aligned carbon nanotube bundles for nanometre electrical contacts. *Nat. Nanotechnol.* **2022**, *17*, 278–284.
- [96] Qian, L.; Xie, Y.; Yu, Y.; Wang, S. S.; Zhang, S. C.; Zhang, J. Growth of single-walled carbon nanotubes with controlled structure: Floating carbide solid catalysts. *Angew. Chem., Int. Ed.* **2020**, *59*, 10884–10887.
- [97] Zhang, S. C.; Kang, L. X.; Wang, X.; Tong, L. M.; Yang, L. W.; Wang, Z. Q.; Qi, K.; Deng, S. B.; Li, Q. W.; Bai, X. D. et al. Arrays of horizontal carbon nanotubes of controlled chirality grown using designed catalysts. *Nature* **2017**, *543*, 234–238.
- [98] Jin, Q.; Jiang, S.; Zhao, Y.; Wang, D.; Qiu, J. H.; Tang, D. M.; Tan, J.; Sun, D. M.; Hou, P. X.; Chen, X. Q. et al. Flexible layer-structured Bi₂Te₃ thermoelectric on a carbon nanotube scaffold. *Nat. Mater.* **2019**, *18*, 62–68.
- [99] Sett, D.; Basak, D. Highly enhanced H₂ gas sensing characteristics of Co: ZnO nanorods and its mechanism. *Sensor. Actuat. B Chem.* **2017**, *243*, 475–483.
- [100] Tian, H. L.; Fan, H. Q.; Li, M. M.; Ma, L. T. Zeolitic imidazolate framework coated ZnO nanorods as molecular sieving to improve selectivity of formaldehyde gas sensor. *ACS Sens.* **2016**, *1*, 243–250.
- [101] Yaghmour, S. J.; Mahmoud, W. E. Synthesis and characterization of self-assembly silver sulfide nanorods prepared by squalene assisted microwave technique. *Mater. Lett.* **2013**, *109*, 55–57.
- [102] Lee, J.; Kim, Y.; Kim, J. K.; Kim, S.; Min, D. H.; Jang, D. J. Highly efficient photocatalytic performances of SnO₂-deposited ZnS nanorods based on interfacial charge transfer. *Appl. Catal. B Environ.* **2017**, *205*, 433–442.
- [103] Zhang, H. Ultrathin two-dimensional nanomaterials. *ACS Nano* **2015**, *9*, 9451–9469.
- [104] Geim, A. K.; Novoselov, K. S. The rise of graphene. *Nat. Mater.* **2007**, *6*, 183–191.
- [105] Geim, A. K. Graphene: Status and prospects. *Science* **2009**, *324*, 1530–1534.
- [106] Raccichini, R.; Varzi, A.; Passerini, S.; Scrosati, B. The role of graphene for electrochemical energy storage. *Nat. Mater.* **2015**, *14*, 271–279.
- [107] Dou, Y. H.; Zhang, L.; Xu, X.; Sun, Z. Q.; Liao, T.; Dou, S. X. Atomically thin non-layered nanomaterials for energy storage and conversion. *Chem. Soc. Rev.* **2017**, *46*, 7338–7373.
- [108] Shahzad, F.; Alhabeb, M.; Hatter, C. B.; Anasori, B.; Hong, S. M.; Koo, C. M.; Gogotsi, Y. Electromagnetic interference shielding

- with 2D transition metal carbides (MXenes). *Science* **2016**, *353*, 1137–1140.
- [109] Neto, A. H. C.; Guinea, F.; Peres, N. M. R.; Novoselov, K. S.; Geim, A. K. The electronic properties of graphene. *Rev. Mod. Phys.* **2009**, *81*, 109–162.
- [110] Jariwala, D.; Sangwan, V. K.; Lauhon, L. J.; Marks, T. J.; Hersam, M. C. Carbon nanomaterials for electronics, optoelectronics, photovoltaics, and sensing. *Chem. Soc. Rev.* **2013**, *42*, 2824–2860.
- [111] Sun, Y. Q.; Wu, Q.; Shi, G. Q. Graphene based new energy materials. *Energy Environ. Sci.* **2011**, *4*, 1113–1132.
- [112] Liu, Y. X.; Dong, X. C.; Chen, P. Biological and chemical sensors based on graphene materials. *Chem. Soc. Rev.* **2012**, *41*, 2283–2307.
- [113] Novoselov, K. S.; Geim, A. K.; Morozov, S. V.; Jiang, D.; Zhang, Y.; Dubonos, S. V.; Grigorieva, I. V.; Firsov, A. A. Electric field effect in atomically thin carbon films. *Science* **2004**, *306*, 666–669.
- [114] Zhou, S. Y.; Gweon, G. H.; Fedorov, A. V.; First, P. N.; De Heer, W. A.; Lee, D. H.; Guinea, F.; Neto, A. H. C.; Lanza, A. Substrate-induced bandgap opening in epitaxial graphene. *Nat. Mater.* **2007**, *6*, 770–775.
- [115] Huang, Y.; Sutter, E.; Shi, N. N.; Zheng, J. B.; Yang, T. Z.; Englund, D.; Gao, H. J.; Sutter, P. Reliable exfoliation of large-area high-quality flakes of graphene and other two-dimensional materials. *ACS Nano* **2015**, *9*, 10612–10620.
- [116] Naguib, M.; Mashatalir, O.; Carle, J.; Presser, V.; Lu, J.; Hultman, L.; Gogotsi, Y.; Barsoum, M. W. Two-dimensional transition metal carbides. *ACS Nano* **2012**, *6*, 1322–1331.
- [117] Liu, K. K.; Zhang, W. J.; Lee, Y. H.; Lin, Y. C.; Chang, M. T.; Su, C. Y.; Chang, C. S.; Li, H.; Shi, Y. M.; Zhang, H. et al. Growth of large-area and highly crystalline MoS₂ thin layers on insulating substrates. *Nano Lett.* **2012**, *12*, 1538–1544.
- [118] Song, F.; Hu, X. L. Exfoliation of layered double hydroxides for enhanced oxygen evolution catalysis. *Nat. Commun.* **2014**, *5*, 4477.
- [119] Georgakilas, V.; Otyepka, M.; Bourlinos, A. B.; Chandra, V.; Kim, N.; Kemp, K. C.; Hobza, P.; Zboril, R.; Kim, K. S. Functionalization of graphene: Covalent and non-covalent approaches, derivatives and applications. *Chem. Rev.* **2012**, *112*, 6156–6214.
- [120] Kong, X. K.; Chen, C. L.; Chen, Q. W. Doped graphene for metal-free catalysis. *Chem. Soc. Rev.* **2014**, *43*, 2841–2857.
- [121] Choi, C. H.; Chung, M. W.; Kwon, H. C.; Park, S. H.; Woo, S. I. B., N- and P, N-doped graphene as highly active catalysts for oxygen reduction reactions in acidic media. *J. Mater. Chem. A* **2013**, *1*, 3694–3699.
- [122] Ding, H. M.; Li, Y. B.; Li, M.; Chen, K.; Liang, K.; Chen, G. X.; Lu, J.; Palisaitis, J.; Persson, P. O. Å.; Eklund, P. et al. Chemical scissor-mediated structural editing of layered transition metal carbides. *Science* **2023**, *379*, 1130–1135.
- [123] Zhang, X.; Lai, Z. C.; Tan, C. L.; Zhang, H. Solution-processed two-dimensional MoS₂ nanosheets: Preparation, hybridization, and applications. *Angew. Chem., Int. Ed.* **2016**, *55*, 8816–8838.
- [124] Fu, Q.; Han, J. C.; Wang, X. J.; Xu, P.; Yao, T.; Zhong, J.; Zhong, W. W.; Liu, S. W.; Gao, T. L.; Zhang, Z. H. et al. 2D transition metal dichalcogenides: Design, modulation, and challenges in electrocatalysis. *Adv. Mater.* **2021**, *33*, 1907818.
- [125] Xie, J. F.; Zhang, H.; Li, S.; Wang, R. X.; Sun, X.; Zhou, M.; Zhou, J. F.; Lou, X. W. D.; Xie, Y. Defect-rich MoS₂ ultrathin nanosheets with additional active edge sites for enhanced electrocatalytic hydrogen evolution. *Adv. Mater.* **2013**, *25*, 5807–5813.
- [126] Kibsgaard, J.; Chen, Z. B.; Reinecke, B. N.; Jaramillo, T. F. Engineering the surface structure of MoS₂ to preferentially expose active edge sites for electrocatalysis. *Nat. Mater.* **2012**, *11*, 963–969.
- [127] Gao, M. R.; Chan, M. K. Y.; Sun, Y. G. Edge-terminated molybdenum disulfide with a 9.4-Å interlayer spacing for electrochemical hydrogen production. *Nat. Commun.* **2015**, *6*, 7493.
- [128] Rao, T. K.; Wang, H. D.; Zeng, Y. J.; Guo, Z. N.; Zhang, H.; Liao, W. G. Phase transitions and water splitting applications of 2D transition metal dichalcogenides and metal phosphorous trichalcogenides. *Adv. Sci. (Weinh.)* **2021**, *8*, 2002284.
- [129] Faraji, M.; Yousefi, M.; Yousefzadeh, S.; Zirak, M.; Naseri, N.; Jeon, T. H.; Choi, W.; Moshfegh, A. Z. Two-dimensional materials in semiconductor photoelectrocatalytic systems for water splitting. *Energy Environ. Sci.* **2019**, *12*, 59–95.
- [130] Qiu, B. C.; Zhu, Q. H.; Du, M. M.; Fan, L. G.; Xing, M. Y.; Zhang, J. L. Efficient solar light harvesting CdS/Co₉S₈ hollow cubes for Z-scheme photocatalytic water splitting. *Angew. Chem., Int. Ed.* **2017**, *56*, 2684–2688.
- [131] Haque, F.; Daeneke, T.; Kalantar-Zadeh, K.; Ou, J. Z. Two-dimensional transition metal oxide and chalcogenide-based photocatalysts. *Nano-Micro Lett.* **2018**, *10*, 23.
- [132] Chang, K.; Mei, Z. W.; Wang, T.; Kang, Q.; Ouyang, S. X.; Ye, J. H. MoS₂/graphene cocatalyst for efficient photocatalytic H₂ evolution under visible light irradiation. *ACS Nano* **2014**, *8*, 7078–7087.
- [133] Pumera, M.; Sofer, Z.; Ambrosi, A. Layered transition metal dichalcogenides for electrochemical energy generation and storage. *J. Mater. Chem. A* **2014**, *2*, 8981–8987.
- [134] Chhowalla, M.; Shin, H. S.; Eda, G.; Li, L. J.; Loh, K. P.; Zhang, H. The chemistry of two-dimensional layered transition metal dichalcogenide nanosheets. *Nat. Chem.* **2013**, *5*, 263–275.
- [135] Yun, Q. B.; Li, L. X.; Hu, Z. N.; Lu, Q. P.; Chen, B.; Zhang, H. Layered transition metal dichalcogenide-based nanomaterials for electrochemical energy storage. *Adv. Mater.* **2020**, *32*, 1903826.
- [136] Sun, Z. Q.; Liao, T.; Dou, Y. H.; Hwang, S. M.; Park, M. S.; Jiang, L.; Kim, J. H.; Dou, S. X. Generalized self-assembly of scalable two-dimensional transition metal oxide nanosheets. *Nat. Commun.* **2014**, *5*, 3813.
- [137] Wang, X.; Chen, W. X.; Zhang, L.; Yao, T.; Liu, W.; Lin, Y.; Ju, H. X.; Dong, J. C.; Zheng, L. R.; Yan, W. S. et al. Uncoordinated amine groups of metal-organic frameworks to anchor single Ru sites as chemoselective catalysts toward the hydrogenation of quinoline. *J. Am. Chem. Soc.* **2017**, *139*, 9419–9422.
- [138] Chen, Y. J.; Ji, S. F.; Wang, Y. G.; Dong, J. C.; Chen, W. X.; Li, Z.; Shen, R. A.; Zheng, L. R.; Zhuang, Z. B.; Wang, D. S. et al. Isolated single iron atoms anchored on N-doped porous carbon as an efficient electrocatalyst for the oxygen reduction reaction. *Angew. Chem., Int. Ed.* **2017**, *56*, 6937–6941.
- [139] Liu, Y. W.; Li, Z.; Yu, Q. Y.; Chen, Y. F.; Chai, Z. W.; Zhao, G. F.; Liu, S. J.; Cheong, W. C.; Pan, Y.; Zhang, Q. H. et al. A general strategy for fabricating isolated single metal atomic site catalysts in Y zeolite. *J. Am. Chem. Soc.* **2019**, *141*, 9305–9311.
- [140] Zhao, C. S.; Zhang, H. T.; Si, W. J.; Wu, H. Mass production of two-dimensional oxides by rapid heating of hydrous chlorides. *Nat. Commun.* **2016**, *7*, 12543.
- [141] Corma, A.; Concepción, P.; Boronat, M.; Sabater, M. J.; Navas, J.; Yacaman, M. J.; Larios, E.; Posadas, A.; López-Quintela, M. A.; Buceta, D. et al. Exceptional oxidation activity with size-controlled supported gold clusters of low atomicity. *Nat. Chem.* **2013**, *5*, 775–781.
- [142] Ortalan, V.; Uzun, A.; Gates, B. C.; Browning, N. D. Direct imaging of single metal atoms and clusters in the pores of dealuminated HY zeolite. *Nat. Nanotechnol.* **2010**, *5*, 506–510.
- [143] Kistler, J. D.; Chotikrai, N.; Xu, P. H.; Enderle, B.; Prasertthdam, P.; Chen, C. Y.; Browning, N. D.; Gates, B. C. A single-site platinum CO oxidation catalyst in zeolite KLTL: Microscopic and spectroscopic determination of the locations of the platinum atoms. *Angew. Chem., Int. Ed.* **2014**, *53*, 8904–8907.
- [144] Luo, E. G.; Zhang, H.; Wang, X.; Gao, L. Q.; Gong, L. Y.; Zhao, T.; Jin, Z.; Ge, J. J.; Jiang, Z.; Liu, C. P. et al. Single-atom Cr-N₄ sites designed for durable oxygen reduction catalysis in acid media. *Angew. Chem., Int. Ed.* **2019**, *58*, 12469–12475.
- [145] Li, J. Z.; Chen, M. J.; Cullen, D. A.; Hwang, S.; Wang, M. Y.; Li, B. Y.; Liu, K. X.; Karakalos, S.; Lucero, M.; Zhang, H. G. et al. Atomically dispersed manganese catalysts for oxygen reduction in proton-exchange membrane fuel cells. *Nat. Catal.* **2018**, *1*, 935–945.
- [146] Zhong, W. F.; Sa, R.; Li, L. Y.; He, Y. J.; Li, L. Y.; Bi, J. H.; Zhuang, Z. Y.; Yu, Y.; Zou, Z. G. A covalent organic framework bearing single Ni sites as a synergistic photocatalyst for selective photoreduction of CO₂ to CO. *J. Am. Chem. Soc.* **2019**, *141*, 7615–7621.



- [147] Chen, Y. J.; Ji, S. F.; Sun, W. M.; Chen, W. X.; Dong, J. C.; Wen, J. F.; Zhang, J.; Li, Z.; Zheng, L. R.; Chen, C. et al. Discovering partially charged single-atom Pt for enhanced anti-markovnikov alkene hydrosilylation. *J. Am. Chem. Soc.* **2018**, *140*, 7407–7410.
- [148] Zhang, E. H.; Tao, L.; An, J. K.; Zhang, J. W.; Meng, L. Z.; Zheng, X. B.; Wang, Y.; Li, N.; Du, S. X.; Zhang, J. T. et al. Engineering the local atomic environments of indium single-atom catalysts for efficient electrochemical production of hydrogen peroxide. *Angew. Chem., Int. Ed.* **2022**, *61*, e202117347.
- [149] Dvořák, F.; Camellone, M. F.; Tovt, A.; Tran, N. D.; Negreiros, F. R.; Vorokhta, M.; Skála, T.; Matolínová, I.; Mysliveček, J.; Matolín, V. et al. Creating single-atom Pt-ceria catalysts by surface step decoration. *Nat. Commun.* **2016**, *7*, 10801.
- [150] Xie, P. F.; Pu, T. C.; Nie, A. M.; Hwang, S.; Purdy, S. C.; Yu, W. J.; Su, D.; Miller, J. T.; Wang, C. Nanoceria-supported single-atom platinum catalysts for direct methane conversion. *ACS Catal.* **2018**, *8*, 4044–4048.
- [151] Li, H. L.; Wang, L. B.; Dai, Y. Z.; Pu, Z. T.; Lao, Z. H.; Chen, Y. W.; Wang, M. L.; Zheng, X. S.; Zhu, J. F.; Zhang, W. H. et al. Synergistic interaction between neighbouring platinum monomers in CO₂ hydrogenation. *Nat. Nanotechnol.* **2018**, *13*, 411–417.
- [152] Lee, B. H.; Park, S.; Kim, M.; Sinha, A. K.; Lee, S. C.; Jung, E.; Chang, W. J.; Lee, K. S.; Kim, J. H.; Cho, S. P. et al. Reversible and cooperative photoactivation of single-atom Cu/TiO₂ photocatalysts. *Nat. Mater.* **2019**, *18*, 620–626.
- [153] Zhang, L. Z.; Jia, Y.; Gao, G. P.; Yan, X. C.; Chen, N.; Chen, J.; Soo, M. T.; Wood, B.; Yang, D. J.; Du, A. J. et al. Graphene defects trap atomic Ni species for hydrogen and oxygen evolution reactions. *Chem* **2018**, *4*, 285–297.
- [154] Huang, F.; Deng, Y. C.; Chen, Y. L.; Cai, X. B.; Peng, M.; Jia, Z. M.; Xie, J. L.; Xiao, D. Q.; Wen, X. D.; Wang, N. et al. Anchoring Cu₁ species over nanodiamond-graphene for semi-hydrogenation of acetylene. *Nat. Commun.* **2019**, *10*, 4431.
- [155] Zhang, J.; Wu, X.; Cheong, W. C.; Chen, W. X.; Lin, R.; Li, J.; Zheng, L. R.; Yan, W. S.; Gu, L.; Chen, C. et al. Cation vacancy stabilization of single-atomic-site Pt₁/Ni(OH)_x catalyst for diboration of alkynes and alkenes. *Nat. Commun.* **2018**, *9*, 1002.
- [156] Huang, F.; Deng, Y. C.; Chen, Y. L.; Cai, X. B.; Peng, M.; Jia, Z. M.; Ren, P. J.; Xiao, D. Q.; Wen, X. D.; Wang, N. et al. Atomically dispersed Pd on nanodiamond/graphene hybrid for selective hydrogenation of acetylene. *J. Am. Chem. Soc.* **2018**, *140*, 13142–13146.
- [157] Zhang, H. B.; Yu, L.; Chen, T.; Zhou, W.; Lou, X. W. D. Surface modulation of hierarchical MoS₂ nanosheets by Ni single atoms for enhanced electrocatalytic hydrogen evolution. *Adv. Funct. Mater.* **2018**, *28*, 1807086.
- [158] Jiang, K.; Liu, B. Y.; Luo, M.; Ning, S. C.; Peng, M.; Zhao, Y.; Lu, Y. R.; Chan, T. S.; De Groot, F. M. F.; Tan, Y. W. Single platinum atoms embedded in nanoporous cobalt selenide as electrocatalyst for accelerating hydrogen evolution reaction. *Nat. Commun.* **2019**, *10*, 1743.
- [159] He, X. H.; He, Q.; Deng, Y. C.; Peng, M.; Chen, H. Y.; Zhang, Y.; Yao, S. Y.; Zhang, M. T.; Xiao, D. Q.; Ma, D. et al. A versatile route to fabricate single atom catalysts with high chemoselectivity and regioselectivity in hydrogenation. *Nat. Commun.* **2019**, *10*, 3663.
- [160] Gao, C.; Chen, S. M.; Wang, Y.; Wang, J. W.; Zheng, X. S.; Zhu, J. F.; Song, L.; Zhang, W. K.; Xiong, Y. J. Heterogeneous single-atom catalyst for visible-light-driven high-turnover CO₂ reduction: The role of electron transfer. *Adv. Mater.* **2018**, *30*, 1704624.
- [161] Shao, X. Z.; Yang, X. F.; Xu, J. M.; Liu, S.; Miao, S.; Liu, X. Y.; Su, X.; Duan, H. M.; Huang, Y. Q.; Zhang, T. Iridium single-atom catalyst performing a quasi-homogeneous hydrogenation transformation of CO₂ to formate. *Chem* **2019**, *5*, 693–705.
- [162] He, T.; Chen, S. M.; Ni, B.; Gong, Y.; Wu, Z.; Song, L.; Gu, L.; Hu, W. P.; Wang, X. Zirconium-porphyrin-based metal-organic framework hollow nanotubes for immobilization of noble-metal single atoms. *Angew. Chem., Int. Ed.* **2018**, *57*, 3493–3498.
- [163] Yin, P. Q.; Yao, T.; Wu, Y. E.; Zheng, L. R.; Lin, Y.; Liu, W.; Ju, H. X.; Zhu, J. F.; Hong, X.; Deng, Z. X. et al. Single cobalt atoms with precise N-coordination as superior oxygen reduction reaction catalysts. *Angew. Chem., Int. Ed.* **2016**, *55*, 10800–10805.
- [164] Fei, H. L.; Dong, J. C.; Feng, Y. X.; Allen, C. S.; Wan, C. Z.; Voloskiy, B.; Li, M. F.; Zhao, Z. P.; Wang, Y. L.; Sun, H. T. et al. General synthesis and definitive structural identification of Mn₄C₄ single-atom catalysts with tunable electrocatalytic activities. *Nat. Catal.* **2018**, *1*, 63–72.
- [165] Sa, Y. J.; Seo, D. J.; Woo, J.; Lim, J. T.; Cheon, J. Y.; Yang, S. Y.; Lee, J. M.; Kang, D.; Shin, T. J.; Shin, H. S. et al. A general approach to preferential formation of active Fe-N_x sites in Fe-N/C electrocatalysts for efficient oxygen reduction reaction. *J. Am. Chem. Soc.* **2016**, *138*, 15046–15056.
- [166] Vilé, G.; Albani, D.; Nachtegaal, M.; Chen, Z. P.; Dontsova, D.; Antonietti, M.; López, N.; Pérez-Ramírez, J. A stable single-site palladium catalyst for hydrogenations. *Angew. Chem., Int. Ed.* **2015**, *54*, 11265–11269.
- [167] Li, X. G.; Bi, W. T.; Chen, M. L.; Sun, Y. X.; Ju, H. X.; Yan, W. S.; Zhu, J. F.; Wu, X. J.; Chu, W. S.; Wu, C. Z. et al. Exclusive NiN₄ sites realize near-unity CO selectivity for electrochemical CO₂ reduction. *J. Am. Chem. Soc.* **2017**, *139*, 14889–14892.
- [168] Chen, S. H.; Li, W. H.; Jiang, W. J.; Yang, J. R.; Zhu, J. X.; Wang, L. Q.; Ou, H. H.; Zhuang, Z. C.; Chen, M. Z.; Sun, X. H. et al. MOF encapsulating N-heterocyclic carbene-ligated copper single-atom site catalyst towards efficient methane electrosynthesis. *Angew. Chem., Int. Ed.* **2022**, *61*, e202114450.
- [169] Ye, L.; Duan, X. P.; Wu, S.; Wu, T. S.; Zhao, Y. X.; Robertson, A. W.; Chou, H. L.; Zheng, J. W.; Ayvalı, T.; Day, S. et al. Self-regeneration of Au/CeO₂ based catalysts with enhanced activity and ultra-stability for acetylene hydrochlorination. *Nat. Commun.* **2019**, *10*, 914.
- [170] Zhang, X. Y.; Sun, Z. C.; Wang, B.; Tang, Y.; Nguyen, L.; Li, Y. T.; Tao, F. F. C–C coupling on single-atom-based heterogeneous catalyst. *J. Am. Chem. Soc.* **2018**, *140*, 954–962.
- [171] Xin, P. Y.; Li, J.; Xiong, Y.; Wu, X.; Dong, J. C.; Chen, W. X.; Wang, Y.; Gu, L.; Luo, J.; Rong, H. P. et al. Revealing the active species for aerobic alcohol oxidation by using uniform supported palladium catalysts. *Angew. Chem., Int. Ed.* **2018**, *57*, 4642–4646.
- [172] Matsuba, J. C.; Yang, V. N.; Christopher, P. Isolated metal active site concentration and stability control catalytic CO₂ reduction selectivity. *J. Am. Chem. Soc.* **2015**, *137*, 3076–3084.
- [173] Millet, M. M.; Algara-Siller, G.; Wrabetz, S.; Mazheika, A.; Girgsdies, F.; Teschner, D.; Seitz, F.; Tarasov, A.; Levchenko, S. V.; Schlögl, R. et al. Ni single atom catalysts for CO₂ activation. *J. Am. Chem. Soc.* **2019**, *141*, 2451–2461.
- [174] Lin, L. L.; Zhou, W.; Gao, R.; Yao, S. Y.; Zhang, X.; Xu, W. Q.; Zheng, S. J.; Jiang, Z.; Yu, Q. L.; Li, Y. W. et al. Low-temperature hydrogen production from water and methanol using Pt/α-MoC catalysts. *Nature* **2017**, *544*, 80–83.
- [175] Lin, L. L.; Yao, S. Y.; Gao, R.; Liang, X.; Yu, Q. L.; Deng, Y. C.; Liu, J. J.; Peng, M.; Jiang, Z.; Li, S. W. et al. A highly CO-tolerant atomically dispersed Pt catalyst for chemoselective hydrogenation. *Nat. Nanotechnol.* **2019**, *14*, 354–361.
- [176] Li, S. W.; Liu, J. J.; Yin, Z.; Ren, P. J.; Lin, L. L.; Gong, Y.; Yang, C.; Zheng, X. S.; Cao, R. C.; Yao, S. Y. et al. Impact of the coordination environment on atomically dispersed Pt catalysts for oxygen reduction reaction. *ACS Catal.* **2020**, *10*, 907–913.
- [177] DeRita, L.; Dai, S.; Lopez-Zepeda, K.; Pham, N.; Graham, G. W.; Pan, X. Q.; Christopher, P. Catalyst architecture for stable single atom dispersion enables site-specific spectroscopic and reactivity measurements of CO adsorbed to Pt atoms, oxidized Pt clusters, and metallic Pt clusters on TiO₂. *J. Am. Chem. Soc.* **2017**, *139*, 14150–14165.
- [178] Jiao, L.; Regalbuto, J. R. The synthesis of highly dispersed noble and base metals on silica via strong electrostatic adsorption: I. Amorphous silica. *J. Catal.* **2008**, *260*, 329–341.
- [179] Yan, H.; Cheng, H.; Yi, H.; Lin, Y.; Yao, T.; Wang, C. L.; Li, J. J.; Wei, S. Q.; Lu, J. L. Single-atom Pd₁/graphene catalyst achieved by atomic layer deposition: Remarkable performance in selective hydrogenation of 1,3-butadiene. *J. Am. Chem. Soc.* **2015**, *137*, 10484–10487.
- [180] Cao, Y. J.; Chen, S.; Luo, Q. Q.; Yan, H.; Lin, Y.; Liu, W.; Cao, L. L.; Lu, J. L.; Yang, J. L.; Yao, T. et al. Atomic-level insight into

- optimizing the hydrogen evolution pathway over a Co₁-N₄ single-site photocatalyst. *Angew. Chem., Int. Ed.* **2017**, *56*, 12191–12196.
- [181] Zhang, L.; Banis, M. N.; Sun, X. L. Single-atom catalysts by the atomic layer deposition technique. *Natl. Sci. Rev.* **2018**, *5*, 628–630.
- [182] Cheng, N. C.; Stambula, S.; Wang, D.; Banis, M. N.; Liu, J.; Riese, A.; Xiao, B. W.; Li, R. Y.; Sham, T. K.; Liu, L. M. et al. Platinum single-atom and cluster catalysis of the hydrogen evolution reaction. *Nat. Commun.* **2016**, *7*, 13638.
- [183] Han, G. F.; Li, F.; Rykov, A. I.; Im, Y. K.; Yu, S. Y.; Jeon, J. P.; Kim, S. J.; Zhou, W. H.; Ge, R. L.; Ao, Z. M. et al. Abrading bulk metal into single atoms. *Nat. Nanotechnol.* **2022**, *17*, 403–407.
- [184] Qu, Y. T.; Li, Z. J.; Chen, W. X.; Lin, Y.; Yuan, T. W.; Yang, Z. K.; Zhao, C. M.; Wang, J.; Zhao, C.; Wang, X. et al. Direct transformation of bulk copper into copper single sites via emitting and trapping of atoms. *Nat. Catal.* **2018**, *1*, 781–786.
- [185] Yang, Z. K.; Chen, B. X.; Chen, W. X.; Qu, Y. T.; Zhou, F. Y.; Zhao, C. M.; Xu, Q.; Zhang, Q. H.; Duan, X. Z.; Wu, Y. E. Directly transforming copper (I) oxide bulk into isolated single-atom copper sites catalyst through gas-transport approach. *Nat. Commun.* **2019**, *10*, 3734.
- [186] Sun, T. T.; Zhao, S.; Chen, W. X.; Zhai, D.; Dong, J. C.; Wang, Y.; Zhang, S. L.; Han, A. J.; Gu, L.; Yu, R. et al. Single-atomic cobalt sites embedded in hierarchically ordered porous nitrogen-doped carbon as a superior bifunctional electrocatalyst. *Proc. Natl. Acad. Sci. USA* **2018**, *115*, 12692–12697.
- [187] Han, Y. H.; Wang, Y. G.; Chen, W. X.; Xu, R. R.; Zheng, L. R.; Zhang, J.; Luo, J.; Shen, R. A.; Zhu, Y. Q.; Cheong, W. C. et al. Hollow N-doped carbon spheres with isolated cobalt single atomic sites: Superior electrocatalysts for oxygen reduction. *J. Am. Chem. Soc.* **2017**, *139*, 17269–17272.
- [188] Zhang, L. Z.; Jia, Y.; Liu, H. L.; Zhuang, L. Z.; Yan, X. C.; Lang, C. G.; Wang, X.; Yang, D. J.; Huang, K. K.; Feng, S. H. et al. Charge polarization from atomic metals on adjacent graphitic layers for enhancing the hydrogen evolution reaction. *Angew. Chem., Int. Ed.* **2019**, *58*, 9404–9408.
- [189] Fan, L. L.; Liu, P. F.; Yan, X. C.; Gu, L.; Yang, Z. Z.; Yang, H. G.; Qiu, S. L.; Yao, X. D. Atomically isolated nickel species anchored on graphitized carbon for efficient hydrogen evolution electrocatalysis. *Nat. Commun.* **2016**, *7*, 10667.
- [190] Ge, X. X.; Zhou, P.; Zhang, Q. H.; Xia, Z. H.; Chen, S. L.; Gao, P.; Zhang, Z.; Gu, L.; Guo, S. J. Palladium single atoms on TiO₂ as a photocatalytic sensing platform for analyzing the organophosphorus pesticide chlorpyrifos. *Angew. Chem., Int. Ed.* **2020**, *59*, 232–236.
- [191] Liu, P. X.; Zhao, Y.; Qin, R. X.; Mo, S. G.; Chen, G. X.; Gu, L.; Chevrier, D. M.; Zhang, P.; Guo, Q.; Zang, D. D. et al. Photochemical route for synthesizing atomically dispersed palladium catalysts. *Science* **2016**, *352*, 797–800.
- [192] Wei, H. H.; Huang, K.; Wang, D.; Zhang, R. Y.; Ge, B. H.; Ma, J. Y.; Wen, B.; Zhang, S.; Li, Q. Y.; Lei, M. et al. Iced photochemical reduction to synthesize atomically dispersed metals by suppressing nanocrystal growth. *Nat. Commun.* **2017**, *8*, 1490.
- [193] Li, Y. G.; Hao, J. C.; Song, H.; Zhang, F. Y.; Bai, X. H.; Meng, X. G.; Zhang, H. Y.; Wang, S. F.; Hu, Y.; Ye, J. H. Selective light absorber-assisted single nickel atom catalysts for ambient sunlight-driven CO₂ methanation. *Nat. Commun.* **2019**, *10*, 2359.
- [194] Yao, Y. G.; Huang, Z. N.; Xie, P. F.; Wu, L. P.; Ma, L.; Li, T. Y.; Pang, Z. Q.; Jiao, M. L.; Liang, Z.; Gao, J. L. et al. High temperature shockwave stabilized single atoms. *Nat. Nanotechnol.* **2019**, *14*, 851–857.
- [195] Deng, D. H.; Chen, X. Q.; Yu, L.; Wu, X.; Liu, Q. F.; Liu, Y.; Yang, H. X.; Tian, H. F.; Hu, Y. F.; Du, P. P. et al. A single iron site confined in a graphene matrix for the catalytic oxidation of benzene at room temperature. *Sci. Adv.* **2015**, *1*, e1500462.
- [196] Cui, X. J.; Xiao, J. P.; Wu, Y. H.; Du, P. P.; Si, R.; Yang, H. X.; Tian, H. F.; Li, J. Q.; Zhang, W. H.; Deng, D. H. et al. A graphene composite material with single cobalt active sites: A highly efficient counter electrode for dye-sensitized solar cells. *Angew. Chem., Int. Ed.* **2016**, *55*, 6708–6712.
- [197] Ding, S. P.; Guo, Y. L.; Hulsey, M. J.; Zhang, B.; Asakura, H.; Liu, L. M.; Han, Y.; Gao, M.; Hasegawa, J. Y.; Qiao, B. T. et al. Electrostatic stabilization of single-atom catalysts by ionic liquids. *Chem* **2019**, *5*, 3207–3219.
- [198] Chen, Y. J.; Ji, S. F.; Sun, W. M.; Lei, Y. P.; Wang, Q. C.; Li, A.; Chen, W. X.; Zhou, G.; Zhang, Z. D.; Wang, Y. et al. Engineering the atomic interface with single platinum atoms for enhanced photocatalytic hydrogen production. *Angew. Chem., Int. Ed.* **2020**, *59*, 1295–1301.
- [199] Yang, J. R.; Li, W. H.; Xu, K. N.; Tan, S. D.; Wang, D. S.; Li, Y. D. Regulating the tip effect on single-atom and cluster catalysts: Forming reversible oxygen species with high efficiency in chlorine evolution reaction. *Angew. Chem., Int. Ed.* **2022**, *61*, e202200366.
- [200] Zheng, X. B.; Yang, J. R.; Li, P.; Jiang, Z. L.; Zhu, P.; Wang, Q. S.; Wu, J. B.; Zhang, E. H.; Sun, W. P.; Dou, S. X. et al. Dual-atom support boosts nickel-catalyzed urea electrooxidation. *Angew. Chem., Int. Ed.* **2023**, *62*, e202217449.
- [201] Zhao, C. X.; Liu, J. N.; Wang, J.; Wang, C. D.; Guo, X.; Li, X. Y.; Chen, X.; Song, L.; Li, B. Q.; Zhang, Q. A clicking confinement strategy to fabricate transition metal single-atom sites for bifunctional oxygen electrocatalysis. *Sci. Adv.* **2022**, *8*, eabn5091.
- [202] Chen, Z. P.; Mitchell, S.; Vorobyeva, E.; Leary, R. K.; Hauert, R.; Furnival, T.; Ramasse, Q. M.; Thomas, J. M.; Midgley, P. A.; Dontsova, D. et al. Stabilization of single metal atoms on graphitic carbon nitride. *Adv. Funct. Mater.* **2017**, *27*, 1605785.
- [203] Chen, Y. J.; Ji, S. F.; Zhao, S.; Chen, W. X.; Dong, J. C.; Cheong, W. C.; Shen, R. A.; Wen, X. D.; Zheng, L. R.; Rykov, A. I. et al. Enhanced oxygen reduction with single-atomic-site iron catalysts for a zinc-air battery and hydrogen-air fuel cell. *Nat. Commun.* **2018**, *9*, 5422.
- [204] Fang, X. Z.; Shang, Q. C.; Wang, Y.; Jiao, L.; Yao, T.; Li, Y. F.; Zhang, Q.; Luo, Y.; Jiang, H. L. Single Pt atoms confined into a metal-organic framework for efficient photocatalysis. *Adv. Mater.* **2018**, *30*, 1705112.
- [205] Liu, Q. T.; Liu, X. F.; Zheng, L. R.; Shui, J. L. The solid-phase synthesis of an Fe-N-C electrocatalyst for high-power proton-exchange membrane fuel cells. *Angew. Chem., Int. Ed.* **2018**, *57*, 1204–1208.
- [206] Peng, W.; Han, J. H.; Lu, Y. R.; Luo, M.; Chan, T. S.; Peng, M.; Tan, Y. W. A general strategy for engineering single-metal sites on 3D porous N, P Co-doped Ti₃C₂T_x MXene. *ACS Nano* **2022**, *16*, 4116–4125.
- [207] George, S. M. Atomic layer deposition: An overview. *Chem. Rev.* **2010**, *110*, 111–131.
- [208] Lu, J. L.; Elam, J. W.; Stair, P. C. Synthesis and stabilization of supported metal catalysts by atomic layer deposition. *Acc. Chem. Res.* **2013**, *46*, 1806–1815.
- [209] Puurunen, R. L. A short history of atomic layer deposition: Tuomo Suntola's atomic layer epitaxy. *Chem. Vap. Deposit.* **2014**, *20*, 332–344.
- [210] Fonseca, J.; Lu, J. L. Single-atom catalysts designed and prepared by the atomic layer deposition technique. *ACS Catal.* **2021**, *11*, 7018–7059.
- [211] Cheng, N. C.; Sun, X. L. Single atom catalyst by atomic layer deposition technique. *Chin. J. Catal.* **2017**, *38*, 1508–1514.
- [212] Xia, W.; Mahmood, A.; Liang, Z. B.; Zou, R. Q.; Guo, S. J. Earth-abundant nanomaterials for oxygen reduction. *Angew. Chem., Int. Ed.* **2016**, *55*, 2650–2676.
- [213] Zheng, X. B.; Li, B. B.; Wang, Q. S.; Wang, D. S.; Li, Y. D. Emerging low-nuclearity supported metal catalysts with atomic level precision for efficient heterogeneous catalysis. *Nano Res.* **2022**, *15*, 7806–7839.
- [214] Du, L.; Prabhakaran, V.; Xie, X. H.; Park, S.; Wang, Y.; Shao, Y. Y. Low-PGM and PGM-free catalysts for proton exchange membrane fuel cells: Stability challenges and material solutions. *Adv. Mater.* **2021**, *33*, 1908232.
- [215] Wang, X. X.; Swihart, M. T.; Wu, G. Achievements, challenges and perspectives on cathode catalysts in proton exchange membrane fuel cells for transportation. *Nat. Catal.* **2019**, *2*, 578–589.
- [216] Wu, D. S.; Kusada, K.; Yamamoto, T.; Toriyama, T.; Matsumura, S.; Kawaguchi, S.; Kubota, Y.; Kitagawa, H. Platinum-group-metal high-entropy-alloy nanoparticles. *J. Am. Chem. Soc.* **2020**, *142*,

- 13833–13838.
- [217] Yao, Y. G.; Huang, Z. N.; Xie, P. F.; Lacey, S. D.; Jacob, R. J.; Xie, H.; Chen, F. J.; Nie, A. M.; Pu, T. C.; Rehwoldt, M. et al. Carbothermal shock synthesis of high-entropy-alloy nanoparticles. *Science* **2018**, *359*, 1489–1494.
- [218] Yao, Y. G.; Dong, Q.; Brozena, A.; Luo, J.; Miao, J. W.; Chi, M. F.; Wang, C.; Kevrekidis, I. G.; Ren, Z. J.; Greeley, J. et al. High-entropy nanoparticles: Synthesis-structure-property relationships and data-driven discovery. *Science* **2022**, *376*, eabn3103.
- [219] Li, T. Y.; Yao, Y. G.; Huang, Z. N.; Xie, P. F.; Liu, Z. Y.; Yang, M. H.; Gao, J. L.; Zeng, K. Z.; Brozena, A. H.; Pastel, G. et al. Denary oxide nanoparticles as highly stable catalysts for methane combustion. *Nat. Catal.* **2021**, *4*, 62–70.
- [220] Stranks, S. D.; Eperon, G. E.; Grancini, G.; Menelaou, C.; Alcocer, M. J. P.; Leijtens, T.; Herz, L. M.; Petrozza, A.; Snaith, H. J. Electron-hole diffusion lengths exceeding 1 micrometer in an organometal trihalide perovskite absorber. *Science* **2013**, *342*, 341–344.
- [221] Chen, X. B.; Mao, S. S. Titanium dioxide nanomaterials: Synthesis, properties, modifications, and applications. *Chem. Rev.* **2007**, *107*, 2891–2959.
- [222] Poizot, P.; Laruelle, S.; Grugueon, S.; Dupont, L.; Tarascon, J. M. Nano-sized transition-metal oxides as negative-electrode materials for lithium-ion batteries. *Nature* **2000**, *407*, 496–499.
- [223] Kudo, A.; Miseki, Y. Heterogeneous photocatalyst materials for water splitting. *Chem. Soc. Rev.* **2009**, *38*, 253–278.
- [224] Zou, X. X.; Zhang, Y. Noble metal-free hydrogen evolution catalysts for water splitting. *Chem. Soc. Rev.* **2015**, *44*, 5148–5180.
- [225] Wang, L. G.; Duan, X. X.; Liu, X. J.; Gu, J.; Si, R.; Qiu, Y.; Qiu, Y. M.; Shi, D. E.; Chen, F. H.; Sun, X. M. et al. Atomically dispersed Mo supported on metallic Co₉S₈ nanoflakes as an advanced noble-metal-free bifunctional water splitting catalyst working in universal pH conditions. *Adv. Energy Mater.* **2020**, *10*, 1903137.
- [226] Choi, W.; Choudhary, N.; Han, G. H.; Park, J.; Akinwande, D.; Lee, Y. H. Recent development of two-dimensional transition metal dichalcogenides and their applications. *Mater. Today* **2017**, *20*, 116–130.
- [227] Hwang, J. Y.; Myung, S. T.; Sun, Y. K. Sodium-ion batteries: Present and future. *Chem. Soc. Rev.* **2017**, *46*, 3529–3614.
- [228] Wang, L. G.; Xia, L.; Wu, Y. J.; Tian, Y. Zr-doped β-In₂S₃ ultrathin nanoflakes as photoanodes: Enhanced visible-light-driven photoelectrochemical water splitting. *ACS Sustainable Chem. Eng.* **2016**, *4*, 2606–2614.
- [229] Martinez, U.; Babu, S. K.; Holby, E. F.; Chung, H. T.; Yin, X.; Zelenay, P. Progress in the development of Fe-based PGM-free electrocatalysts for the oxygen reduction reaction. *Adv. Mater.* **2019**, *31*, 1806545.
- [230] Thompson, S. T.; Papageorgopoulos, D. Platinum group metal-free catalysts boost cost competitiveness of fuel cell vehicles. *Nat. Catal.* **2019**, *2*, 558–561.
- [231] Ni, W. Y.; Wang, T.; Héroguel, F.; Krammer, A.; Lee, S.; Yao, L.; Schüler, A.; Luterbacher, J. S.; Yan, Y. S.; Hu, X. L. An efficient nickel hydrogen oxidation catalyst for hydroxide exchange membrane fuel cells. *Nat. Mater.* **2022**, *21*, 804–810.
- [232] Ye, K.; Cao, A.; Shao, J. Q.; Wang, G.; Si, R.; Ta, N.; Xiao, J. P.; Wang, G. X. Synergy effects on Sn-Cu alloy catalyst for efficient CO₂ electroreduction to formate with high mass activity. *Sci. Bull.* **2020**, *65*, 711–719.
- [233] He, J. Y.; Liu, W. H.; Wang, H.; Wu, Y.; Liu, X. J.; Nieh, T. G.; Lu, Z. P. Effects of Al addition on structural evolution and tensile properties of the FeCoNiCrMn high-entropy alloy system. *Acta Mater.* **2014**, *62*, 105–113.
- [234] Jiao, J. Q.; Lin, R.; Liu, S. J.; Cheong, W. C.; Zhang, C.; Chen, Z.; Pan, Y.; Tang, J. G.; Wu, K. L.; Hung, S. F. et al. Copper atom-pair catalyst anchored on alloy nanowires for selective and efficient electrochemical reduction of CO₂. *Nat. Chem.* **2019**, *11*, 222–228.
- [235] Chen, Y. J.; Pei, J. J.; Chen, Z.; Li, A.; Ji, S. F.; Rong, H. P.; Xu, Q.; Wang, T.; Zhang, A. J.; Tang, H. L. et al. Pt atomic layers with tensile strain and rich defects boost ethanol electrooxidation. *Nano Lett.* **2022**, *22*, 7563–7571.
- [236] Bu, L. Z.; Zhang, N.; Guo, S. J.; Zhang, X.; Li, J.; Yao, J. L.; Wu, T.; Lu, G.; Ma, J. Y.; Su, D. et al. Biaxially strained PtPb/Pt core/shell nanoplate boosts oxygen reduction catalysis. *Science* **2016**, *354*, 1410–1414.
- [237] Huang, X. Q.; Zhao, Z. P.; Cao, L.; Chen, Y.; Zhu, E. B.; Lin, Z. Y.; Li, M. F.; Yan, A. M.; Zettl, A.; Wang, Y. M. et al. High-performance transition metal-doped Pt₃Ni octahedra for oxygen reduction reaction. *Science* **2015**, *348*, 1230–1234.
- [238] Luo, M. C.; Zhao, Z. L.; Zhang, Y. L.; Sun, Y. J.; Xing, Y.; Lv, F.; Yang, Y.; Zhang, X.; Hwang, S.; Qin, Y. N. et al. PdMo bimettallene for oxygen reduction catalysis. *Nature* **2019**, *574*, 81–85.
- [239] Tian, X. L.; Zhao, X.; Su, Y. Q.; Wang, L. J.; Wang, H. M.; Dang, D.; Chi, B.; Liu, H. F.; Hensen, E. J. M.; Lou, X. W. et al. Engineering bunched Pt-Ni alloy nanocages for efficient oxygen reduction in practical fuel cells. *Science* **2019**, *366*, 850–856.
- [240] Janssonius, R. P.; Reid, L. M.; Virca, C. N.; Berlinguet, C. P. Strain engineering electrocatalysts for selective CO₂ Reduction. *ACS Energy Lett.* **2019**, *4*, 980–986.
- [241] Liu, D. Y.; Zeng, Q.; Liu, H.; Hu, C. Q.; Chen, D.; Xu, L.; Yang, J. Combining the core-shell construction with an alloying effect for high efficiency ethanol electrooxidation. *Cell Rep. Phys. Sci.* **2021**, *2*, 100357.
- [242] Zhou, Y.; Gu, Q. F.; Yin, K.; Li, Y. J.; Tao, L.; Tan, H.; Yang, Y.; Guo, S. J. Engineering e_g orbital occupancy of Pt with Au alloying enables reversible Li-O₂ batteries. *Angew. Chem., Int. Ed.* **2022**, *61*, e202201416.
- [243] Zheng, X. B.; Li, P.; Dou, S. X.; Sun, W. P.; Pan, H. G.; Wang, D. S.; Li, Y. D. Non-carbon-supported single-atom site catalysts for electrocatalysis. *Energy Environ. Sci.* **2021**, *14*, 2809–2858.
- [244] Tang, H. L.; Su, Y.; Zhang, B. S.; Lee, A. F.; Isaacs, M. A.; Wilson, K.; Li, L.; Ren, Y. G.; Huang, J. H.; Haruta, M. et al. Classical strong metal-support interactions between gold nanoparticles and titanium dioxide. *Sci. Adv.* **2017**, *3*, e1700231.
- [245] Dong, J. H.; Fu, Q.; Li, H. B.; Xiao, J. P.; Yang, B.; Zhang, B. S.; Bai, Y. X.; Song, T. Y.; Zhang, R. K.; Gao, L. J. et al. Reaction-induced strong metal-support interactions between metals and inert boron nitride nanosheets. *J. Am. Chem. Soc.* **2020**, *142*, 17167–17174.
- [246] Yu, J. S.; Kang, S.; Yoon, S. B.; Chai, G. Fabrication of ordered uniform porous carbon networks and their application to a catalyst supporter. *J. Am. Chem. Soc.* **2002**, *124*, 9382–9383.
- [247] Chai, G. S.; Shin, I. S.; Yu, J. S. Synthesis of ordered, uniform, macroporous carbons with mesoporous walls templated by aggregates of polystyrene spheres and silica particles for use as catalyst supports in direct methanol fuel cells. *Adv. Mater.* **2004**, *16*, 2057–2061.
- [248] Choi, W. C.; Woo, S. I.; Jeon, M. K.; Sohn, J. M.; Kim, M. R.; Jeon, H. J. Platinum nanoclusters studded in the microporous nanowalls of ordered mesoporous carbon. *Adv. Mater.* **2005**, *17*, 446–451.
- [249] Han, S.; Yun, Y.; Park, K. W.; Sung, Y. E.; Hyeon, T. Simple solid-phase synthesis of hollow graphitic nanoparticles and their application to direct methanol fuel cell electrodes. *Adv. Mater.* **2003**, *15*, 1922–1925.
- [250] Luo, Z. X.; Zhao, G. Q.; Pan, H. G.; Sun, W. P. Strong metal-support interaction in heterogeneous catalysts. *Adv. Energy Mater.* **2022**, *12*, 2201395.
- [251] Yao, S. Y.; Zhang, X.; Zhou, W.; Gao, R.; Xu, W. Q.; Ye, Y. F.; Lin, L. L.; Wen, X. D.; Liu, P.; Chen, B. B. et al. Atomic-layered Au clusters on α-MoC as catalysts for the low-temperature water-gas shift reaction. *Science* **2017**, *357*, 389–393.
- [252] Van Deelen, T. W.; Mejía, C. H.; De Jong, K. P. Control of metal-support interactions in heterogeneous catalysts to enhance activity and selectivity. *Nat. Catal.* **2019**, *2*, 955–970.
- [253] Yang, J. R.; Li, W. H.; Wang, D. S.; Li, Y. D. Electronic metal-support interaction of single-atom catalysts and applications in electrocatalysis. *Adv. Mater.* **2020**, *32*, 2003300.
- [254] Li, W. H.; Yang, J. R.; Wang, D. S. Long-range interactions in diatomic catalysts boosting electrocatalysis. *Angew. Chem., Int. Ed.* **2022**, *61*, e202213318.

- [255] Wan, J. W.; Chen, W. X.; Jia, C. Y.; Zheng, L. R.; Dong, J. C.; Zheng, X. S.; Wang, Y.; Yan, W. S.; Chen, C.; Peng, Q. et al. Defect effects on TiO₂ nanosheets: Stabilizing single atomic site Au and promoting catalytic properties. *Adv. Mater.* **2018**, *30*, 1705369.
- [256] Zhang, J. Q.; Zhao, Y. F.; Guo, X.; Chen, C.; Dong, C. L.; Liu, R. S.; Han, C. P.; Li, Y. D.; Gogotsi, Y.; Wang, G. X. Single platinum atoms immobilized on an MXene as an efficient catalyst for the hydrogen evolution reaction. *Nat. Catal.* **2018**, *1*, 985–992.
- [257] Zheng, X. B.; Cui, P. X.; Qian, Y. M.; Zhao, G. Q.; Zheng, X. S.; Xu, X.; Cheng, Z. X.; Liu, Y. Y.; Dou, S. X.; Sun, W. P. Multifunctional active-center-transferable platinum/lithium cobalt oxide heterostructured electrocatalysts towards superior water splitting. *Angew. Chem., Int. Ed.* **2020**, *59*, 14533–14540.
- [258] Zhang, Z. D.; Zhou, M.; Chen, Y. J.; Liu, S. J.; Wang, H. F.; Zhang, J.; Ji, S. F.; Wang, D. S.; Li, Y. D. Pd single-atom monolithic catalyst: Functional 3D structure and unique chemical selectivity in hydrogenation reaction. *Sci. China Mater.* **2021**, *64*, 1919–1929.
- [259] Wang, L. G.; Liu, H.; Zhuang, J. H.; Wang, D. S. Small-scale big science: From nano- to atomically dispersed catalytic materials. *Small Sci.* **2022**, *2*, 2200036.
- [260] Yang, X. F.; Wang, A. Q.; Qiao, B. T.; Li, J.; Liu, J. Y.; Zhang, T. Single-atom catalysts: A new frontier in heterogeneous catalysis. *Acc. Chem. Res.* **2013**, *46*, 1740–1748.
- [261] Wang, H. W.; Gu, X. K.; Zheng, X. S.; Pan, H. B.; Zhu, J. F.; Chen, S.; Cao, L. N.; Li, W. X.; Lu, J. L. Disentangling the size-dependent geometric and electronic effects of palladium nanocatalysts beyond selectivity. *Sci. Adv.* **2019**, *5*, eaat6413.
- [262] Wei, S. J.; Li, A.; Liu, J. C.; Li, Z.; Chen, W. X.; Gong, Y.; Zhang, Q. H.; Cheong, W. C.; Wang, Y.; Zheng, L. R. et al. Direct observation of noble metal nanoparticles transforming to thermally stable single atoms. *Nat. Nanotechnol.* **2018**, *13*, 856–861.
- [263] Li, W.; Wang, D. D.; Zhang, Y. Q.; Tao, L.; Wang, T. H.; Zou, Y. Q.; Wang, Y. Y.; Chen, R.; Wang, S. Y. Defect engineering for fuel-cell electrocatalysts. *Adv. Mater.* **2020**, *32*, 1907879.
- [264] Zhang, Y. Q.; Tao, L.; Xie, C.; Wang, D. D.; Zou, Y. Q.; Chen, R.; Wang, Y. Y.; Jia, C. K.; Wang, S. Y. Defect engineering on electrode materials for rechargeable batteries. *Adv. Mater.* **2020**, *32*, 1905923.
- [265] Zhang, B.; Hou, J. G.; Wu, Y. Z.; Cao, S. Y.; Li, Z. W.; Nie, X. W.; Gao, Z. M.; Sun, L. C. Tailoring active sites in mesoporous defect-rich NC/V_o-WON heterostructure array for superior electrocatalytic hydrogen evolution. *Adv. Energy Mater.* **2019**, *9*, 1803693.
- [266] Zhang, B. W.; Qi, Z. Y.; Wu, Z. S.; Lui, Y. H.; Kim, T. H.; Tang, X. H.; Zhou, L.; Huang, W. Y.; Hu, S. Defect-rich 2D material networks for advanced oxygen evolution catalysts. *ACS Energy Lett.* **2019**, *4*, 328–336.
- [267] Zhu, J. W.; Huang, Y. P.; Mei, W. C.; Zhao, C. Y.; Zhang, C. T.; Zhang, J.; Amiu, I. S.; Mu, S. C. Effects of intrinsic pentagon defects on electrochemical reactivity of carbon nanomaterials. *Angew. Chem., Int. Ed.* **2019**, *58*, 3859–3864.
- [268] Yang, H. G.; Sun, C. H.; Qiao, S. Z.; Zou, J.; Liu, G.; Smith, S. C.; Cheng, H. M.; Lu, G. Q. Anatase TiO₂ single crystals with a large percentage of reactive facets. *Nature* **2008**, *453*, 638–641.
- [269] Li, R. G.; Zhang, F. X.; Wang, D.; Yang, J. X.; Li, M. R.; Zhu, J.; Zhou, X.; Han, H. X.; Li, C. Spatial separation of photogenerated electrons and holes among {010} and {110} crystal facets of BiVO₄. *Nat. Commun.* **2013**, *4*, 1432.
- [270] Chen, R. T.; Pang, S.; An, H. Y.; Zhu, J.; Ye, S.; Gao, Y. Y.; Fan, F. T.; Li, C. Charge separation via asymmetric illumination in photocatalytic Cu₂O particles. *Nat. Energy* **2018**, *3*, 655–663.
- [271] Takata, T.; Jiang, J. Z.; Sakata, Y.; Nakabayashi, M.; Shibata, N.; Nandal, V.; Seki, K.; Hisatomi, T.; Domen, K. Photocatalytic water splitting with a quantum efficiency of almost unity. *Nature* **2020**, *581*, 411–414.
- [272] Li, M. F.; Zhao, Z. P.; Cheng, T.; Fortunelli, A.; Chen, C. Y.; Yu, R.; Zhang, Q. H.; Gu, L.; Merinov, B. V.; Lin, Z. Y. et al. Ultrafine jagged platinum nanowires enable ultrahigh mass activity for the oxygen reduction reaction. *Science* **2016**, *354*, 1414–1419.
- [273] Liu, J. W.; You, F. T.; He, B. W.; Wu, Y. L.; Wang, D. D.; Zhou, W. Q.; Qian, C.; Yang, G. B.; Liu, G. F.; Wang, H. et al. Directing the architecture of surface-clean Cu₂O for CO electroreduction. *J. Am. Chem. Soc.* **2022**, *144*, 12410–12420.
- [274] Zou, Z. H.; Wang, T. T.; Zhao, X. H.; Jiang, W. J.; Pan, H. R.; Gao, D. Q.; Xu, C. L. Expediting *in-situ* electrochemical activation of two-dimensional metal-organic frameworks for enhanced OER intrinsic activity by iron incorporation. *ACS Catal.* **2019**, *9*, 7356–7364.
- [275] Zhao, Y. F.; Kumar, P. V.; Tan, X.; Lu, X. X.; Zhu, X. F.; Jiang, J. J.; Pan, J.; Xi, S. B.; Yang, H. Y.; Ma, Z. P. et al. Modulating Pt-O-Pt atomic clusters with isolated cobalt atoms for enhanced hydrogen evolution catalysis. *Nat. Commun.* **2022**, *13*, 2430.
- [276] Pei, Z. H.; Lu, X. F.; Zhang, H. B.; Li, Y. X.; Luan, D. Y.; Lou, X. W. Highly efficient electrocatalytic oxygen evolution over atomically dispersed synergistic Ni/Co dual sites. *Angew. Chem., Int. Ed.* **2022**, *61*, e202207537.
- [277] Yan, Y.; Yin, Y. X.; Guo, Y. G.; Wan, L. J. A sandwich-like hierarchically porous carbon/graphene composite as a high-performance anode material for sodium-ion batteries. *Adv. Energy Mater.* **2014**, *4*, 1301584.
- [278] Wang, J.; Liu, J. L.; Chao, D. L.; Yan, J. X.; Lin, J. Y.; Shen, Z. X. Self-assembly of honeycomb-like MoS₂ nanoarchitectures anchored into graphene foam for enhanced lithium-ion storage. *Adv. Mater.* **2014**, *26*, 7162–7169.
- [279] Zhang, Z. B.; Wang, C. C.; Zakaria, R.; Ying, J. Y. Role of particle size in nanocrystalline TiO₂-based photocatalysts. *J. Phys. Chem. B* **1998**, *102*, 10871–10878.
- [280] Chen, C.; Kang, Y. J.; Huo, Z. Y.; Zhu, Z. W.; Huang, W. Y.; Xin, H. L.; Snyder, J. D.; Li, D. G.; Herron, J. A.; Mavrikakis, M. et al. Highly crystalline multimetallic nanoframes with three-dimensional electrocatalytic surfaces. *Science* **2014**, *343*, 1339–1343.
- [281] Vogt, C.; Weckhuysen, B. M. The concept of active site in heterogeneous catalysis. *Nat. Rev. Chem.* **2022**, *6*, 89–111.
- [282] Babucci, M.; Guntida, A.; Gates, B. C. Atomically dispersed metals on well-defined supports including zeolites and metal-organic frameworks: Structure, bonding, reactivity, and catalysis. *Chem. Rev.* **2020**, *120*, 11956–11985.
- [283] Montini, T.; Melchionna, M.; Monai, M.; Fornasiero, P. Fundamentals and catalytic applications of CeO₂-based materials. *Chem. Rev.* **2016**, *116*, 5987–6041.
- [284] Natinsky, B. S.; Liu, C. Two are better than one. *Nat. Chem.* **2019**, *11*, 200–201.
- [285] Zhu, P.; Xiong, X.; Wang, D. S. Regulations of active moiety in single atom catalysts for electrochemical hydrogen evolution reaction. *Nano Res.* **2022**, *15*, 5792–5815.
- [286] Li, R. Z.; Wang, D. S. Understanding the structure-performance relationship of active sites at atomic scale. *Nano Res.* **2022**, *15*, 6888–6923.
- [287] Zhao, J. J.; Fu, C. H.; Ye, K.; Liang, Z.; Jiang, F. L.; Shen, S. Y.; Zhao, X. R.; Ma, L.; Shadike, Z.; Wang, X. M. et al. Manipulating the oxygen reduction reaction pathway on Pt-coordinated motifs. *Nat. Commun.* **2022**, *13*, 685.
- [288] Pan, Y.; Chen, Y. J.; Wu, K. L.; Chen, Z.; Liu, S. J.; Cao, X.; Cheong, W. C.; Meng, T.; Luo, J.; Zheng, L. R. et al. Regulating the coordination structure of single-atom Fe-N_xC_y catalytic sites for benzene oxidation. *Nat. Commun.* **2019**, *10*, 4290.
- [289] Yang, J. R.; Li, W. H.; Tan, S. D.; Xu, K. N.; Wang, Y.; Wang, D. S.; Li, Y. D. The electronic metal-support interaction directing the design of single atomic site catalysts: Achieving high efficiency towards hydrogen evolution. *Angew. Chem., Int. Ed.* **2021**, *60*, 19085–19091.
- [290] Li, W. H.; Yang, J. R.; Jing, H. Y.; Zhang, J.; Wang, Y.; Li, J.; Zhao, J.; Wang, D. S.; Li, Y. D. Creating high regioselectivity by electronic metal-support interaction of a single-atomic-site catalyst. *J. Am. Chem. Soc.* **2021**, *143*, 15453–15461.
- [291] Wu, J. B.; Su, J. W.; Wu, T.; Huang, L.; Li, Q.; Luo, Y. X.; Jin, H. R.; Zhou, J.; Zhai, T. Y.; Wang, D. S. et al. Scalable synthesis of 2D Mo₂C and thickness-dependent hydrogen evolution on its basal plane and edges. *Adv. Mater.* **2023**, *35*, 2209954.
- [292] Li, Q.; Wu, J. B.; Wu, T.; Jin, H. R.; Zhang, N.; Li, J.; Liang, W. X.; Liu, M. L.; Huang, L.; Zhou, J. Phase engineering of atomically thin perovskite oxide for highly active oxygen evolution. *Adv.*

- Funct. Mater.* **2021**, *31*, 2102002.
- [293] Ye, C. L.; Peng, M.; Li, Y.; Wang, D. S.; Chen, C.; Li, Y. D. Atomically dispersed Pt in ordered PtSnZn intermetallic with Pt-Sn and Pt-Zn pairs for selective propane dehydrogenation. *Sci. China Mater.* **2023**, *66*, 1071–1078.
- [294] Yan, J. H.; Dong, K. Q.; Zhang, Y. Y.; Wang, X.; Aboalhassan, A. A.; Yu, J. Y.; Ding, B. Multifunctional flexible membranes from sponge-like porous carbon nanofibers with high conductivity. *Nat. Commun.* **2019**, *10*, 5584.
- [295] Zhuang, Z. C.; Li, Y.; Li, Y. H.; Huang, J. Z.; Wei, B.; Sun, R.; Ren, Y. J.; Ding, J.; Zhu, J. X.; Lang, Z. Q. et al. Atomically dispersed nonmagnetic electron traps improve oxygen reduction activity of perovskite oxides. *Energy Environ. Sci.* **2021**, *14*, 1016–1028.
- [296] Wang, Y.; Wang, D. S.; Li, Y. D. Rational design of single-atom site electrocatalysts: From theoretical understandings to practical applications. *Adv. Mater.* **2021**, *33*, 2008151.
- [297] Chen, Y. J.; Gao, R.; Ji, S. F.; Li, H. J.; Tang, K.; Jiang, P.; Hu, H. B.; Zhang, Z. D.; Hao, H. G.; Qu, Q. Y. et al. Atomic-level modulation of electronic density at cobalt single-atom sites derived from metal-organic frameworks: Enhanced oxygen reduction performance. *Angew. Chem., Int. Ed.* **2021**, *60*, 3212–3221.
- [298] Han, Y. H.; Dai, J.; Xu, R. R.; Ai, W. Y.; Zheng, L. R.; Wang, Y.; Yan, W. S.; Chen, W. X.; Luo, J.; Liu, Q. et al. Notched-polyoxometalate strategy to fabricate atomically dispersed Ru catalysts for biomass conversion. *ACS Catal.* **2021**, *11*, 2669–2675.
- [299] Jia, Y. L.; Xue, Z. Q.; Yang, J.; Liu, Q. L.; Xian, J. H.; Zhong, Y. C.; Sun, Y. M.; Zhang, X. X.; Liu, Q. H.; Yao, D. X. et al. Tailoring the electronic structure of an atomically dispersed zinc electrocatalyst: Coordination environment regulation for high selectivity oxygen reduction. *Angew. Chem., Int. Ed.* **2022**, *61*, e202110838.
- [300] Tian, S. B.; Wang, B. X.; Gong, W. B.; He, Z. Z.; Xu, Q.; Chen, W. X.; Zhang, Q. H.; Zhu, Y. Q.; Yang, J. R.; Fu, Q. et al. Dual-atom Pt heterogeneous catalyst with excellent catalytic performances for the selective hydrogenation and epoxidation. *Nat. Commun.* **2021**, *12*, 3181.
- [301] Segler, M. H. S.; Preuss, M.; Waller, M. P. Planning chemical syntheses with deep neural networks and symbolic AI. *Nature* **2018**, *555*, 604–610.
- [302] Collins, K. D.; Glorius, F. A robustness screen for the rapid assessment of chemical reactions. *Nat. Chem.* **2013**, *5*, 597–601.
- [303] Robinson, R. LXIII.-A synthesis of tropinone. *J. Chem. Soc. Trans.* **1917**, *111*, 762–768.
- [304] Chong, L. N.; Gao, G. P.; Wen, J. G.; Li, H. X.; Xu, H. P.; Green, Z.; Sugar, J. D.; Kropf, A. J.; Xu, W. Q.; Lin, X. M. et al. La-and Mn-doped cobalt spinel oxygen evolution catalyst for proton exchange membrane electrolysis. *Science* **2023**, *380*, 609–616.
- [305] Smith, R. D. L.; Prévot, M. S.; Fagan, R. D.; Zhang, Z. P.; Sedach, P. A.; Siu, M. K. J.; Trudel, S.; Berlinguette, C. P. Photochemical route for accessing amorphous metal oxide materials for water oxidation catalysis. *Science* **2013**, *340*, 60–63.
- [306] Huang, J. Z.; Sheng, H. Y.; Ross, R. D.; Han, J. C.; Wang, X. J.; Song, B.; Jin, S. Modifying redox properties and local bonding of Co_3O_4 by CeO_2 enhances oxygen evolution catalysis in acid. *Nat. Commun.* **2021**, *12*, 3036.
- [307] Jing, H. Y.; Zhu, P.; Zheng, X. B.; Zhang, Z. D.; Wang, D. S.; Li, Y. D. Theory-oriented screening and discovery of advanced energy transformation materials in electrocatalysis. *Adv. Powder Mater.* **2022**, *1*, 100013.
- [308] Wang, L. G.; Ma, N.; Wu, N.; Wang, X. G.; Xin, J. J.; Wang, D. S.; Lin, J. H.; Li, X. G.; Sun, J. L. Stable, efficient, copper coordination polymer-derived heterostructured catalyst for oxygen evolution under pH-universal conditions. *ACS Appl. Mater. Interfaces* **2021**, *13*, 25461–25471.
- [309] Liu, Z. H.; Du, Y.; Yu, R. H.; Zheng, M. B.; Hu, R.; Wu, J. S.; Xia, Y. Y.; Zhuang, Z. C.; Wang, D. S. Tuning mass transport in electrocatalysis down to sub-5 nm through nanoscale grade separation. *Angew. Chem., Int. Ed.* **2023**, *62*, e202212653.
- [310] Wang, L. G.; Su, H.; Tan, G. Y.; Xin, J. J.; Wang, X. G.; Zhang, Z.; Li, Y. P.; Qiu, Y.; Li, X. H.; Li, H. S. et al. Boosting efficient and sustainable alkaline water oxidation on W-CoOOH-TT Pair sites catalyst synthesized via topochemical transformation. *Adv. Mater.*, in press, DOI: 10.1002/adma.202302642.
- [311] Rong, C. L.; Shen, X. J.; Wang, Y.; Thomsen, L.; Zhao, T. W.; Li, Y. B.; Lu, X. Y.; Amal, R.; Zhao, C. Electronic structure engineering of single-atom Ru sites via Co-N₄ sites for bifunctional pH-universal water splitting. *Adv. Mater.* **2022**, *34*, 2110103.
- [312] Wan, L.; Xu, Z. A.; Xu, Q.; Wang, P. C.; Wang, B. G. Overall design of novel 3D-ordered MEA with drastically enhanced mass transport for alkaline electrolyzers. *Energy Environ. Sci.* **2022**, *15*, 1882–1892.
- [313] Browne, M. P.; Redondo, E.; Pumera, M. 3D printing for electrochemical energy applications. *Chem. Rev.* **2020**, *120*, 2783–2810.
- [314] Zheng, X. B.; Yang, J. R.; Xu, Z. F.; Wang, Q. S.; Wu, J. B.; Zhang, E. H.; Dou, S. X.; Sun, W. P.; Wang, D. S.; Li, Y. D. Ru-Co pair sites catalyst boosts the energetics for the oxygen evolution reaction. *Angew. Chem., Int. Ed.* **2022**, *61*, e202205946.
- [315] Lin, C.; Li, J. L.; Li, X. P.; Yang, S.; Luo, W.; Zhang, Y. J.; Kim, S. H.; Kim, D. H.; Shinde, S. S.; Li, Y. F. et al. *In-situ* reconstructed Ru atom array on $\alpha\text{-MnO}_2$ with enhanced performance for acidic water oxidation. *Nat. Catal.* **2021**, *4*, 1012–1023.
- [316] Hao, S. Y.; Sheng, H. Y.; Liu, M.; Huang, J. Z.; Zheng, G. K.; Zhang, F.; Liu, X. N.; Su, Z. W.; Hu, J. J.; Qian, Y. et al. Torsion strained iridium oxide for efficient acidic water oxidation in proton exchange membrane electrolyzers. *Nat. Nanotechnol.* **2021**, *16*, 1371–1377.
- [317] Wen, Y. Z.; Chen, P. N.; Wang, L.; Li, S. Y.; Wang, Z. Y.; Abed, J.; Mao, X. N.; Min, Y. M.; Dinh, C. T.; Luna, P. D. et al. Stabilizing highly active Ru sites by suppressing lattice oxygen participation in acidic water oxidation. *J. Am. Chem. Soc.* **2021**, *143*, 6482–6490.
- [318] Shi, Z. P.; Li, J.; Wang, Y. B.; Liu, S. W.; Zhu, J. B.; Yang, J. H.; Wang, X.; Ni, J.; Jiang, Z.; Zhang, L. J. et al. Customized reaction route for ruthenium oxide towards stabilized water oxidation in high-performance PEM electrolyzers. *Nat. Commun.* **2023**, *14*, 843.
- [319] Sun, K. A.; Wu, X. Y.; Zhuang, Z. W.; Liu, L. Y.; Fang, J. J.; Zeng, L. Y.; Ma, J. G.; Liu, S. J.; Li, J. Z.; Dai, R. Y. et al. Interfacial water engineering boosts neutral water reduction. *Nat. Commun.* **2022**, *13*, 6260.
- [320] Fu, X. B.; Zhang, J. H.; Zhan, S. Q.; Xia, F. J.; Wang, C. J.; Ma, D. S.; Yue, Q.; Wu, J. S.; Kang, Y. J. High-entropy alloy nanosheets for fine-tuning hydrogen evolution. *ACS Catal.* **2022**, *12*, 11955–11959.
- [321] Cipriano, L. A.; Di Liberto, G.; Pacchioni, G. Superoxide and peroxy complexes on single-atom catalysts: Impact on the oxygen evolution reaction. *ACS Catal.* **2022**, *12*, 11682–11691.
- [322] He, Q.; Zhou, Y. Z.; Shou, H. W.; Wang, X. Y.; Zhang, P. J.; Xu, W. J.; Qiao, S. C.; Wu, C. Q.; Liu, H. J.; Liu, D. B. et al. Synergic reaction kinetics over adjacent ruthenium sites for superb hydrogen generation in alkaline media. *Adv. Mater.* **2022**, *34*, 2110604.
- [323] Dinh, C. T.; Jain, A.; De Arquer, F. P. G.; De Luna, P.; Li, J.; Wang, N.; Zheng, X. L.; Cai, J.; Gregory, B. Z.; Voznyy, O. et al. Multi-site electrocatalysts for hydrogen evolution in neutral media by destabilization of water molecules. *Nat. Energy* **2019**, *4*, 107–114.
- [324] Chen, J. D.; Chen, C. H.; Qin, M. K.; Li, B.; Lin, B. B.; Mao, Q.; Yang, H. B.; Liu, B.; Wang, Y. Reversible hydrogen spillover in Ru-WO_{3-x} enhances hydrogen evolution activity in neutral pH water splitting. *Nat. Commun.* **2022**, *13*, 5382.
- [325] Yang, Q.; Liu, H. X.; Yuan, P.; Jia, Y.; Zhuang, L. Z.; Zhang, H. W.; Yan, X. C.; Liu, G. H.; Zhao, Y. F.; Liu, J. Z. et al. Single carbon vacancy traps atomic platinum for hydrogen evolution catalysis. *J. Am. Chem. Soc.* **2022**, *144*, 2171–2178.
- [326] Zheng, Y.; Jiao, Y.; Vasileff, A.; Qiao, S. Z. The hydrogen evolution reaction in alkaline solution: From theory, single crystal models, to practical electrocatalysts. *Angew. Chem., Int. Ed.* **2018**, *57*, 7568–7579.
- [327] Zhang, J. Y.; Zhang, H. C.; Cheng, M. J.; Lu, Q. Tailoring the electrochemical production of H_2O_2 : Strategies for the rational

- design of high-performance electrocatalysts. *Small* **2020**, *16*, 1902845.
- [328] Tian, Y. H.; Li, M.; Wu, Z. Z.; Sun, Q.; Yuan, D.; Johannessen, B.; Xu, L.; Wang, Y.; Dou, Y. H.; Zhao, H. J. et al. Edge-hosted atomic Co-N₄ sites on hierarchical porous carbon for highly selective two-electron oxygen reduction reaction. *Angew. Chem., Int. Ed.* **2022**, *61*, e202213296.
- [329] Mao, J. J.; He, C. T.; Pei, J. J.; Liu, Y.; Li, J.; Chen, W. X.; He, D. S.; Wang, D. S.; Li, Y. D. Isolated Ni atoms dispersed on Ru nanosheets: High-performance electrocatalysts toward hydrogen oxidation reaction. *Nano Lett.* **2020**, *20*, 3442–3448.
- [330] Han, A. L.; Wang, X. J.; Tang, K.; Zhang, Z. D.; Ye, C. L.; Kong, K. J.; Hu, H. B.; Zheng, L. R.; Jiang, P.; Zhao, C. X. et al. An adjacent atomic platinum site enables single-atom iron with high oxygen reduction reaction performance. *Angew. Chem., Int. Ed.* **2021**, *60*, 19262–19271.
- [331] Han, A.; Sun, W. M.; Wan, X.; Cai, D. D.; Wang, X. J.; Li, F.; Shui, J. L.; Wang, D. S. Construction of Co₄ atomic clusters to enable Fe-N₄ motifs with highly active and durable oxygen reduction performance. *Angew. Chem., Int. Ed.* **2023**, *62*, e202303185.
- [332] Wang, Y.; Wu, J.; Tang, S. H.; Yang, J. R.; Ye, C. L.; Chen, J.; Lei, Y. P.; Wang, D. S. Synergistic Fe-Se atom Pairs as bifunctional oxygen electrocatalysts boost low-temperature rechargeable Zn-Air battery. *Angew. Chem., Int. Ed.* **2023**, *62*, e202219191.
- [333] Kim, H. W.; Bukas, V. J.; Park, H.; Park, S.; Diederichsen, K. M.; Lim, J.; Cho, Y. H.; Kim, J.; Kim, W.; Han, T. H. et al. Mechanisms of two-electron and four-electron electrochemical oxygen reduction reactions at nitrogen-doped reduced graphene oxide. *ACS Catal.* **2020**, *10*, 852–863.
- [334] Deng, Y. J.; Luo, J. M.; Chi, B.; Tang, H. B.; Li, J.; Qiao, X. C.; Shen, Y. J.; Yang, Y. J.; Jia, C. M.; Rao, P. et al. Advanced atomically dispersed metal-nitrogen-carbon catalysts toward cathodic oxygen reduction in PEM fuel cells. *Adv. Energy Mater.* **2021**, *11*, 210122.
- [335] Zhuang, Z. C.; Xia, L. X.; Huang, J. Z.; Zhu, P.; Li, Y.; Ye, C. L.; Xia, M. G.; Yu, R. H.; Lang, Z. Q.; Zhu, J. X. et al. Continuous modulation of electrocatalytic oxygen reduction activities of single-atom catalysts through p-n junction rectification. *Angew. Chem., Int. Ed.* **2023**, *62*, e202212335.
- [336] Cui, T. T.; Wang, Y. P.; Ye, T.; Wu, J.; Chen, Z. Q.; Li, J.; Lei, Y. P.; Wang, D. S.; Li, Y. D. Engineering dual single-atom sites on 2D ultrathin N-doped carbon nanosheets attaining ultra-low-temperature zinc-air battery. *Angew. Chem., Int. Ed.* **2022**, *61*, e202115219.
- [337] Kim, S.; Lee, Y. M. Two-dimensional nanosheets and membranes for their emerging technologies. *Curr. Opin. Chem. Eng.* **2023**, *39*, 100893.
- [338] Hu, C.; Xu, J. J.; Tan, Y. Z.; Huang, X. Q. Recent advances of ruthenium-based electrocatalysts for hydrogen energy. *Trends Chem.* **2023**, *5*, 225–239.
- [339] Liu, S. S.; Wang, M. F.; Qian, T.; Ji, H. Q.; Liu, J.; Yan, C. L. Facilitating nitrogen accessibility to boron-rich covalent organic frameworks via electrochemical excitation for efficient nitrogen fixation. *Nat. Commun.* **2019**, *10*, 3898.
- [340] Sim, H. Y. F.; Chen, J. R. T.; Koh, C. S. L.; Lee, H. K.; Han, X. M.; Phan-Quang, G. C.; Pang, J. Y.; Lay, C. L.; Pedireddy, S.; Phang, I. Y. et al. ZIF-induced d-band modification in a bimetallic nanocatalyst: Achieving over 44% efficiency in the ambient nitrogen reduction reaction. *Angew. Chem., Int. Ed.* **2020**, *59*, 16997–17003.
- [341] Sahoo, S.; Dekel, D. R.; Maric, R.; Alpay, S. P. Atomistic insights into the hydrogen oxidation reaction of palladium-ceria bifunctional catalysts for anion-exchange membrane fuel cells. *ACS Catal.* **2021**, *11*, 2561–2571.
- [342] Gruber, N.; Galloway, J. N. An earth-system perspective of the global nitrogen cycle. *Nature* **2008**, *451*, 293–296.
- [343] Chen, G. F.; Cao, X. R.; Wu, S. Q.; Zeng, X. Y.; Ding, L. X.; Zhu, M.; Wang, H. H. Ammonia electrosynthesis with high selectivity under ambient conditions via a Li⁺ incorporation strategy. *J. Am. Chem. Soc.* **2017**, *139*, 9771–9774.
- [344] Guo, C. X.; Ran, J. R.; Vasileff, A.; Qiao, S. Z. Rational design of electrocatalysts and photo(electro)catalysts for nitrogen reduction to ammonia (NH₃) under ambient conditions. *Energy Environ. Sci.* **2018**, *11*, 45–56.
- [345] Van Der Ham, C. J. M.; Koper, M. T. M.; Hetterscheid, D. G. H. Challenges in reduction of dinitrogen by proton and electron transfer. *Chem. Soc. Rev.* **2014**, *43*, 5183–5191.
- [346] Li, S. J.; Bao, D.; Shi, M. M.; Wulan, B. R.; Yan, J. M.; Jiang, Q. Amorphizing of Au nanoparticles by CeO_x-RGO hybrid support towards highly efficient electrocatalyst for N₂ reduction under ambient conditions. *Adv. Mater.* **2017**, *29*, 1700001.
- [347] Wang, J.; Yu, L.; Hu, L.; Chen, G.; Xin, H. L.; Feng, X. F. Ambient ammonia synthesis via palladium-catalyzed electrohydrogenation of dinitrogen at low overpotential. *Nat. Commun.* **2018**, *9*, 1795.
- [348] Wang, M. F.; Liu, S. S.; Qian, T.; Liu, J.; Zhou, J. Q.; Ji, H. Q.; Xiong, J.; Zhong, J.; Yan, C. L. Over 56.55% faradaic efficiency of ambient ammonia synthesis enabled by positively shifting the reaction potential. *Nat. Commun.* **2019**, *10*, 341.
- [349] Fu, X. B.; Pedersen, J. B.; Zhou, Y. Y.; Saccoccio, M.; Li, S. F.; Sažinas, R.; Li, K.; Andersen, S. Z.; Xu, A. N.; Deissler, N. H. et al. Continuous-flow electrosynthesis of ammonia by nitrogen reduction and hydrogen oxidation. *Science* **2023**, *379*, 707–712.
- [350] Shen, H. D.; Choi, C.; Masa, J.; Li, X.; Qiu, J. S.; Jung, Y.; Sun, Z. Y. Electrochemical ammonia synthesis: Mechanistic understanding and catalyst design. *Chem* **2021**, *7*, 1708–1754.
- [351] Yu, X. M.; Han, P.; Wei, Z. X.; Huang, L. S.; Gu, Z. X.; Peng, S. J.; Ma, J. M.; Zheng, G. F. Boron-doped graphene for electrocatalytic N₂ reduction. *Joule* **2018**, *2*, 1610–1622.
- [352] Chen, S. H.; Wang, B. Q.; Zhu, J. X.; Wang, L. Q.; Ou, H. H.; Zhang, Z. D.; Liang, X.; Zheng, L. R.; Zhou, L.; Su, Y. Q. et al. Lewis acid site-promoted single-atomic Cu catalyzes electrochemical CO₂ methanation. *Nano Lett.* **2021**, *21*, 7325–7331.
- [353] Zhu, J. B.; Xiao, M. L.; Ren, D. Z.; Gao, R.; Liu, X. Z.; Zhang, Z.; Luo, D.; Xing, W.; Su, D.; Yu, A. P. et al. Quasi-covalently coupled Ni-Cu atomic pair for synergistic electroreduction of CO₂. *J. Am. Chem. Soc.* **2022**, *144*, 9661–9671.
- [354] Qian, Y.; Liu, Y.; Zhao, Y.; Zhang, X.; Yu, G. Single vs double atom catalyst for N₂ activation in nitrogen reduction reaction: A DFT perspective. *EcoMat* **2020**, *2*, e12014.
- [355] Nitopi, S.; Bertheussen, E.; Scott, S. B.; Liu, X. Y.; Engstfeld, A. K.; Horch, S.; Seger, B.; Stephens, I. E. L.; Chan, K.; Hahn, C. et al. Progress and perspectives of electrochemical CO₂ reduction on copper in aqueous electrolyte. *Chem. Rev.* **2019**, *119*, 7610–7672.
- [356] De Luna, P.; Hahn, C.; Higgins, D.; Jaffer, S. A.; Jaramillo, T. F.; Sargent, E. H. What would it take for renewably powered electrosynthesis to displace petrochemical processes. *Science* **2019**, *364*, eaav3506.
- [357] Gu, J.; Hsu, C. S.; Bai, L. C.; Chen, H. M.; Hu, X. L. Atomically dispersed Fe³⁺ sites catalyze efficient CO₂ electroreduction to CO. *Science* **2019**, *364*, 1091–1094.
- [358] Wang, X. L.; De Araújo, J. F.; Ju, W.; Bagger, A.; Schmies, H.; Kühl, S.; Rossmeisl, J.; Strasser, P. Mechanistic reaction pathways of enhanced ethylene yields during electroreduction of CO₂-CO co-feeds on Cu and Cu-tandem electrocatalysts. *Nat. Nanotechnol.* **2019**, *14*, 1063–1070.
- [359] Birdja, Y. Y.; Pérez-Gallent, E.; Figueiredo, M. C.; Göttle, A. J.; Calle-Vallejo, F.; Koper, M. T. M. Advances and challenges in understanding the electrocatalytic conversion of carbon dioxide to fuels. *Nat. Energy* **2019**, *4*, 732–745.
- [360] Zhang, Z. D.; Zhu, J. X.; Chen, S. H.; Sun, W. M.; Wang, D. S. Liquid fluxional Ga single atom catalysts for efficient electrochemical CO₂ reduction. *Angew. Chem., Int. Ed.* **2023**, *62*, e202215136.
- [361] Shen, Y.; Ren, C. J.; Zheng, L. R.; Xu, X. Y.; Long, R.; Zhang, W. Q.; Yang, Y.; Zhang, Y. C.; Yao, Y. F.; Chi, H. Q. et al. Room-temperature photosynthesis of propane from CO₂ with Cu single atoms on vacancy-rich TiO₂. *Nat. Commun.* **2023**, *14*, 1117.
- [362] Huang, J. E.; Li, F. W.; Ozden, A.; Rasouli, A. S.; De Arquer, F. P. G.; Liu, S. J.; Zhang, S. Z.; Luo, M. C.; Wang, X.; Lum, Y. et al. CO₂ electrolysis to multicarbon products in strong acid. *Science* **2021**, *372*, 1074–1078.



- [363] Gao, Y.; Liu, B. Z.; Wang, D. S. Microenvironment engineering of single/dual-atom catalysts for electrocatalytic application. *Adv. Mater.*, in press, DOI: 10.1002/adma.202209654.
- [364] Jiao, L.; Yang, W. J.; Wan, G.; Zhang, R.; Zheng, X. S.; Zhou, H.; Yu, S. H.; Jiang, H. L. Single-atom electrocatalysts from multivariate metal-organic frameworks for highly selective reduction of CO₂ at low pressures. *Angew. Chem., Int. Ed.* **2020**, *59*, 20589–20595.
- [365] Bao, H. H.; Qiu, Y.; Peng, X. Y.; Wang, J. A.; Mi, Y. Y.; Zhao, S. Z.; Liu, X. J.; Liu, Y. F.; Cao, R.; Zhuo, L. C. et al. Isolated copper single sites for high-performance electroreduction of carbon monoxide to multicarbon products. *Nat. Commun.* **2021**, *12*, 238.
- [366] Shang, H. S.; Wang, T.; Pei, J. J.; Jiang, Z. L.; Zhou, D. N.; Wang, Y.; Li, H. J.; Dong, J. C.; Zhuang, Z. B.; Chen, W. X. et al. Design of a single-atom indium³⁺-N₄ interface for efficient electroreduction of CO₂ to formate. *Angew. Chem., Int. Ed.* **2020**, *59*, 22465–22469.
- [367] Yang, J. R.; Li, W. H.; Wang, D. S.; Li, Y. D. Single-atom materials: Small structures determine macroproperties. *Small Struct.* **2021**, *2*, 2000051.
- [368] Cai, Y. M.; Fu, J. J.; Zhou, Y.; Chang, Y. C.; Min, Q. H.; Zhu, J. J.; Lin, Y. H.; Zhu, W. L. Insights on forming N, O-coordinated Cu single-atom catalysts for electrochemical reduction CO₂ to methane. *Nat. Commun.* **2021**, *12*, 586.
- [369] Das, S.; Pérez-Ramírez, J.; Gong, J. L.; Dewangan, N.; Hidajat, K.; Gates, B. C.; Kawi, S. Core-shell structured catalysts for thermocatalytic, photocatalytic, and electrocatalytic conversion of CO₂. *Chem. Soc. Rev.* **2020**, *49*, 2937–3004.
- [370] Yang, Y.; Li, Y. K.; Zhao, Y. X.; Wei, G. P.; Ren, Y.; Asmis, K. R.; He, S. G. Catalytic Co-conversion of CH₄ and CO₂ mediated by rhodium-titanium oxide anions RhTiO₂⁻. *Angew. Chem., Int. Ed.* **2021**, *60*, 13788–13792.
- [371] Shi, L.; Yang, G. H.; Tao, K.; Yoneyama, Y.; Tan, Y. S.; Tsubaki, N. An introduction of CO₂ conversion by dry reforming with methane and new route of low-temperature methanol synthesis. *Acc. Chem. Res.* **2013**, *46*, 1838–1847.
- [372] Galvis, H. M. T.; De Jong, K. P. Catalysts for production of lower olefins from synthesis gas: A review. *ACS Catal.* **2013**, *3*, 2130–2149.
- [373] Pakhare, D.; Spivey, J. A review of dry (CO₂) reforming of methane over noble metal catalysts. *Chem. Soc. Rev.* **2014**, *43*, 7813–7837.
- [374] Posada-Borbón, A.; Grönbeck, H. A first-principles-based microkinetic study of CO₂ reduction to CH₃OH over In₂O₃(110). *ACS Catal.* **2021**, *11*, 9996–10006.
- [375] Liu, B.; Liu, J.; Xin, L.; Zhang, T.; Xu, Y. B.; Jiang, F.; Liu, X. H. Unraveling reactivity descriptors and structure sensitivity in low-temperature NH₃-SCR reaction over CeTiO_x catalysts: A combined computational and experimental study. *ACS Catal.* **2021**, *11*, 7613–7636.
- [376] Luo, Z. X.; Castleman, A. W. Jr; Khanna, S. N. Reactivity of metal clusters. *Chem. Rev.* **2016**, *116*, 14456–14492.
- [377] Zhao, Y. X.; Li, Z. Y.; Yang, Y.; He, S. G. Methane activation by gas phase atomic clusters. *Acc. Chem. Res.* **2018**, *51*, 2603–2610.
- [378] Geng, C. Y.; Weiske, T.; Li, J. L.; Shaik, S.; Schwarz, H. Intrinsic reactivity of diatomic 3d transition-metal carbides in the thermal activation of methane: Striking electronic structure effects. *J. Am. Chem. Soc.* **2019**, *141*, 599–610.
- [379] Miller, G. B. S.; Esser, T. K.; Knorke, H.; Gewinner, S.; Schöllkopf, W.; Heine, N.; Asmis, K. R.; Uggerud, E. Spectroscopic identification of a bidentate binding motif in the anionic magnesium-CO₂ complex ([ClMgCO₂]⁻). *Angew. Chem., Int. Ed.* **2014**, *53*, 14407–14410.
- [380] Zhao, D.; Tian, X. X.; Doronkin, D. E.; Han, S. L.; Kondratenko, V. A.; Grunwaldt, J. D.; Perechodnik, A.; Vuong, T. H.; Rabeah, J.; Eckelt, R. et al. *In situ* formation of ZnO_x species for efficient propane dehydrogenation. *Nature* **2021**, *599*, 234–238.
- [381] Motagamwala, A. H.; Almallahi, R.; Wortman, J.; Igenegbhai, V. O.; Linic, S. Stable and selective catalysts for propane dehydrogenation operating at thermodynamic limit. *Science* **2021**, *373*, 217–222.
- [382] Hannagan, R. T.; Giannakakis, G.; Réocreux, R.; Schumann, J.; Finzel, J.; Wang, Y. C.; Michaelides, A.; Deshlahra, P.; Christopher, P.; Flytzani-Stephanopoulos, M. et al. First-principles design of a single-atom-alloy propane dehydrogenation catalyst. *Science* **2021**, *372*, 1444–1447.
- [383] Chang, X.; Zhao, Z. J.; Lu, Z. P.; Chen, S.; Luo, R.; Zha, S.; Li, L. L.; Sun, G. D.; Pei, C. L.; Gong, J. L. Designing single-site alloy catalysts using a degree-of-isolation descriptor. *Nat. Nanotechnol.* **2023**, *18*, 611–616.
- [384] Correa-Baena, J. P.; Hippalgaonkar, K.; Van Duren, J.; Jaffer, S.; Chandrasekhar, V. R.; Stevanovic, V.; Wadia, C.; Guha, S.; Buonassisi, T. Accelerating materials development via automation, machine learning, and high-performance computing. *Joule* **2018**, *2*, 1410–1420.
- [385] Krivanek, O. L.; Chisholm, M. F.; Nicolosi, V.; Pennycook, T. J.; Corbin, G. J.; Dellby, N.; Murfitt, M. F.; Own, C. S.; Szilagyi, Z. S.; Oxley, M. P. et al. Atom-by-atom structural and chemical analysis by annular dark-field electron microscopy. *Nature* **2010**, *464*, 571–574.
- [386] Sun, Z. H.; Liu, Q. H.; Yao, T.; Yan, W. S.; Wei, S. Q. X-ray absorption fine structure spectroscopy in nanomaterials. *Sci. China Mater.* **2015**, *58*, 313–341.
- [387] Funke, H.; Scheinost, A. C.; Chukalina, M. Wavelet analysis of extended X-ray absorption fine structure data. *Phys. Rev. B* **2005**, *71*, 094110.
- [388] Liu, J. C.; Wang, Y. G.; Li, J. Toward rational design of oxide-supported single-atom catalysts: Atomic dispersion of gold on ceria. *J. Am. Chem. Soc.* **2017**, *139*, 6190–6199.
- [389] Xie, Y. C.; Zhang, C.; Hu, X. Q.; Zhang, C.; Kelley, S. P.; Atwood, J. L.; Lin, J. Machine learning assisted synthesis of metal-organic nanocapsules. *J. Am. Chem. Soc.* **2020**, *142*, 1475–1481.